JUSTUS-LIEBIG-
UNIVERSITÄT
GIESSEN

Mass Measurements of ^{238}U-Projectile Fragments for the First Time with a Multiple-Reflection Time-Of-Flight Mass Spectrometer

Inauguraldissertation zur Erlangung des Doktorgrades der
Naturwissenschaftlichen Fakultät der Justus-Liebig-Universität Gießen

vorgelegt von

Jens Ebert
geboren in Gießen

Fachbereich 07 - Mathematik und Informatik, Physik, Geographie

II. Physikalisches Institut Justus-Liebig-Universität Gießen

Gießen 2016

Zusammenfassung

Im Rahmen dieser Arbeit wurden erstmal mit einem Multireflexions Flugzeit-Massenspektrometer (MR-TOF-MS) Massenmessungen an kurzlebigen Uran-Projektilfragmente durchgeführt. Ein Hauptteil dieser Arbeit war die Entwicklung einer Datenauswertemethode für die MR-TOF-MS Massenmessungen exotischer Kerne am Fragmentseparator FRS der GSI. Das entwickelte Verfahren wurde erfolgreich auf die Daten zweier Pilotexperimente des MR-TOF-MS am FRS 2012 und 2014 angewandt, in denen die Massen der Isotope ^{211}Rn, ^{211}Po und ^{220}Po erstmalig direkt gemessen wurden. Ebenfalls wurden umfangreiche Verbesserungen am MR-TOF-MS nach dem ersten Experiment im Rahmen dieser Arbeit durchgeführt.

In den Experimenten wurden Projektilfragmente mit 1000 MeV/u ^{238}U Ionen in einem Be/Nb Target am Eingang des im-Flug Separators FRS erzeugt. Die exotischen Kerne wurden räumlich separiert, in der Energie komprimiert und abgebremst mit dem Ionenoptischen System des FRS in Verbindung mit monoenergetischen und homogenen Degradern. Die Fragmente wurden am finalen Fokus des FRS mittels einer kryogenen Stoppzelle (CSC) vollständig abgebremst und thermalisiert. Die CSC war dabei mit 3-5 mg/cm^2 reinem Heliumgas gefüllt. Die exotischen Kerne wurden schnell aus der CSC extrahiert, um Massenmessungen sehr kurzlebiger Fragmente mit dem MR-TOF-MS zu ermöglichen. Das Erlangen dieses Ziels wurde erfolgreich durch die Massenmessung von ^{220}Ra Ionen mit einer Lebensdauer von 17,9 ms und 11 detektierten Ereignissen demonstriert. Die Massenmessungen der Isobare ^{211}Fr, ^{211}Po und ^{211}Rn haben klar das wissenschaftliche Potential des MR-TOF-MS für die Untersuchung exotischer Kerne und die Fähigkeiten des Datenauswerteprogramms aufgezeigt. Die Herausforderung des neuen Datenauswerteverfahrens, das auf der Maximum Likelihood Methode beruht, bestand in den Messungen mit überlappenden Verteilungen und nur wenigen Ereignissen in den Spektren. Die Drifts während der Messungen wurden mit der neu entwickelten Zeit-aufgelösten Kalibration korrigiert. Nach den Verbesserungen des Aufbaus als Konsequenz des ersten Experiments 2012 und der Anwendung der Zeit-aufgelösten Kalibration wurde im zweiten Experiment 2014 ein Massenauflösungsvermögen von 400.000 erreicht. Zusätzlich wurde eine Elektronenstoßquelle installiert, um Kalibranten aus Gasen wie Xe und SF_6 erzeugen zu können. Die Verfügbarkeit zahlreicher Kalibranten ist eine Voraussetzung für Messungen über große Massenbereiche.

Die erreichten Massengenauigkeiten dieser Pilotexperimente betrugen ungefähr $1{\cdot}10^{-6}$. Der Beitrag des Datenauswerteverfahrens und der resultierende systematische Fehler

befanden sich im Bereich von 10^{-8}. Die Zuverlässigkeit der gegenwärtigen Auswertemethode wurde reiflich in detaillierten Simulationen untersucht. Die gemessene Verteilungsfunktion wurde durch die exponentiell modifizierte Gauß-Funktion angenähert. Mittels stark überlappender Massenverteilungen, niedrigen Zählraten und variablen Mengen an Untergrund wurde die Auswertemethode getestet.

Zusammengefasst haben der experimentelle Aufbau für Massenmessungen sehr seltener und kurzlebiger Kerne und die zugehörige Datenauswertemethode im Rahmen dieser Dissertation ein großes Potential für hoch-aufgelöste Messungen in zukünftigen Experimenten erreicht.

Contents

1. Introduction **7**

2. Basics of Mass Measurements of Exotic Nuclei **9**
2.1. Motivation . . . 9
2.2. Production . . . 10
2.3. Separation . . . 11
2.4. Methods of Mass Measurements . . . 12
2.4.1. Penning Traps . . . 12
2.4.2. Storage Rings . . . 14
2.4.3. Time-of-Flight Mass Spectrometer . . . 15
2.5. Analysis and Mass Calibration of the Multiple-Reflection Time-of-Flight Mass Spectrometer . . . 19
2.5.1. Relativistic Mass Calibration . . . 19
2.5.2. Mass Calibration with Different Turn Numbers . . . 21
2.5.3. Drift Correction . . . 22

3. Experimental Setup **25**
3.1. Fragment Separator . . . 25
3.2. Cryogenic Stopping Cell . . . 26
3.3. RFQ Beamline and Diagnostics Unit . . . 29
3.4. Multiple-Reflection Time-of-Flight Mass Spectrometer . . . 29
3.4.1. Data Acquisition . . . 33
3.4.2. Improvements of the MR-TOF-MS . . . 35

4. Development of the MR-TOF-MS Mass Analysis **41**
4.1. Development of the Fit Algorithm . . . 44
4.1.1. Test Procedure . . . 44
4.1.2. Generation of Random Numbers . . . 46
4.1.3. Fit Process . . . 46
4.1.4. Weighted Fits . . . 47
4.1.5. Iterative Fitting . . . 50
4.1.6. Influence of the Peak Width . . . 52
4.1.7. Bias Correction for Overlapping Peaks . . . 55
4.1.8. Comparison with Bootstrapping . . . 57
4.1.9. Calculation of Fit Errors . . . 59
4.2. Statistical Significance . . . 60
4.3. Summary . . . 61

5. Mass Measurements, Analysis and Results of ^{238}U-Projectile Fragments **65**
5.1. Experiment in 2012 . . . 66
5.1.1. Calibration and Fitting . . . 66
5.1.2. Error of the Mass Determination . . . 73
5.1.3. Results . . . 76
5.2. Experiment in 2014 . . . 77
5.2.1. Calibration And Fitting . . . 80
5.2.2. Error of the Mass Determination . . . 83
5.2.3. Results . . . 87
5.3. Comparison of the Experimental Results with Theoretical Predictions 88
5.4. Outlook on Future Error Contributions . . . 90

6. Summary and Conclusions **93**

A. Appendix **95**
A.1. Definitions . . . 95
A.2. Numerical Methods for Mass Determination . . . 95
A.3. Maximum Likelihood Estimation . . . 97
A.4. R Programming Language and Test Environment . . . 98
A.5. Exponentially Modified Gaussian . . . 99

Bibliography **101**

Acknowledgments **113**

1. Introduction

Accurate experimental mass values, separation energies and lifetimes are important for nuclear structure and astrophysics [Thielemann et al., 2001]. The experimental data contribute to the understanding of the stability of matter and the origin of the elements in the universe.
The nuclear models are based on accurately measured masses of nuclides close to the valley of stability. Therefore, new mass values of exotic nuclei represent a crucial test for the predictive power of the theoretical descriptions. The challenges of experiments with exotic nuclei are their short half-lives and the low production rates. More than 280 new exotic nuclei have been recently discovered with the in-flight fragment separator (FRS) [Geissel et al., 1992] at GSI [Geissel et al., 2016]. Most of the new nuclides are neutron rich and close to the expected astrophysical r-process path.
In the framework of this thesis a new device for accurate mass measurements and decay studies of exotic nuclei has been commissioned at the final focus of the FRS. The short-lived nuclei are produced via projectile fragmentation of ^{238}U ions at 1000 MeV / u in the target at the entrance of the FRS. The fragments of interest are spatially separated in-flight, slowed down and thermalized in a cryogenic stopping cell (CSC) [Purushothaman et al., 2013, Reiter, 2015]. The exotic nuclei are extracted from the CSC in about 20 ms and transported to a Multiple-Reflection Time-Of-Flight Mass Spectrometer (MR-TOF-MS) [Plaß et al., 2008, Dickel et al., 2015a, Dickel et al., 2015b]. The low-energy setup of the experiment, the FRS Ion Catcher, is a central part of the present work. For the first time masses of short-lived projectile fragments were measured in such an MR-TOF-MS. The main part of this thesis is the development and application of new analysis software tailored to the properties of exotic nuclei and few counts in the spectra. It is inevitable in the mass analysis to treat overlapping mass distributions caused either by different nuclides, or molecules, or by excited states of nuclei.

2. Basics of Mass Measurements of Exotic Nuclei

2.1. Motivation

The first systematic measurements of atomic masses performed by Aston [Aston, 1927] led to the nuclear liquid drop model and the mass formula of Weizsäcker [Weizsäcker, 1935]. Further measurements of stable and long-lived isotopes showed a structured deviation of the experimental data from the liquid drop model, as depicted in figure 2.1. This structure is caused by the evolution of neutron and proton shells in the nuclei.

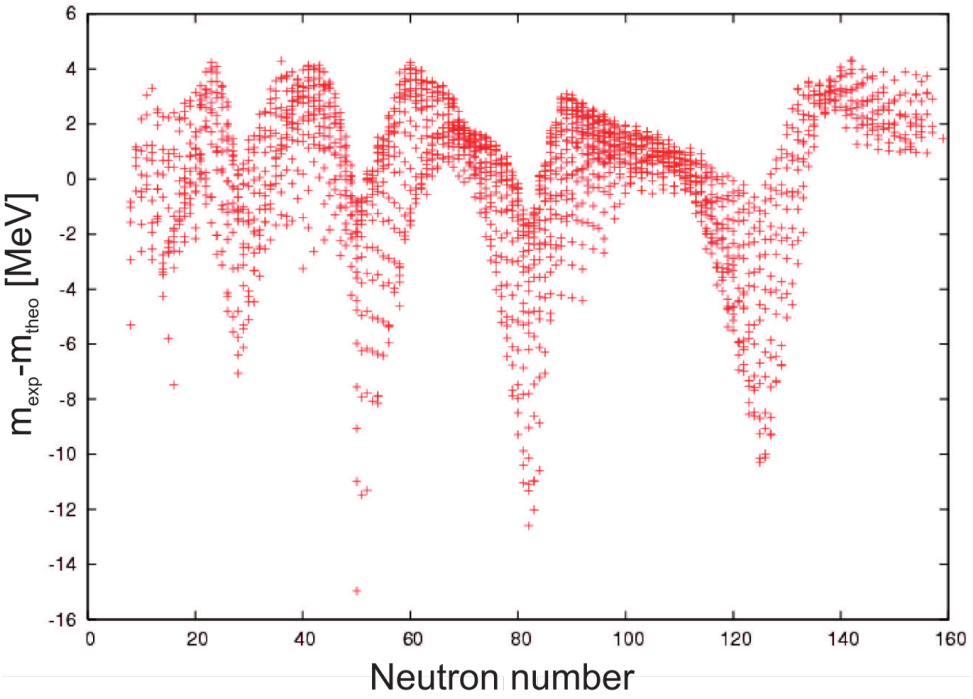

Figure 2.1.: Deviation between experimental data reported in reference [Audi et al., 2012] and the Weizsäcker mass formula [Diwisch, 2015].

Nowadays, the experimental data of isotopes close to the valley of β-stability are well described by different theories, but they strongly deviate for exotic nuclei, as shown in figure 2.2. The lack of accurate nuclear mass values limits the reliability of theoretical descriptions [Chomaz, 2003]. Even for the doubly magic nucleus ^{208}Pb

the theoretical descriptions differ and do not agree with experimental data, see insert of figure 2.2 [Bender et al., 2002].

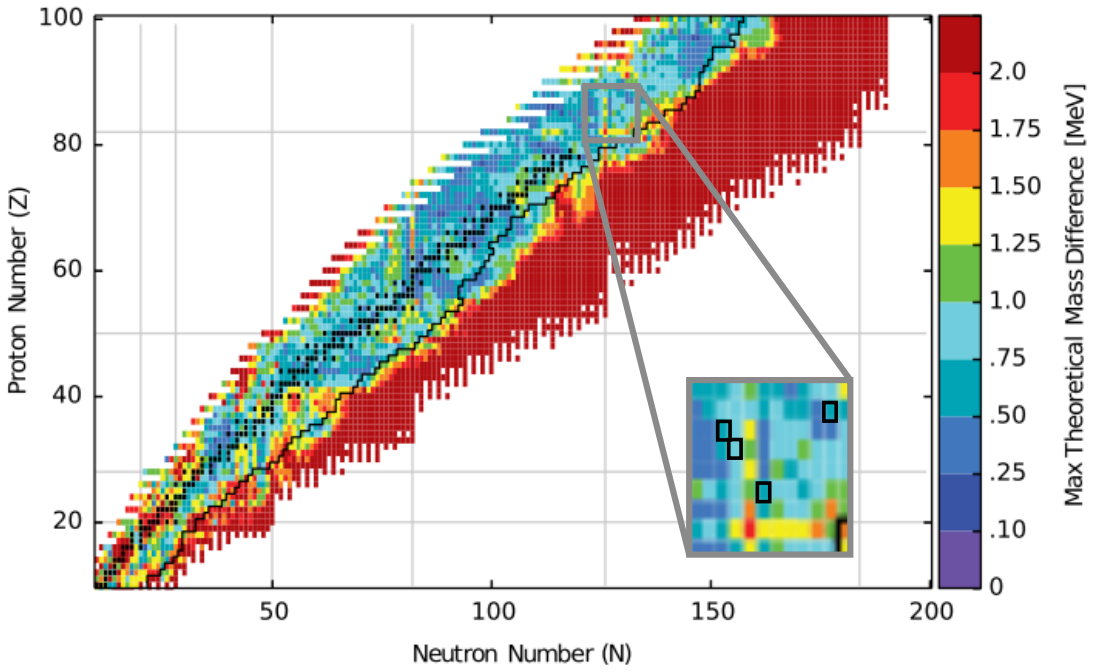

Figure 2.2.: Maximum deviations of predicted mass values of different models for all nuclei enclosed by the drip lines [Mumpower et al., 2015]. The black line indicates the experimentally known masses of the most neutron-rich isotopes [Wang et al., 2012]. The zoom includes the nuclei covered in the present experiment (black rectangles).

2.2. Production

Exotic nuclei can be produced via several nuclear reactions over a wide range of energies [Geissel et al., 1995, Mittig et al., 1997]. At energies close to the Coulomb barrier, fusion and transfer reactions are applied and at higher energies, above the Fermi velocity, fragmentation and abrasion fission are rich sources for exotic nuclei.

Fusion-Evaporation Fusion occurs in central collisions of projectile and target nuclei, whereby a compound nucleus is formed in the first stage. The compound nucleus dissipates its excitation energy by the emission of neutrons, protons, α-particles, γ-rays and fission in the case of heavy reaction products. The final product is called evaporation residue. The mean velocity of the fusion products is much lower than the incident projectile, due to the momentum conservation of the inelastic collisions. This method is well suited to produce neutron-deficient nuclei and heavy elements above Fermium [Münzenberg, 1998].

Projectile and Target Fragmentation Exotic nuclei are created by fragmentation above the Fermi energy. Fragmentation is a characterized by peripheral collisions. It can be described by the two-stage process of abrasion-ablation [Hüfner et al., 1975]. Depending on the projectile-target reference frame, one distinguishes projectile and target fragmentation. The mean velocity of the projectile fragments is close to the one of the projectiles. The fragments are kinematically focused in forward direction with a small energy and angular distribution [Morrissey, 1989]. The produced fragments cover the full range of elements below the heavier collision partner [Gaimard and Schmidt, 1991]. Projectile fragmentation is used at in-flight separators, whereas target fragmentation is applied at ISOL facilities.

Fission of Heavy Ions Fission of heavy nuclei produces neutron-rich medium mass isotopes. The element distribution of the fission products depends on the mass and excitation of the fissile nuclei. The fission reaction can be generated with low and high energy beams. For secondary beam experiments with fission fragments abrasion fission at relativistic energies represents a rich source of exotic nuclei. In general, the phase space of fission products is much larger than for projectile fragments.

2.3. Separation

The investigation and application of exotic nuclei requires an efficient separation from non-reacted projectiles and abundant background. Therefore, several sophisticated separation methods have been developed in nuclear structure and reaction laboratories. The two most common separation schemes are the Isotope Separation On-Line (ISOL) method and the in-flight separation. A combination of both methods is an in-flight separator coupled with a gas-filled stopping cell. The latter hybrid device is a central part of the present work.

Isotope Separation On-Line (ISOL) Method The ISOL method is mainly used in combination with target fragmentation and fission, deep-inelastic, transfer and fusion-evaporation reactions. The primary beam is thereby stopped in a target together with the produced nuclei. These nuclei diffuse out of the high temperature target. They are ionized, subsequently accelerated up to 60 keV and electromagnetically separated. For some elements selective laser ionization has been employed [Jokinen et al., 1997]. The time between production and separation mainly given by the needed time for the nuclei to diffuse out of the target ($\geq$ ms) is one disadvantage of this method besides the issue that not all elements can diffuse out of the target for chemical reasons. Their advantage is that ISOL beams have a small phase space and high intensities for some elements.

In-Flight Separation In-flight separation is used for high-energy production methods, such as projectile fragmentation and abrasion fission, characterized by a strong forward focusing of the fragments. Therefore, they have a relatively small energy and angular distribution. Furthermore, they exceed by far the energy of the Coulomb barrier. The fragments are separated by a combination of electromagnetic fields and energy loss in matter. The time-of-flight of the fragments through the separator takes less than 1 μs. In addition, in-flight separation is universally applicable for all elements and thus ideal for measurements of very short-lived nuclei. Fusion evaporation reactions in thin targets are also suitable for in-flight separation, but the evaporation residues have kinetic energies well below the Coulomb barrier and therefore, they can not be studied via secondary nuclear reactions.

2.4. Methods of Mass Measurements

Different techniques in nuclear physics are applied for accurate and high-resolving mass measurements of short-lived nuclei [Mittig et al., 1997, Lunney et al., 2003]. In general, the methods are based on frequency, time-of-flight and nuclear reaction measurements.
Established modern methods with mass resolving powers of 10^6 and accuracies of 10^{-7} and better are the measurement of cyclotron frequencies in Penning traps [Blaum, 2006] and the measurement of revolution times in heavy ion cooler-storage rings [Franzke et al., 2008]. The central part of this work is a novel time-of-flight mass spectrometer with an enlarged flight path realized by multiple reflections between electrostatic mirrors [Wollnik and Casares, 2003]. Therefore, the system is called Multiple-Reflection Time-of-Flight Mass Spectrometer (MR-TOF-MS). The comparison with Penning traps and cooler-storage rings shows that the MR-TOF-MS has many advantages and is competitive for mass measurements of exotic nuclei.
Presently three MR-TOF-MS are in use at different exotic nuclear beam facilities: at the BigRIPS at RIKEN / Japan [Schury et al., 2014], at ISOLDE at CERN / Switzerland [Wolf et al., 2013] and at the FRS at GSI / Germany [Dickel et al., 2015a].

2.4.1. Penning Traps

Ions are stored in Penning traps by means of a combination of a strong homogeneous magnetic dipole field B and a weak electrostatic potential [Blaum, 2006]. The ions with mass m and charge q move in a superposition of three independent motions in the electromagnetic fields: The axial motion with frequency ω_z, the cyclotron motion with reduced cyclotron frequency ω_+ and a drift motion with magnetron frequency ω_-. By measuring ω_+ and ω_- the cyclotron frequency ω_c and thus the mass-to-charge ratio of the ions can be determined.

$$\omega_+ + \omega_- = \omega_c = \frac{q}{m} \cdot B \tag{2.1}$$

The motion of the ions is confined by a magnetic dipole field and a electrostatic field between a ring electrode and two end-cap electrodes as shown in figure 2.3.
With a segmented ring electrode a quadrupole excitation is applied to the ion motion

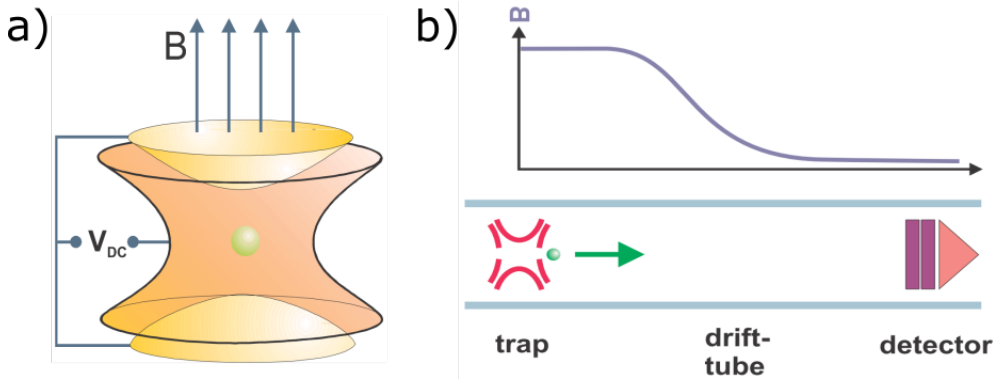

Figure 2.3.: a) Basic configuration of a Penning trap [Bollen, 2004]: The stored ion moves in a strong magnetic field. The movement in direction of the field is constraint by two end-caps with electrical repelling potential. The ring electrode can be segmented to enable quadrupole excitation of the ion movement. b) Schematic setup of TOF-ICR with the gradient of the magnetic field.

and the ions are subsequently released from the trap and fly through a magnetic field gradient to a particle detector. The field gradient converts the energy of the cyclotron motion into kinetic energy. The excitation frequency is scanned and the corresponding time-of-flight is measured. The time-of-flight is the lowest if the excitation frequency is in resonance with the mass dependent cyclotron frequency. This measurement technique is called Time-of-Flight Ion Cyclotron Resonance (TOF-ICR).
The mass resolving power is given by

$$R_m = \frac{m}{\Delta m} = \frac{\omega_c}{\Delta\omega_c} = \frac{\omega_c}{2\pi} T_{obs} \tag{2.2}$$

T_{obs} is the duration of the excitation or observation time. The width $\Delta\omega_c$ is determined by the Fourier limit dependent on T_{obs}. The achievable mass resolving power is limited for short-lived nuclei by their half-life. For a doubly charged ^{220}Ra-ion with an excitation duration equal to the half-life of 17.9 ms and a Penning trap with a 6 T magnet, the mass resolving power is 2500. The precision and mass resolving power for a given excitation time can be increased by increasing the charge state of the stored ions. At SMILETRAP mass measurements with q>40 have been performed [Bergström et al., 2002]. The time needed to increase the charge state is in the order of some 10 ms [Ettenauer et al., 2013]. With q=40 the mass resolving power for ^{220}Ra would be 100000. The most short-lived nuclei measured in a Penning trap so far is ^{11}Li with a half-life of 8.8 ms [Chaudhuri et al., 2014]. The advantage of the MR-TOF-MS compared with a Penning trap is the short measurement time, e.g. ^{220}Ra can be measured in less than 5 ms with a mass resolving power of 145000, see section 5.2.

2.4.2. Storage Rings

In an experimental cooler-storage ring, such as the ESR at GSI [Franzke, 1987], mass measurements of relativistic exotic ions produced and separated in-flight [Geissel et al., 1992] can be performed. The relation of the revolution frequency f of two isochronous ions with the mass-to-charge ratio (m/q) is given by [Franzke et al., 2008]

$$\frac{f_1 - f_2}{f_1} = -\frac{1}{\gamma_t^2}\frac{(m/q)_1 - (m/q)_2}{(m/q)_1} \tag{2.3}$$

γ_t is the so called transition point. For non-isochronous ions a frequency broadening Δf appears.

$$\frac{\Delta f}{f} = \frac{\Delta v}{v}(1 - \frac{\gamma^2}{\gamma_t^2}) \tag{2.4}$$

v is the velocity of the ions and Δv the velocity spread. Δf can be reduced in two ways, see also figure 2.4:

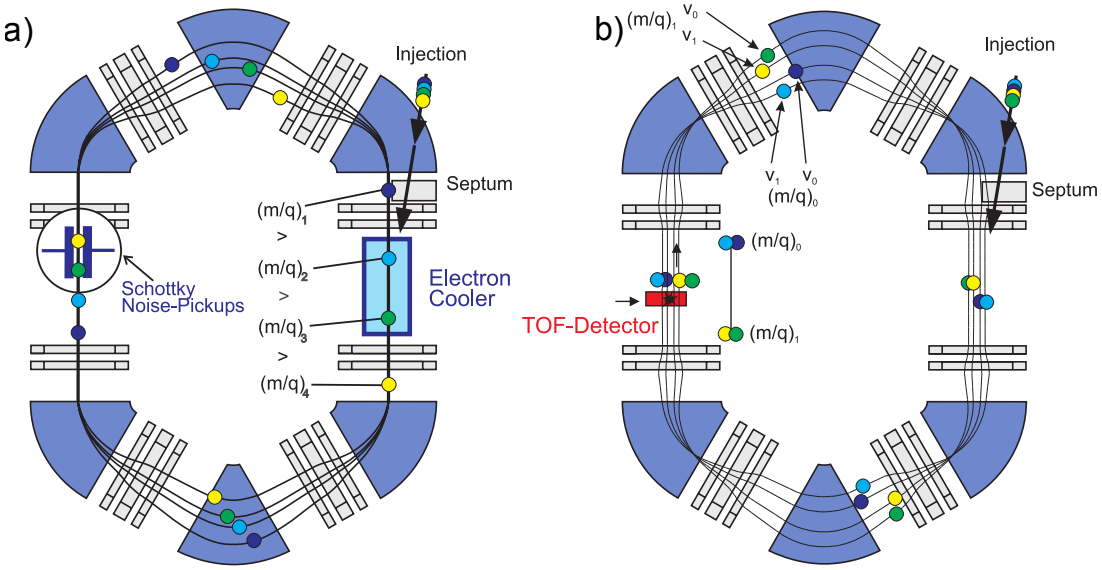

Figure 2.4.: Two methods of mass measurement with the ESR at GSI [Franzke, 1987]: a) In Schottky mass spectrometry the velocity spread of the stored ions is reduced via electron cooling to 10^{-7}. b) For the isochronous mass spectrometry the hot ions are injected in the ring at the transition energy γ_t, for which the revolution time is independent on the velocity spread

.

- **Schottky Mass Spectrometry (SMS)**
  The first method is to reduce the velocity spread of the stored ions with an electron cooler to a small value ($\frac{\Delta v}{v} < 10^{-7}$) [Radon et al., 1997]. All ions with the same (m/q) have the same revolution frequency, which can be measured by Fourier transformation of the signals from the Schottky noise detected by electrodes in the ring. A mass resolving power of $2 \cdot 10^6$ for low-intensity ions have been routinely achieved with accuracies of 10^{-7} [Litvinov et al., 2005]. A speciality are measurements down to single ions, because in this way ground and

isomeric states are naturally distinguished. The lower limit in the measurement is given by the cooling time of about 1 s, which limits the accessible short-lived nuclei.

- **Isochronous Mass Spectrometry (IMS)**
  The second method of mass measurements is applied to uncooled ions stored in the ring with a kinetic energy corresponding to γ_t [Wollnik, 1987, Hausmann et al., 2000]. The revolution frequency for one ion species is in first order independent on the velocity spread. The revolution frequency of the stored ions is about 1.95 MHz. Since no time is spent for cooling IMS enables mass measurement of very exotic nuclei with half-lives down to a few 10 μs. A mass resolving power of 250,000 has been achieved [Knöbel et al., 2016].

Although the mass resolving power of SMS [Chen et al., 2012] is higher than 400,000 which is presently achieved with the MR-TOF-MS [Plaß et al., 2015], the cooling time of 1 s is a limitation of SMS for short-lived nuclei with half-lives in the ms range. IMS can access nuclides with half-lives in the 10 μs range, but has restriction due to the smaller mass resolving power. The latter limitation is a big disadvantage to identify isomers with low excitation energies. In principle, MR-TOF-MS has the advantages of both experimental methods applied with the ESR.

2.4.3. Time-of-Flight Mass Spectrometer

The principle of time-of-flight mass spectrometry is illustrated in figure 2.5. An ion with mass m and charge qe starting on the electrical potential U has in the drift with potential $U_0 = 0$ the kinetic energy

$$\frac{1}{2}mv^2 = qeU \tag{2.5}$$

The velocity v is given by the effective length of the flight path s divided by the time-of-flight t in the mass spectrometer.

$$\frac{1}{2}m\frac{s^2}{t^2} = qeU \tag{2.6}$$

$$m = \frac{2qeU}{s^2}t^2 \tag{2.7}$$

The pre-factor on the right-hand side of the equation is constant and can be substituted. The dependence of the mass on the time-of-flight is then given by

$$m = at^2 \tag{2.8}$$

The mass resolving power R_m

$$R_m = \frac{m}{\Delta m} \tag{2.9}$$

is connected via equation 2.8 to the time-of-flight resolving power R_t

$$R_m = \frac{m}{\Delta m} = \frac{m}{|\frac{\partial m}{\partial t}|\Delta t} = \frac{t}{2\Delta t} = \frac{1}{2}R_t, \tag{2.10}$$

where Δm and Δt are the widths of the mass and the time-of-flight distributions, respectively. The mass resolving power is limited by the magnitude of time-of-flight, which depends on the length of the flight path. However, for practical reasons the length of a drift tube is about one meter. Figure 2.6 shows solutions to avoid this problem by an increase of the flight path. In figure 2.6 b) and c) ions move in multiple reflections on closed [Wollnik and Casares, 2003] or open [Verentchikov et al., 2005] paths and multiple turns on closed [Okumura et al., 2004] and open [Satoh et al., 2005] paths in figure 2.6 d) and e). The advantage of a closed path is the principally unlimited path length. The disadvantage is the non-unambiguous mass range, because

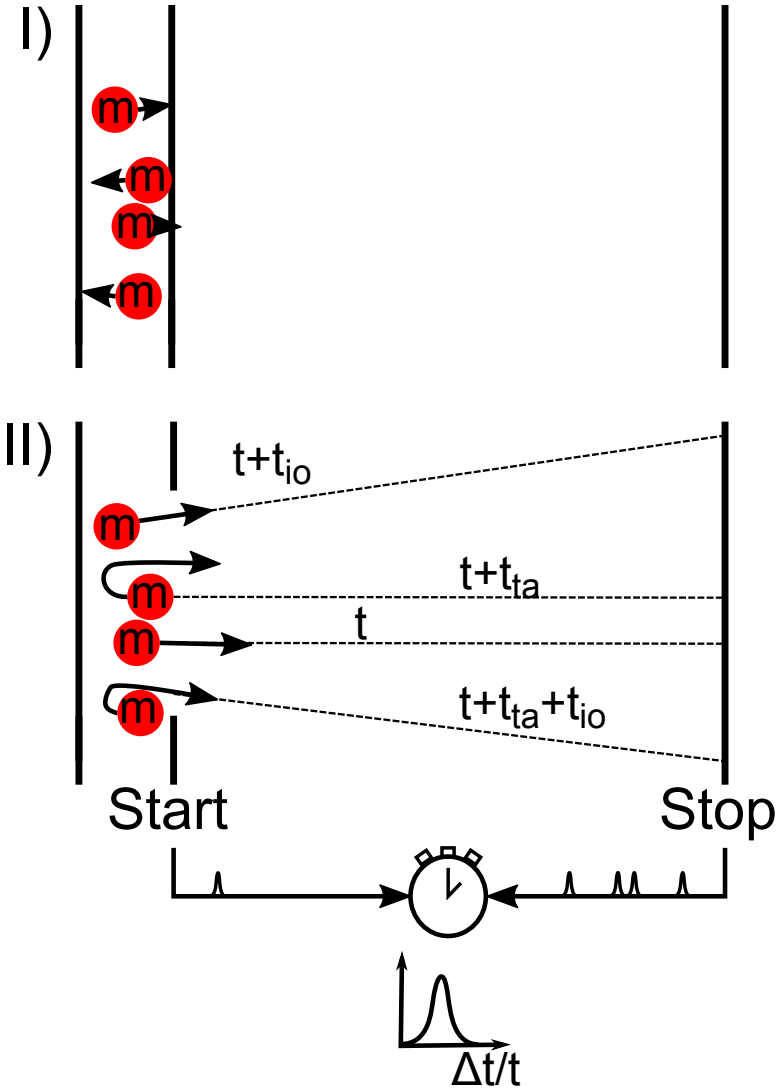

Figure 2.5.: Principle of time-of-flight mass spectrometry. I) Ions are stored in a trap and have a thermal velocity distribution. II) The trap is opened and ions with the same mass m and same kinetic energy fly along a path in a characteristic time t. Start- and stop-signals are generated at the opening of the trap and at the end of the path. The time difference between stop- and start-signal is the time-of-flight. It is characteristic for the mass m. The accuracy of the time-of-flight determination is determined by the turn-around time t_{ta} in the trap and ion optical aberrations t_{io}.

heavy ions are overtaken by lighter ones. The MR-TOF-MS bases on reflections on closed paths.

In a MR-TOF-MS the flight of the ions starts with the ejection from a trap. They

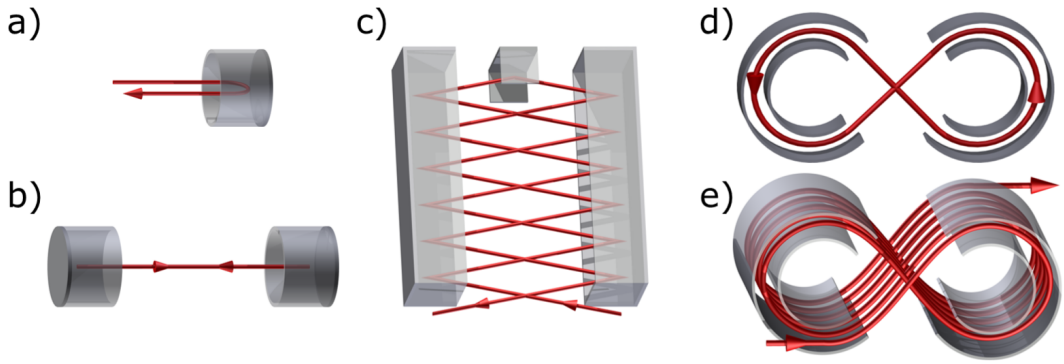

Figure 2.6.: Different methods to increase the flight path of a time-of-flight mass spectrometer: a) single reflection b) multiple-reflections on a closed path c) multiple-reflections on a open path d) multiple-turns on a closed path e) multiple-turns on a open path

fly N_{Turn} turns in the mass analyzer and are afterwards guided to a detector, as shown in figure 2.9.

The measured shape and width of a peak are determined by the turn-around time, the ion optical aberrations, the detector response and the data acquisition. The latter two contributions can be neglected compared to the first two ones. In the trap the ions have a Gaussian velocity distribution, therefore, also the peak shape caused by the turn-around is Gaussian. The turn-around time is the time ions with an opposite initial direction take to change to the right direction. The shape induced by the ion optical aberrations is typically not Gaussian-like. The time-of-flight spreads due the turn-around time Δt_{ta} and ion optical aberrations Δt_{io} are independent and cause a total peak width of Δt

$$\Delta t = \sqrt{(\Delta t_{ta})^2 + (\Delta t_{io})^2} \tag{2.11}$$

The time-of-flight and the errors can be written as time and time spread without turns in the analyzer t_0, Δt_0 and for N_{Turn} turns in the analyzer $N_{Turn} \cdot t_{Turn}$, $N_{Turn} \cdot \Delta t_{Turn}$. With this and equation 2.9 the mass resolving power can be written as

$$R_m = \frac{t_0 + N_{Turn} \cdot t_{Turn}}{2\sqrt{(\Delta t_0)^2 + (N_{Turn} \cdot \Delta t_{Turn})^2}} = \frac{\frac{t_0}{N_{Turn}} + t_{Turn}}{2\sqrt{(\frac{\Delta t_0}{N_{Turn}})^2 + (\Delta t_{Turn})^2}} \tag{2.12}$$

The total path length is in first order independent of the mass in electrostatic fields. Aberrations depend on the deviation from the ideal path and thus all ions with the same initial phase space have the same mass resolving power. Since the time-of-flight in the system is in first order independent of position and angles, R_m is constant for all ions in a mass spectrum, see figure 2.7. The shape, e.g. the width, scales linearly with the $\frac{m}{q}$ ratio.

For a high number of turns the mass resolving power is dominated by the time-of-flight and time spread of one turn in the analyzer.

The MR-TOF-MS can measure masses in a few 10 ms with mass resolving powers of

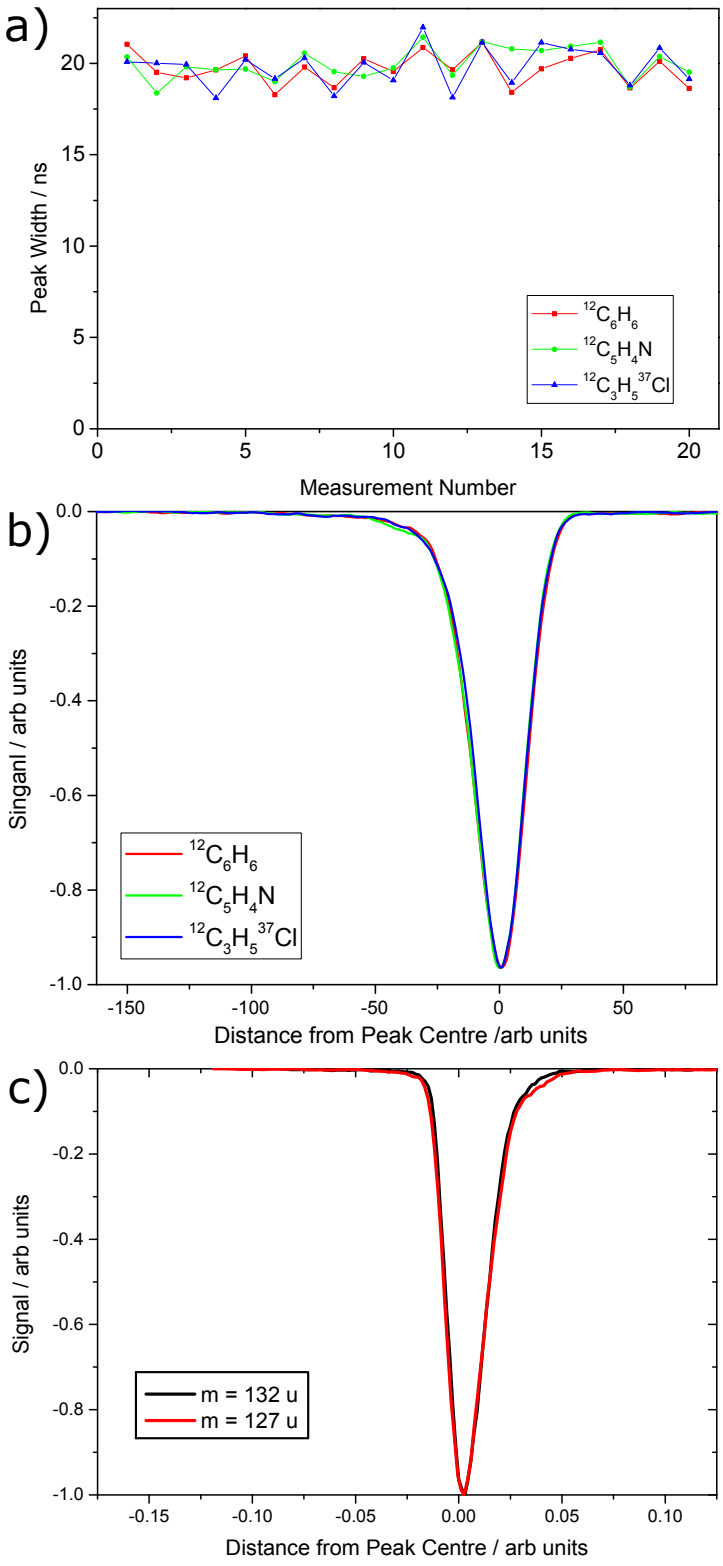

Figure 2.7.: a) Peak widths of an isobar triplet in 20 consecutive measurements. b) Peak shapes of the isobars in one of these measurements in comparison. c) Peak shapes of ^{132}Xe (masse m = 132 u) and $^{32}S^{19}F_5$ (m = 127 u), measured in the same spectrum, see also section 5.2. The spectrum of ^{132}Xe was shrunk by the factor $\frac{127}{132}$, to make the peak shapes comparable.

up to 400,000 [Plaß et al., 2015]. A mass value of short-lived nuclei can be determined with only 11 events, as shown in section 5.2 for ^{220}Ra with a half-life of 17.9 ms. The mass resolving power for the ^{220}Ra measurement was 145,000.

2.5. Analysis and Mass Calibration of the Multiple-Reflection Time-of-Flight Mass Spectrometer

A MR-TOF-MS performs like all mass spectrometer no absolute mass measurement, it always needs well known calibrant ions to calibrate the relation between the time-of-flight and the mass-to-charge ratio of an ion. The measured time is the sum of the time-of-flight of the ions and a constant delay t_0 caused by the signal propagation through the electronics.

$$t_{meas} = t + t_0 \tag{2.13}$$

The relation between mass and time-of-flight in equation 2.8 can be written as

$$m = a(t_{meas} - t_0)^2 \tag{2.14}$$

The constants a and t_0 must be determined through the measurement of the time-of-flight of two known calibrant ions or one calibrant ion and a direct measurement of t_0. For the case of very long time-of-flights and a small t_0 ($t_{meas} \gg t_0$), the delay t_0 can be neglected and only one calibrant ion is needed, if the mass difference between ion of interest and calibrant is not to large [Ito et al., 2013].

The energy of the ions is normally so low that relativistic effects can be neglected. An estimation of the error caused by relativistic effects is given in section 2.5.1. In equation 2.14 it is assumed, that the ion of interest and the calibrant ion make the same number of turns in the mass analyzer. Unfortunately not always is a calibrant in the desired mass region available. For this case a different calibration function is needed (section 2.5.2) to calibrate with different turn numbers. Section 2.5.3 shows how the calibration of time-of-flight spectra is used to correct drifts in the time-of-flight for a given mass-to-charge ratio caused e. g. by instabilities of the electronics.

2.5.1. Relativistic Mass Calibration

In section 2.4.3 the relation between time-of-flight and the mass of an ion was derived in a classical, non-relativistic ansatz. The following section estimates the discrepancy to a relativistic ansatz. Therefore, we take the non-relativistic formula for the mass calibration, equation 2.8, and replace mass m with the relativistic mass γm_0.

$$\gamma m_0 = at^2 \tag{2.15}$$

γ is the Lorentz factor

$$\gamma = \frac{1}{\sqrt{1 - \frac{v^2}{c_0^2}}} \tag{2.16}$$

v is the velocity of the ions and c_0 the speed of light. If γ is approximately the same for all ions in the spectrum, equation 2.15 can be rewritten as

$$m_0 = \frac{a}{\gamma} t^2 = a_{rel} \cdot t^2 \tag{2.17}$$

This is the case for all ions with the same velocity like for isobars. For ions with different mass-to-charge ratios the change in γ is directly the uncertainty in mass. Figure 2.8 shows the calculated errors for different kinetic energies and mass-to-charge ratios. The relative errors for measurements with kinetic energies of $\leq$ q*1300 eV

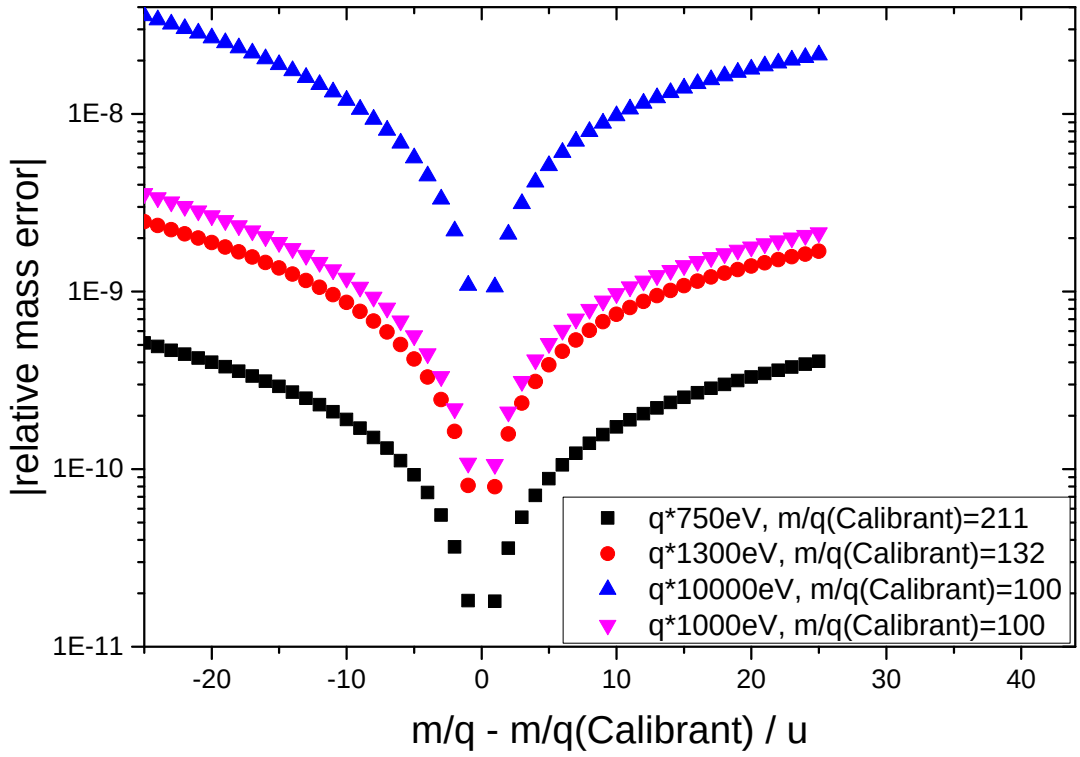

Figure 2.8.: Absolute values of the relative mass errors of ions with a mass-to-charge ratio m/q, that differs from the m/q of the calibrant. Shown are calculations for different kinetic energies of the ions and calibrants.

are below 10^{-8} and can be neglected. These kinetic energies correspond to the measurements in the sections 5.1 and 5.2. These effects are even more reduced in reality, since the ions do not have always high kinetic energies, but slow down in the reflectors of the MR-TOF-MS.

2.5.2. Mass Calibration with Different Turn Numbers

An issue of multiple-reflecting time-of-flight mass analyzers with a closed path is that from a certain number of turns on lighter ions overtake the heavier ones, which leads to ambiguous time-of-flight spectra. The unambiguous mass range m_{min} to m_{max} is limited by the number of turns N_{Turn} in the mass analyzer [Yavor et al., 2015]

$$\frac{m_{max}}{m_{min}} \leq \left(\frac{N_{Turn} + \lambda_{inj}}{N_{Turn} + \lambda_{inj} - (1 - \lambda_{mir})} \right)^2 \tag{2.18}$$

$\lambda_{inj} = \frac{t_{inj}}{t_{Turn}}$ is the time ions are flying from the trap to the second mirror. t_{Turn} is the time for one turn in the mass analyzer for a given mass-to-charge ratio. $\lambda_{mir} = \frac{t_{mir}}{t_{Turn}}$ is the time where ions are influenced by pulsing the ion mirrors, compare figure 2.9. For the case that ions make different number of turns in the mass analyzer equation 2.7 must be modified [Haettner, 2012]. For this we divide the flight path in two parts, see figure 2.9

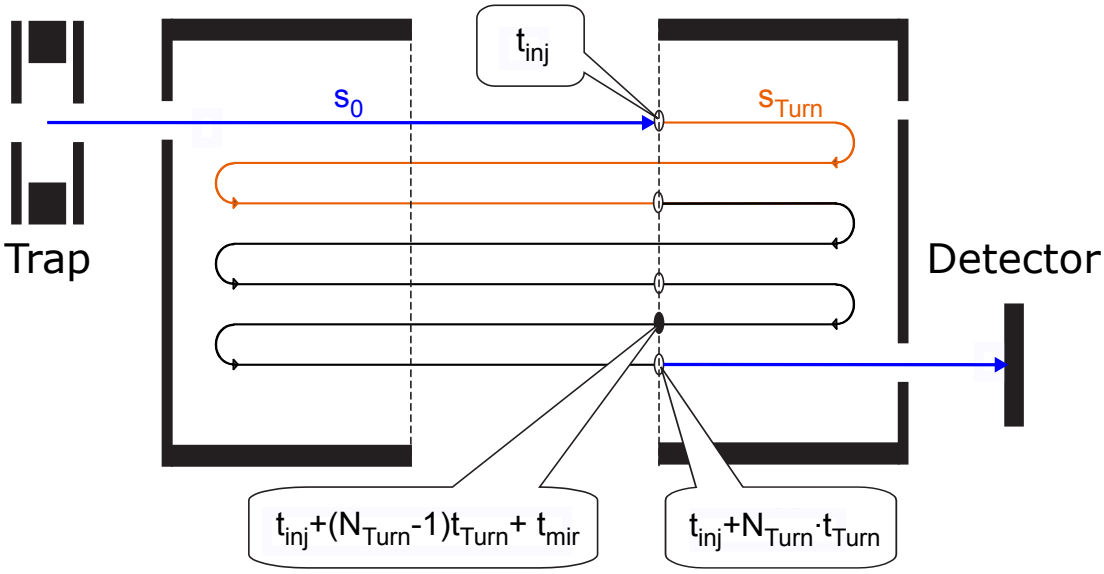

Figure 2.9.: Scheme of the flight path in the MR-TOF-MS [Yavor et al., 2015]. The path is split into two parts: from the trap directly to the detector (s_0) and the turns in the mass analyzer ($N_{Turn} \cdot s_{Turn}$). For the maximum unambiguous mass range, the two ions indicated by solid and empty circles represent the minimum and maximum mass-to-charge ratios m_{min} with N_{Turn} turns and m_{max} with $(N_{Turn} - 1)$ turns, respectively.

$$s = s_0 + N_{Turn} \cdot s_{Turn} \tag{2.19}$$

s_0 is the effective length of the flight path from the trap to the detector without turns, s_{Turn} the effective length of one turn in the mass analyzer and N_{Turn} the number of turns. Using equation 2.19 for equation 2.7 follows

$$m = \frac{2qeU}{(s_0 + N_{Turn} \cdot s_{Turn})^2} t^2 \tag{2.20}$$

$$m = \frac{2qeU}{s_0^2(1 + N_{Turn}\frac{s_{Turn}}{s_0})^2}t^2 \tag{2.21}$$

With $\frac{s_{Turn}}{s_0}$ and $\frac{2qeU}{s_0}$ substituted by b and c the relation 2.14 between mass and time-of-flight can be rewritten as

$$m = \frac{c(t_{meas} - t_0)^2}{(1 + N_{Turn} \cdot b)^2} \tag{2.22}$$

This formula needs three different calibrants with at least two different numbers of turns to determine the constants b, c and t_0. For the case ($t_{meas} \gg t_0$) t_0 can be again neglected as before, if the mass difference between ion of interest and calibrant ion is not to large.

2.5.3. Drift Correction

For the equations 2.14 and 2.22 we implied a perfect mass spectrometer with a constant effective length of the flight path, but in reality thermal expansion of mechanical components and instabilities of electrical power supplies change the length. The largest impact on the time-of-flight of the ions have the electrostatic mirrors because the ions test these electric fields up to several hundreds times during their measurement. Thus the length of one turn in the mass analyzer depends on the measurement time $s_{Turn} = s_{Turn}(T)$. In comparison to this the fluctuations of path length s_0 are larger, but the ions see them only once.
The drift of the time-of-flight can be corrected in two ways, compare figure 2.10. The first method is to split the measurement in time fragments. The time-of-flight spectrum of each segment is shifted till the calibration peaks are at the same position, which corrects for the drift. The time-of-flight spectra of all segments are then added together and the sum spectra is calibrated. The second method is to split the measurement in time fragments and correct the drift by determining position of the calibration peaks in each time-of-flight spectrum. Then each spectrum is individually calibrated and the drift corrected mass spectra are added together.
For this thesis the second method was chosen, because it can be easily included in the data analysis. In the following it is called Time Resolved Calibration. Therefore, the time dependent parameters a and b in the equations 2.14 and 2.22 are calculated from the time-of-flight of the calibration peak. The time independent parameters t_0 and c can be measured in a different measurement, which reduces the required number of calibrants, that must be measured together with the ions of interest to one.
Two kinds of calibrations can be used : (i) internal and (ii) external calibration. In the case of (i) a calibrant ion source is permanently on and for each measurement cycle a or b can be determined by determining the time-of-flight of the calibrant. In contrast to that in (ii) the calibrant ion source is only periodically switched on and the time-of-flight of the calibrant is linear interpolated between the segments with ion source on.
Case (i) is preferable, because the correction is more accurate. Nevertheless there are

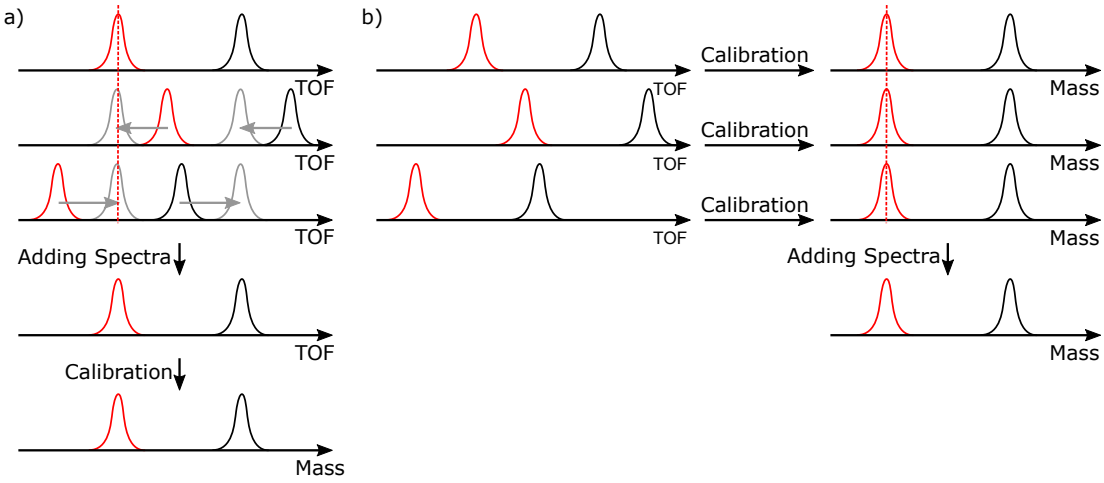

Figure 2.10.: Principle of the drift correction. a) First method: The measurement is split into time segments. The time-of-flight (TOF) spectrum of each segment is shifted till the calibration peaks (red) are aligned. The spectra are then added together and calibrated to get the drift corrected mass spectrum. b) Second method: The measurement is again split in time segments. The TOF of the calibration peak (red) of each segment is determined and each spectrum is calibrated separately. The drift corrected mass spectra are then added together.

reasons not use (i), if the peaks of calibrant and ion of interest are overlapping. In the case of pulsed production of exotic nuclei at an accelerator facility the calibrant ion source can be switched on between the pulses of exotic nuclei.

3. Experimental Setup

This chapter provides an overview of the experimental setup of the FRS Ion Catcher at the high-energy facility at GSI (figure 3.1) which is a test bench for the Low-Energy Branch of the Super-FRS [Geissel et al., 2003, Geissel et al., 2013] at FAIR. The FRS Ion Catcher consists of a gas filled cryogenic stopping cell (CSC) [Ranjan et al., 2011, Purushothaman et al., 2013, Reiter, 2015], a radio frequency quadrupole (RFQ)-based low-energy beamline with detectors for beam diagnostics (DU) [Reiter, 2011] and the multiple-reflection time-of-flight mass spectrometer (MR-TOF-MS) [Dickel, 2010, Dickel et al., 2015a]. CSC, DU and MR-TOF-MS are located in the experimental area at the final focus (F4) of the FRS (figure 3.3). The measurements with the MR-TOF-MS and the analysis of the mass spectra are the central parts of this doctoral thesis.

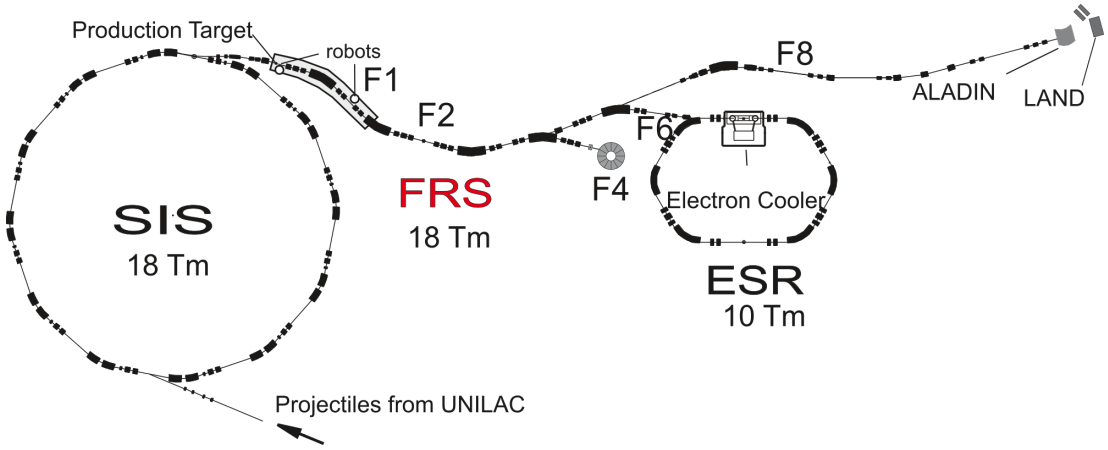

Figure 3.1.: Overview of the present high-energy facility at GSI [Geissel et al., 2016]. The FRS Ion Catcher is installed at the final focal plane (F4) of the FRS.

3.1. Fragment Separator

The FRS [Geissel et al., 1992] can separate nuclei in-flight which are produced via projectile fragmentation or fission of relativistic heavy-ions in a production target at the entrance of the FRS. These nuclei can be spatially separated with a two-fold magnetic rigidity analysis combined with energy loss in thick layers of matter. The layers of solid matter have a variable thickness and shape and are called "degraders". They are normally placed in the dispersive central focal plane of the FRS. An achromatic degrader preserves the overall ion optical achromatism of the FRS and provides

the best spatial resolving power for the separated exotic nuclei. A monoenergetic degrader bunches the energy distribution of the fragments and enables in this way the complete stopping of ions in thin layers of matter.
For the experiments of the FRS Ion Catcher it was necessary to use a mono-energetic degrader, so that separated isotopes can be efficiently stopped in the helium filled stopping cell with an areal density of 3 mg/cm^2 . The mean range of the ions to be stopped can be adjusted with a variable homogeneous degrader (VH-Degrader) in front of the CSC.
Scintillator detectors (SCI), time-projection-chambers [Janik et al., 2011] and multiple sampling ionization chambers [Pfützner et al., 1994] (MUSIC) at the middle and final focal planes enable a full identification of all ions flying through the FRS by measuring their time-of-flight, charge, magnetic rigidity and energy loss in matter. For a verification of the particle identification well-known α-emitting isotopes are measured in a double-sided silicon strip detector [Farinon et al., 2011] (Alpha Tagger) in front of the CSC. The CSC and the MR-TOF-MS are located at the final focal plane of the FRS, see figure 3.3.

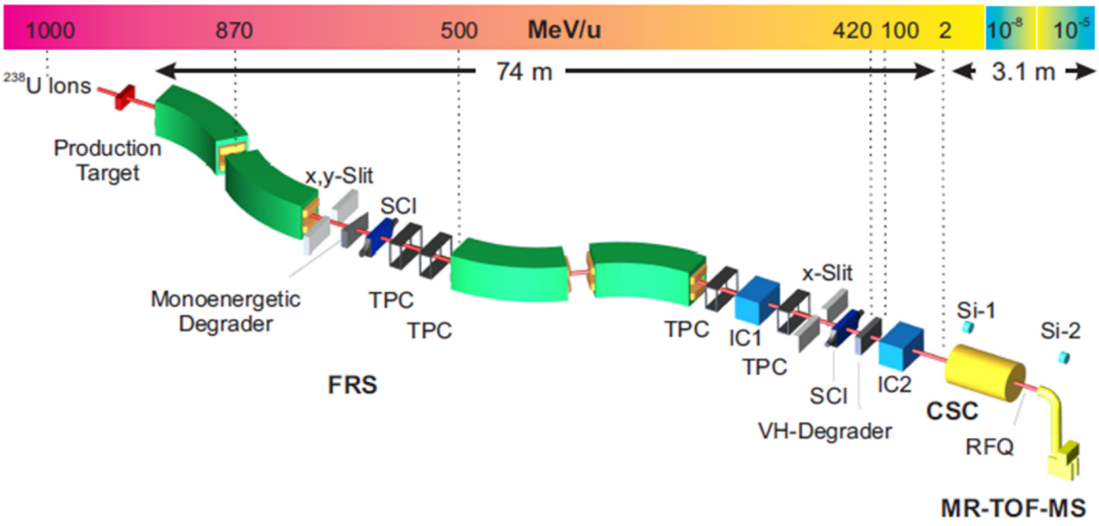

Figure 3.2.: The experimental setup of the FRS Ion Catcher at the fragment separator (FRS) [Purushothaman et al., 2013] with degraders and detectors for particle identification at the central and final focus planes, the cryogenic stopping cell (CSC), a RFQ-based low-energy beamline with detectors for ion diagnostics and a multiple-reflection time-of-flight mass spectrometer (MR-TOF-MS). The colour band indicates the kinetic energy of ions in different stages of the setup.

3.2. Cryogenic Stopping Cell

The energy bunched ions produced and separated with the FRS must be slowed down and thermalized in order to perform high-accuracy measurements. The final slowing down is achieved by atomic collisions of the fast ions with Helium gas in the cryogenic

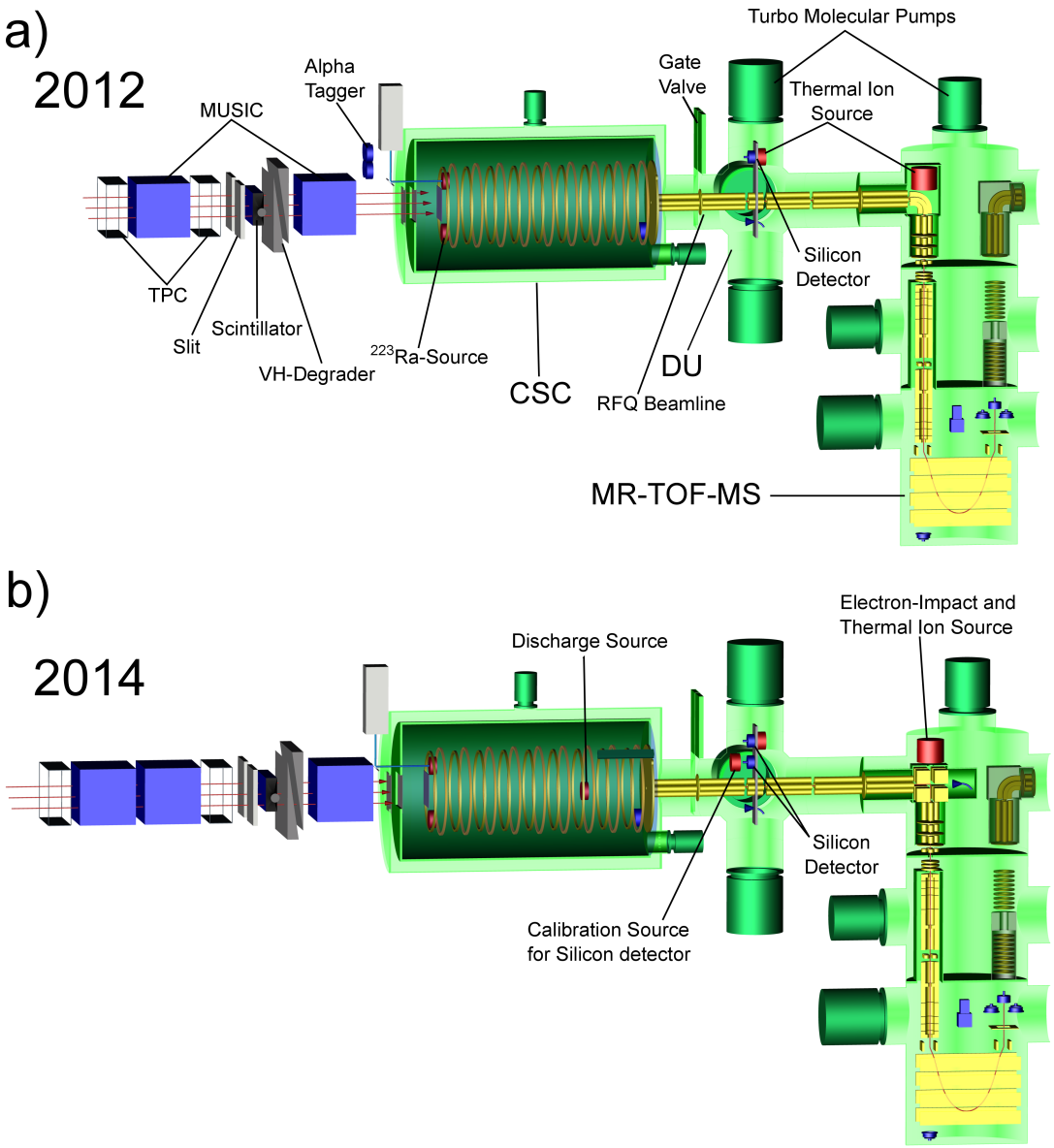

Figure 3.3.: Setup of the FRS Ion Catcher at the final focus of the FRS during the experiments 2012 (a) and 2014 (b). The time-projection-chambers (TPC), multiple sampling ionization chambers (MUSIC), the scintillator and silicon detectors enable the particle identification of ions transported through the FRS. The mean atomic range of these ions can be adjusted with the homogeneous variable degrader to stop them in the CSC. Red: ion sources, Blue: detectors, green: vacuum components. The most important changes between 2012 and 2014 are improvements in the CSC, the RFQ beamline [Reiter, 2015] and the MR-TOF-MS, compare section 3.4.2.

stopping cell. The stopping cell consists of two vacuum chambers, see figure 3.4. The outer one is at room temperature and generates a vacuum for thermal isolation of the inner chamber. The inner one contains the ultra pure Helium gas at a pressure of 70-100 mbar. It is surrounded by cooling channels filled with a cold Helium gas supplied by a cryocooler. The cooling system [Ranjan et al., 2015] can reach temperatures down to 60 K, which freezes out most of the impurities in the stopping gas. Both chambers have an entrance window made of stainless steel with a thickness of 100 μm each. The performance characteristics are listed in table 3.1.

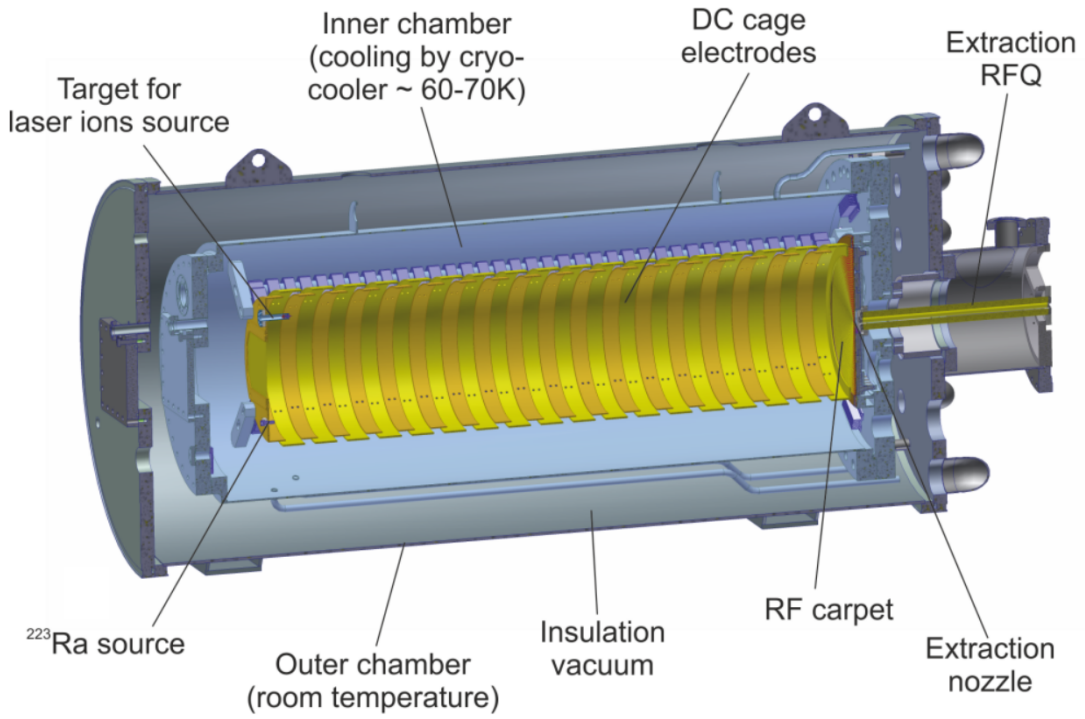

Figure 3.4.: Drawing of the cryogenic stopping cell. The stopping volume is surrounded by an additional vacuum chamber for thermal insulation and can be cooled down to 60 K. Thermalized ions are guided via an electrical field generated by the DC cage electrodes to the RF carpet, where electrical RF and DC fields transport the ions to the extraction nozzle. For commissioning of the CSC and calibration of MR-TOF-MS a ^{223}Ra-source is located at the beginning of the DC cage. [Reiter, 2015]

After stopping in the helium gas the ions are guided by an electrical field generated by a cage of DC electrodes to the RF carpet at the exit side of the cell. RF voltages are applied to the ring electrodes of the RF carpet to create a repulsive electrical field. In addition, DC voltages are applied to the rings to guide the ions to the nozzle placed in the middle of the RF carpet. The ions are extracted through the gas flow into the extraction radio-frequency quadrupole (RFQ) [Dawson, 1976].
Several ion sources are placed inside the inner chamber for calibration and commissioning. A ^{223}Ra recoil source with a half-life of 11.4 days provides heavy α and β-decaying ions. A discharge source in the middle of the DC cage can generate high ion currents by ionizing the buffer gas and material from the discharge electrodes [Greiner and Miskun, 2016].

Length of Stopping Volume	104.5 cm
Maximum Acceptable Beam Diameter	25 cm
Areal Density	3.5 - 5.6 $\frac{mg}{cm^2}$ He equivalent
Temperature	60 - 90 K
Survival and Extraction Efficiency	80 %
Extraction Time	22.7 ms

Table 3.1.: Characteristics of the cryogenic stopping cell [Reiter, 2015]

3.3. RFQ Beamline and Diagnostics Unit

For the transport of the ions a novel non-electrostatic concept was implemented [Plaß et al., 2007]. Ions extracted from the CSC are transported to the MR-TOF-MS with RFQs made out of resistive material [Takamine, 2007, Simon, 2008]. The RFQ rods have a diameter of 11 mm and a distance of 10 mm. As shown in figure 3.5 the second and third RFQ are moveable which enables to separate the vacuum system with a gate valve. This is advantageous for maintenance or to move detectors in the beamline for particle diagnostics and decay spectroscopy of extracted ions [Reiter, 2015]. For this tasks a channeltron and two silicon surface barrier detectors are installed on a moveable detector sled. For calibration the silicon detectors can be moved in front of a mixed α-source containing ^{239}Pu, ^{241}Am and ^{244}Cm atoms. An additional thermal alkali ion source (Heat Wave Labs TB-118) can be used for commissioning and calibration of the MR-TOF-MS.
Three turbo-molecular pumps with a total pumping speed of 4000 l/s to reduce the Helium pressure coming from the CSC down to the required working pressure of about 10^{-2} mbar suitable for the RFQs.
The first RFQ, the so called extraction RFQ, has two operating modes. Either it transports ions within a wide mass range or it can also be used as a narrow band mass filter [Paul and Steinwedel, 1953] to preselect ions extracted from the CSC [Miskun, 2015].

3.4. Multiple-Reflection Time-of-Flight Mass Spectrometer

The high-resolution part of the FRS Ion Catcher is the MR-TOF-MS, which was mainly constructed and commissioned by T. Dickel [Dickel, 2010, Dickel et al., 2015a]. This compact device fits together with its electronic components in a volume of 2 m x 1.9 m x 0.85m. The ion-optical part is mounted in a vacuum chamber which consists of three CF250 vacuum crosses and a CF250 tube. The complete vacuum system is shown in figure 3.6.
The upper vacuum cross is pumped by a turbo-molecular pump (Varian Turbo-V

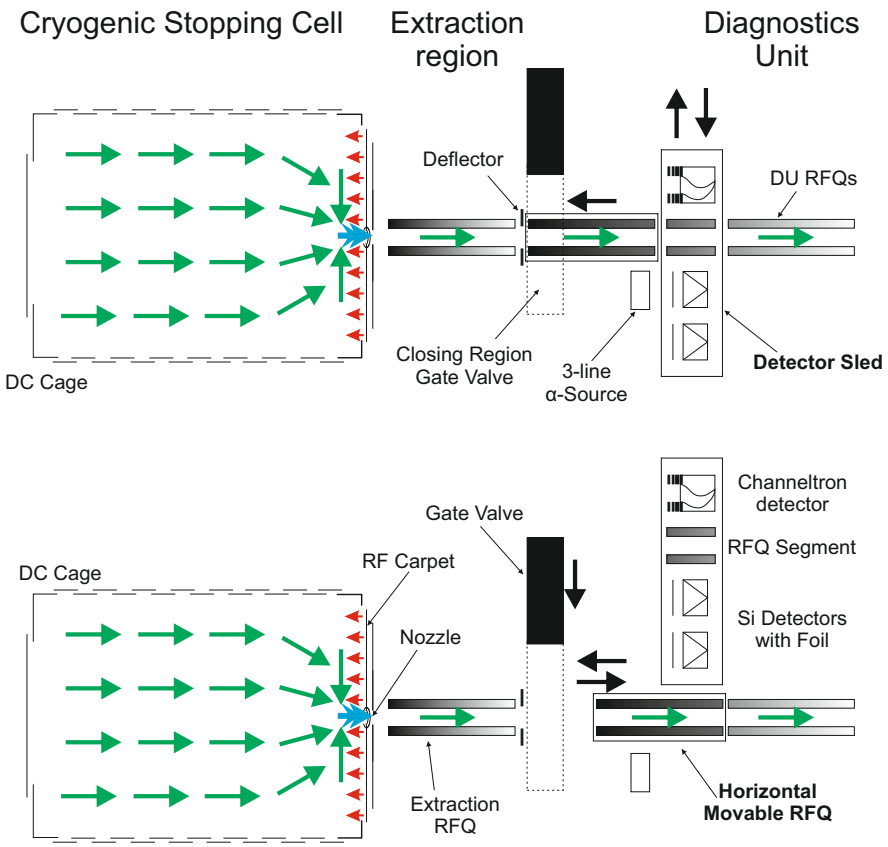

Figure 3.5.: Scheme of the CSC and RFQ beamline. Ions extracted from the CSC can be transported to a detector on a moveable sled in the diagnostics unit or with a RFQ segment to the MR-TOF-MS (top). For maintenance the vacuum chambers of CSC and MR-TOF-MS can be decoupled with a gate valve. Therefore, the detector sled is moved out of the beamline and the horizontal RFQ is moved out of the area of the gate valve (bottom). [Reiter, 2015]

1001 Navigator). The pressure is regulated by a Helium inlet inside the RFQ and trap system. The same inlet can be used to vent the system with dry nitrogen for maintenance. A second gas inlet delivers a mixture of Xe and SF_6 gas for the internal electron impact ion source directly in the volume of the upper cross. For reducing the pump down time of the encapsulated RFQ and trap system a remote controlled pumping valve can be opened to increase the conductivity between encapsulated RFQs and the upper cross. The middle cross is a differential pumping stage and has a turbomolecular pump (Varian Turbo-V 551 Navigator) to reduce the gas flow coming from the trap system. The lower cross containing the mass analyzer has two turbomolecular pumps (Varian Turbo-V 551 Navigator, Pfeiffer HiPace 700). The rough vacuum is generated by a scroll pump (Varian Triscroll 300).

For pressure readout Pirani and cold cathode gauges (Pfeiffer PKR 251) are used in upper and middle cross. In the lower one a combination of Pirani and hot cathode gauge (Pfeiffer PBR 260) is used. Typical operation pressures are given in table 3.2.

The schematic drawing in figure 3.7 shows the ion optical setup. Ions of interest coming from the DU are guided through two RFQs to a RFQ-based beam switch-

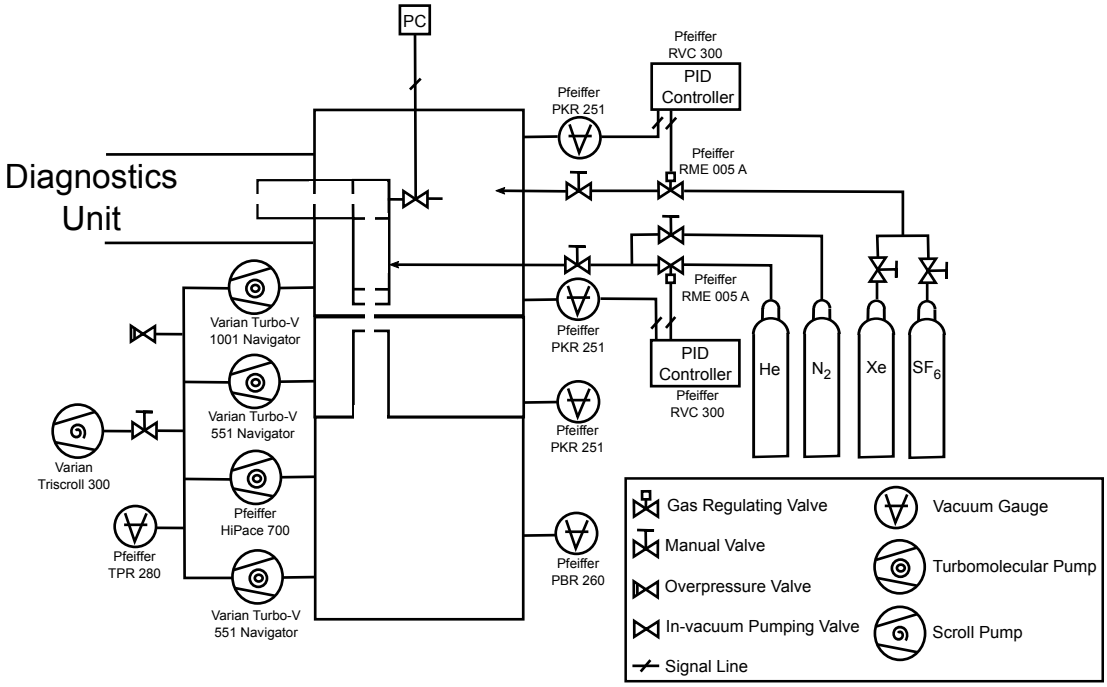

Figure 3.6.: Vacuum and gas inlet system of the MR-TOF-MS. Helium is used as cooling gas in the RFQs and trap system, nitrogen for venting the vacuum chamber. The inlet for Xe and SF_6 was installed 2014 for generating calibrant ions with the internal electron impact ion source. The pressure in the MR-TOF-MS is regulated through the helium pressure around trap and RFQ system.

	Typical Pressure [mbar]
Upper Cross	$8.9 \cdot 10^{-5}$
Middle Cross	$1.7 \cdot 10^{-6}$
Lower Cross	$1.3 \cdot 10^{-7}$

Table 3.2.: Typical pressures in the different parts of the MR-TOF-MS in 2014. The values are corrected for the gas type dependent measurement of the used vacuum gauges. The pressure in the RFQ system can not be measured.

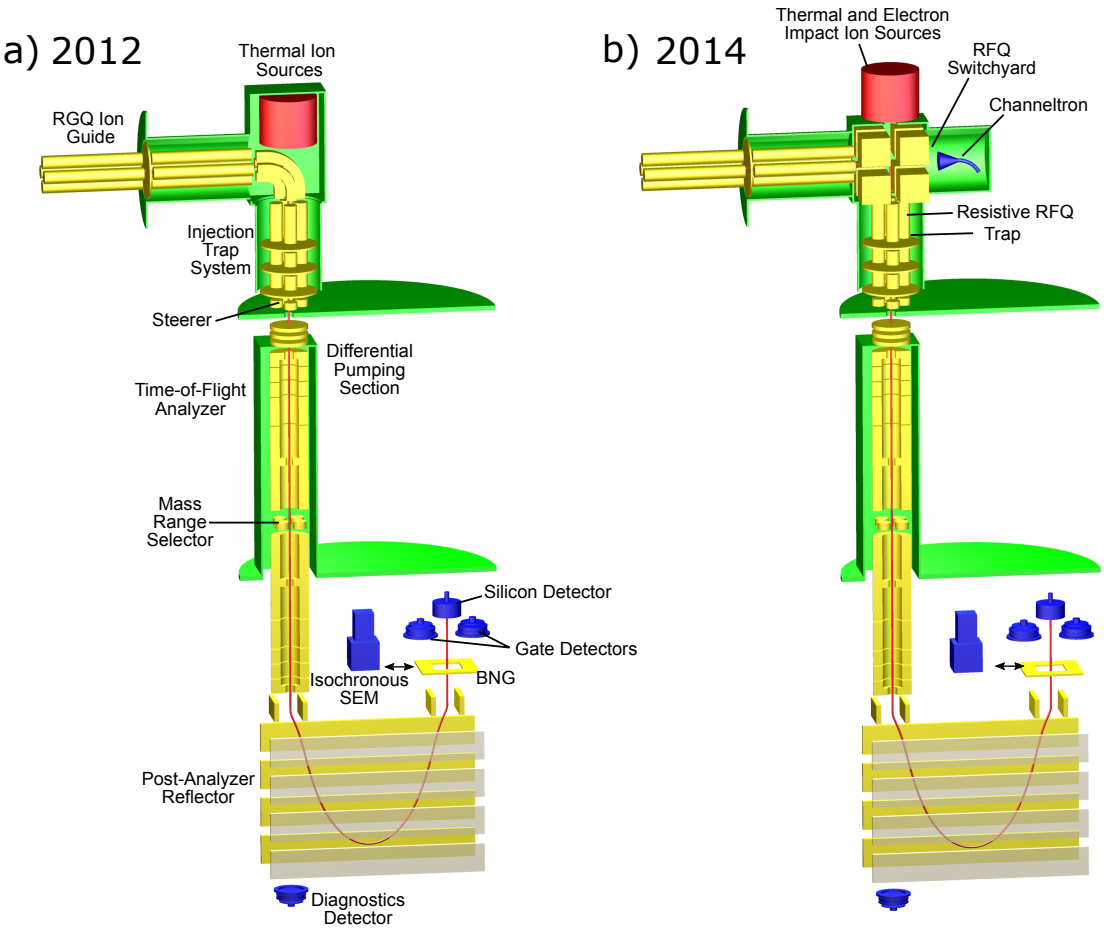

Figure 3.7.: Schematic drawing of the MR-TOF-MS for the status 2012 (a) and 2014 (b). Green are differential pumping elements, yellow are ion optical parts, blue are detectors and red are ion sources. The BNG, silicon detector and isochronous SEM are mounted on a moveable detector sled. Major changes of the hardware installed between 2012 and 2014 are indicated in panel b).

yard [Greiner, 2013, Plaß et al., 2015], see also section 3.4.2. There the ions can be directed to a channeltron detector (Photonis 5901 Magnum Electron Multiplier for commissioning) or together with calibrant ions from the internal thermal or electron impact ion source to a third RFQ and the trap system [Jesch, 2008, Dickel, 2010]. All RFQs have rod diameters of 11mm and rod distances of 10 mm and are made of a resistive material like the switchyard and the RFQs in the beamline .
In the trap system the ions are accumulated in a first linear Paul trap [Paul and Steinwedel, 1953] and ejected in a bunch to a second trap, where the ions are cooled and stored until the last trap is emptied and pulsed on a low electrical potential. Then the ions are transported in this trap and the electrical potentials of trap and ions are lifted from near ground to originally 750 V [Dickel, 2010, Dickel et al., 2015a]. This potential could be further increased in 2014 to 1300 V by improving the electronics [Ayet et al., 2014, Plaß et al., 2015].
Depending on the operation mode of the MR-TOF-MS, see figure 3.8, the ions either fly directly to the detector or make a certain number of turns in the time-of-flight

analyzer. The additional flight path in the analyzer increases the spatial separation between ions of different masses and thus the mass resolving power of the device. For a large number of turns lighter ions make higher number of turns than the heavier ones. To prevent this a mass range selector is installed in the middle of the analyzer. It is switched on temporary to deflect ions of unwanted mass and therefore clean the ion population from contamination.
After this the ions are deflected by electrical dipoles towards the detector and pass the post-analyzer reflector which shifts the energy-time focus of all ions to the detector [Yavor et al., 2015]. Energy-time focus is the point where ions with the same mass-to-charge ratio are at the same time independent of their energy. As detector two different systems are available, mounted on a movable sled. The first one is a MagneTOF DM167 (SGE Analytical Science Pty Ltd.) for time-of-flight measurements. The second one is a combination of a fast switchable Bradbury-Nielson ion gate (BNG) [Bradbury and Nielsen, 1936, Yoon et al., 2007], two microchannel plate (MCP) detectors [Wiza, 1979] and a silicon surface barrier detector (Ortec Ultra BU-016-150-100). The BNG let ions with a choosen time-of-flight and corresponding mass-to-charge ratio pass and transmit them to the silicon detector. All other ions are deflected by applying high voltages with different signs to thin wires, which act as dipole deflectors. These unwanted ions are steered to the MCP detectors where their time-of-flight can be measured. The MR-TOF-MS can run with repetition rates up to 400 Hz which corresponds to a measurement duration of only 2.5 ms. For longer measurement durations a mass resolving power of $6 \cdot 10^5$ has been reached. It is sensitive for single ions and can handle up to 10^6 ions per second [Dickel et al., 2015a]. For running the MR-TOF-MS more than 130 DC, RF and pulsed voltages are required. An overview of important voltages and their typical values is given in table 3.3. DC voltages below 60 V are generated by in-house made and commercial power supplies. High-voltage power supplies are completely commercial ones. The hardware for RF voltage generation, see [Jesch, 2008] and section 3.4.2, is completely in-house made as well as the high voltage switches.
The sequence control is regulated by a FPGA-based TTL-generator as shown in [Jesch, 2016]. It has 32 channels which can be triggered on each other, input signals or virtual channels.

3.4.1. Data Acquisition

Signals from the MagneTOF detector are amplified [Ayet San Andres, 2014] and recorded by a time-to-digital converter (TDC) (Ortec Model 9353) either in list-mode (see also appendix A.1) with a time resolution of 100 ps or in histogram mode. For the first mode the original TDC software (Digitizer) was used and for the second one the software MAc, developed by [Pikhtelev, 2014] and further improved in [Bergmann, 2015].
MAc is not only a software for data acquisition but also for on- and offline data analysis. It enables online the calibration of TOF spectra and provides a database for identification of peaks. Offline the time resolved calibration can be performed as well

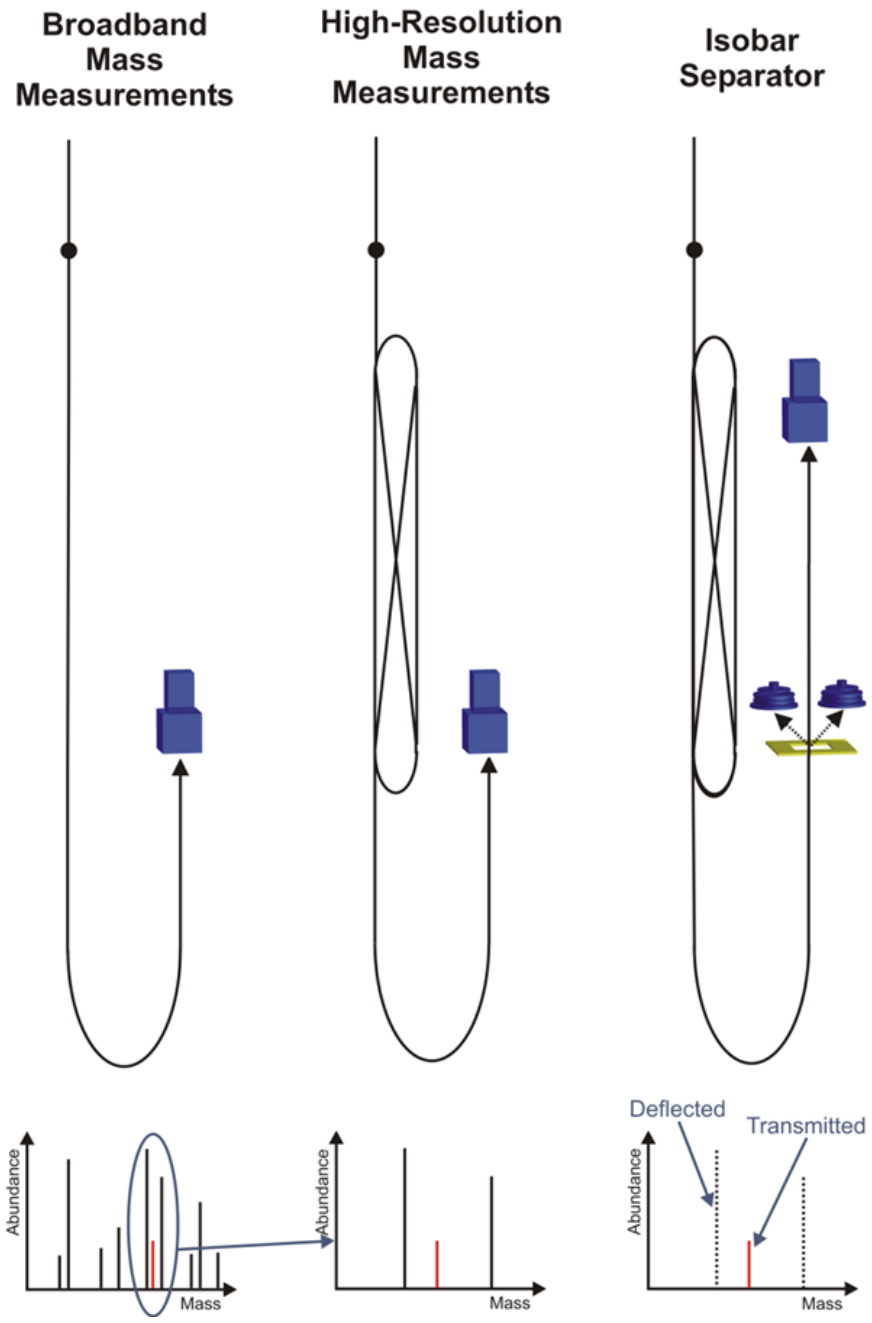

Figure 3.8.: Different operating modes of the MR-TOF-MS. Broadband mass measurements [Dickel et al., 2015a]: Ions fly directly from the trap system to the detector. This mode provides a broad mass spectrum with many ions window and has a mass resolving power of several 10^3. High-resolution mass measurements [Scheidenberger et al., 2001]: The ejected ions make a selected number of turns inside the time-of-flight analyzer before they impinge on the detector. Therefore, the measured mass range in the spectrum is reduced and the mass resolving power increased to several 100,000. Isobar Separator [Plaß et al., 2008]: It is also a high-resolution mode but the detector is replaced by a Bradbury-Nielson gate to deflect unwanted ions. In this way the separated ions can either be directly investigated in the detector or can be transported to other experimental areas. The schematic mass spectra at the bottom demonstrate the characteristics of the different modes [Plaß et al., 2013].

	DC Volt. [V]	AC Volt. [Vpp]	Freq. [MHz]
Sine RF for RFQs		400 - 500	1.035
Sine RF for switchyard		400 - 500	1.278
Rectangular RF for trap system		90 - 120	2.0
Potential of last trap	1300		
Potential depth of last trap	30		
Extraction potential of last trap	$\pm$ 230		
Potential of lens between trapr and time-of-flight analyzer	2300		
Mirror electrodes of mass analyzer open	404 0		
Mirror electrodes of mass analyzer closed	1751 1237		
Potential of lens in time-of-flight analyzer	-3386		
Mass range selector	-100 - 100		
Potential of lens between time-of-flight analyzer and post-analyzer reflector	-1000		
Electrodes in post-analyzer reflector	0 -1806 348 1234 1564		
Lens potential in front of the detector system	-500		
Operating voltage of TOF detector	-3000		

Table 3.3.: Overview of important operation voltages and their typical values in the MR-TOF-MS in 2014. The amplitude of AC voltages is given as peak-to-peak voltage and the corresponding frequency in MHz. The drift potential of ions is ground.

as data filtering or smoothing.
Beside the data acquisition MAc controls the measurement sequence with the generation of TTL signals and can optimize voltage settings of the MR-TOF-MS autonomously under different aspects like maximum mass resolving power or transmission efficiency.

3.4.2. Improvements of the MR-TOF-MS

In the frame work of this thesis several parts of the MR-TOF-MS have been improved.

New Resistive RFQ and Longer Trap Electrodes

The RFQ system consisted originally of 3 RFQs made of resistive plastic and a metal RFQ with LINAC electrodes [Loboda et al., 2000] to create a drag field along the RFQ [Dickel, 2010]. The electric fields in the latter depend strongly on manufacturing precision and positioning of the LINAC electrodes. Therefore, it was exchanged with a one made out of carbon filled plastic.
The length of the electrodes in the linear Paul trap behind the third RFQ was increased to 1 cm to reduce the mass selectivity of this trap, better control the conditions in the trap, increase the efficiency and enable broadband operation.

Installation of a RFQ Based Switchyard

As shown in figure 3.7 the horizontal RFQ beamline and the vertical oriented parts of the MR-TOF-MS were originally [Dickel, 2010] connected through a curved resistive RFQ. A constant DC gradient along the RFQ guided ions around the corner. Calibrant ions from an internal thermal ion source were transported through a hole in one of the RFQ rods, which required a high amount of ions because of the low transmission efficiency through the rod caused by the high amplitude of the applied RF voltage. To overcome this limitation a switchyard based on a RFQ structure, developed in [Greiner, 2013, Plaß et al., 2015], was installed in 2014, see figure 3.7.
Figure 3.9 shows a picture and a technical drawing of the switchyard installed in the MR-TOF-MS. On top is an ion source combining a surface ionization source (Heat Wave labs TB-118) for Cs, Ba, Ca and Sr ions and an in-house made electron impact ion source, which generates ions from gasses like Xe or SF_6. A channeltron detector (Photonis 5901 Magnum Electron Multiplier) allows the measurement of high ion currents as well as single counts for commissioning of the RFQ beamline or high pressure operation of the CSC [Reiter, 2015]. On the third side a motor controlled valve can be used to decrease the pump down time of the RFQ system. One side is currently unused and allows the installation of additional ion sources or detectors for future applications.
Ions from CSC and internal ion sources can be mixed in the switchyard and transported together to the time-of-flight analyzer or ions from one direction can be split up to measure them in the MR-TOF-MS and on the channeltron [Plaß et al., 2015].
In the prototype of the switchyard [Greiner, 2013] the electrodes were cubes with metal electrodes on the corners for connecting and an electrical resistance of about 30 Ω. This low resistance and the consequential current heated up the electrodes, which results in outgassing. In the version in the MR-TOF-MS the electrodes are constructed as shown in figure 3.9, which increases the resistance and prevents the electrodes from heating up and outgassing.
The new switchyard provides calibrants in a wide mass range for calibration and the channeltron as diagnostics tool can measure higher ion currents from the CSC than the MR-TOF-MS.

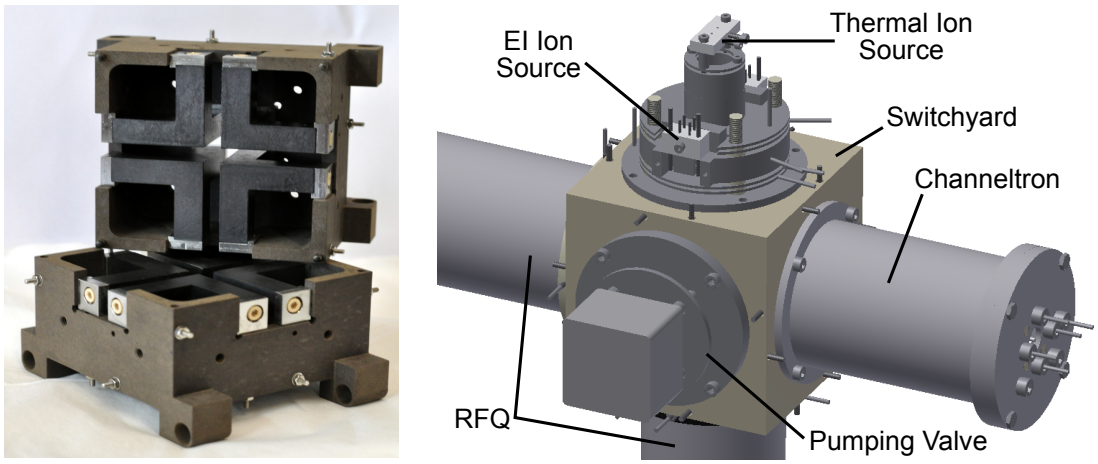

Figure 3.9.: Left panel: Picture of the opened switchyard [Jesch, 2016]. Right panel: Technical drawing of the RFQ switchyard in the MR-TOF-MS. The RFQs are installed at the bottom and the left-hand side of the switchyard. A channeltron detector is placed on the right-hand side and the ion sources on top of the switchyard. The large diameter of the pumping valve in the front decreases the pump-down time.

Improved Sinusoidal RF-Voltage Generation and Mixing

The sine RF voltage for the RFQs and the switchyard are generated by a resonance circuit consisting of a hand wired air coil and the capacitance of coax cables and the rods in the RFQs. Originally the resonance circuit was driven by a sine RF voltage from a frequency generator amplified by a modified commercial amplifier (RM Italy KL-500). The disadvantage of this solution was the large size of the required electronics located in the frame of the MR-TOF-MS, the reduction of the Q value caused by the amplifier and the limited capability for remote control of the used devices.
In the new version the resonance circuit is driven by a rectangular voltage [Ayet San Andres and Short, 2015], controlled by a TTL signal like all other pulsed voltages in the MR-TOF-MS. The size is roughly reduced by a factor of 4.
An analysis electronic enables the readout of the RF amplitudes of both phases and the amplitude and phase difference between them.
To apply a electrical drag field along the RFQs, the generated RF voltage must be coupled with several DC voltages. This is done inside the vacuum chamber on two PCB based mixing boards, to reduce the number of electrical feedthroughs and the capacitance of the resonance circuit. Figure 3.10 shows the corresponding circuit diagrams.
The coils on the mixing boards are made of ferrite rings wrapped with Teflon isolated cables. They have a high Q value and the cables have almost no electrical resistance. The main reason, why no commercial coils were used, is, that they typically have a resistance of several ten Ω or more.
The changes make the the RF-voltage generation and mixing much more reliable and robust and enable higher RF-voltages.

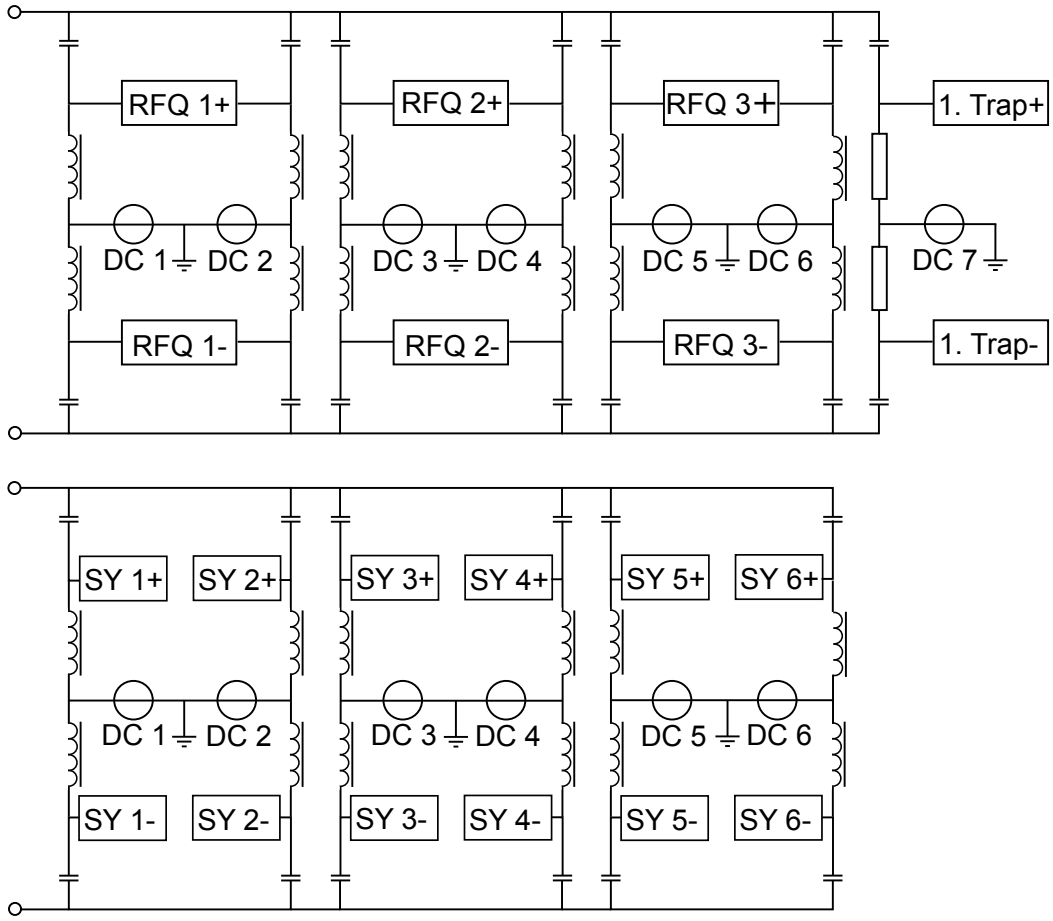

Figure 3.10.: Circuit diagram of the mixing boards inside the vacuum. The upper one is for the voltage supply of the RFQs and the first trap, the lower one for the switchyard. The DC potentials float the RFQs and the trap respectively the different surfaces of the switchyard and are mixed with the RF voltages, which are coupled on the left-hand side of the boards. All used capacitors have a capacitance of 22 nF, the resistors a resistance of 1 MΩ and the coils are handwrapped with an inductance of roughly 500 μH.

Steerer for Beam Alignment

If the different ion optical parts are mechanically not perfectly aligned, e.g. because of fabrication tolerances, the ion beam will not hit the detector. A misalignment like this can be compensated by using two sets of quadrupole steerer to change beam position and angle. In the MR-TOF-MS these are on the one hand the steerer electrodes directly after the trap system and on the other hand the electrodes of the mass range selector in the middle of the time-of-flight analyzer, compare figure 3.7.
The setting to align the beam consists of 8 different voltages, which are determined by scanning the corresponding parameter space. Till now this is done by hand, but will be done automatically by MAc in the future.

Stabilization of High Voltages

The fluctuations of an insufficient stabilized voltage in the mass analyzer influenced the time-of-flight of ions in the beamtime 2012, see also section 5.1.2. The hardware stabilization was reworked in 2013 to solve this issue. The new stabilization enables a higher mass resolving power and improved reliability of the system. For further details see reference [Ayet San Andres, 2017].

Increased Kinetic Energy

The kinetic energy of the ions was increased from 750 V to 1300 V by improving the electronics of the trap system and the mass analyzer. The time-of-flight t is related to the kinetic energy of the ions E_{kin} via

$$t \propto E_{kin}^{-1/2} \tag{3.1}$$

If the width of a time-of-flight peak is dominated by the turn-around time Δt_{ta} (which is counter proportional to E_{kin} [Wiley and McLaren, 1955]), the increase in kinetic energy also increases the mass resolving power (equation 2.10)

$$R_m = \frac{t}{2\Delta t_{ta}} \propto \frac{E_{kin}}{E_{kin}^{1/2}} = E_{kin}^{1/2} \tag{3.2}$$

This enables shorter measurements for a given mass resolving power. An increase of the kinetic energy results also in a reduction of the beam emittance. The results are shown in reference [Ayet San Andres, 2017].

Improved Differential Pumping

The high gas pressure in RFQs and trap system is required to transport and cool ions. However a higher pressure increases the loss of ions in the time-of-flight analyzer through collisions with residual gas. Therefore a differential pumping as good as possible is needed. It was improved by installing a larger turbomolecular pump on the top cross and reducing the conductance between trap system and upper cross by tightening the encapsulation of RFQs and trap system, but this has no influence on the directed gas flow from the trap system to the time-of-flight analyzer. Therefore a aperture with smaller diameter was installed after the last trap.
To reduce also the pressure in the lower cross an additional turbomolecular pump was installed there.
All together reduces the pump-down time of the system after venting and the probability of gas collisions of the ions, which increases the transport efficiency.

Remote Control

During an online measurement the MR-TOF-MS must be controlled remotely for radiation safety reasons. This includes both the adjusting of voltages and TTL signals and the readout of values like pressures, currents and the position of the detectors. Software and hardware has been developed and implemented to control and check the different parts of the MR-TOF-MS.

Connected Devices All electronic devices are controlled via serial connections. Either with USB or a serial-to-ethernet adapter.

Labview Controll Software Based on Labview a program was developed that controls all parts of the vacuum system like the turbomolecular pumps and regulating valves for gas inlet [Siebring, 2012]. Also included in the program is the control of frequency generators and automatically recording of the system properties.

Voltage Control DC voltages can be controlled in a software, which offers graphical arrangements and grouping of alls channels and formulas to calculate automatically voltage settings [Lotze, 2014].

Moveable Detector System A PCB based position sensor enables the position readout of the moveable detector system and positioning with an accuracy of better than 1 mm.

Temperature Sensors at different parts of the setup monitor the temperature of critical parts like electronics and warn in case of an overheating.

4. Development of the MR-TOF-MS Mass Analysis

The quest for the investigation of the most exotic nuclei requires effective measurements with a few ions only. Ideally information is extracted from a detection of a single ion. Mass measurements become a challenge by the existence of long-lived low lying isomeric states, which can only be barely resolved from the ground state.
A schematic time-of-flight spectrum, after application of our time-resolved calibration, see section 2.5, is shown in figure 4.1. It consists of separated and overlapping

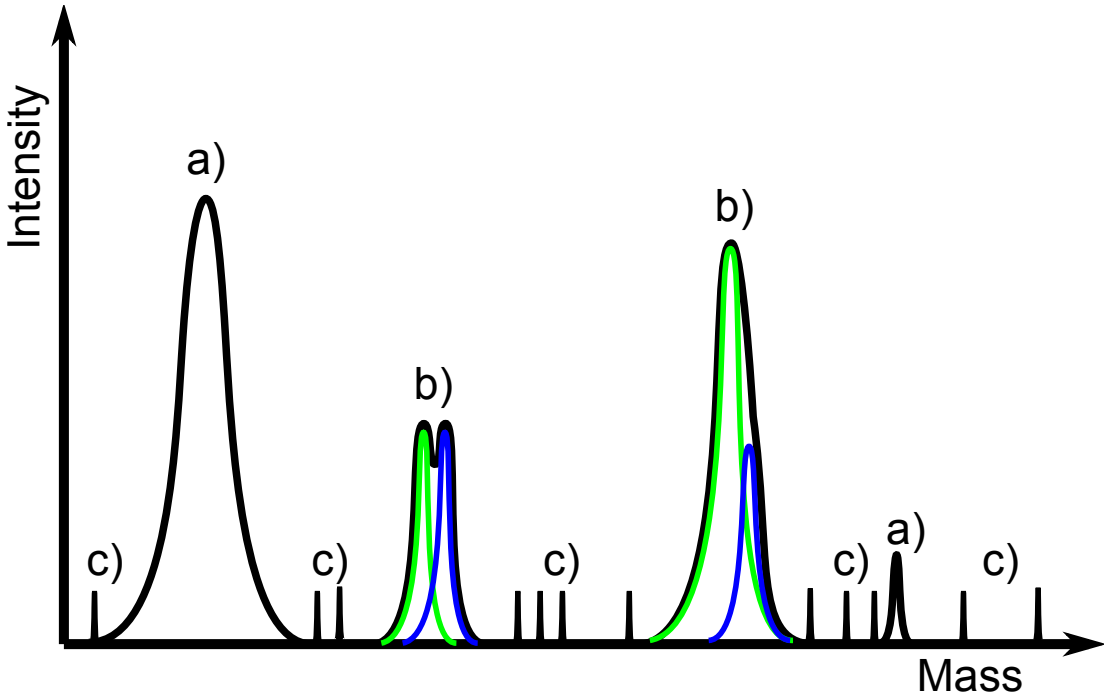

Figure 4.1.: Schematic mass spectrum demonstrating the characteristic experimental conditions. It consists of single peaks (a), overlapping peaks (b) and randomly distributed dark counts (c).

peaks and randomly distributed dark counts. Typically the background in the MR-TOF-MS ranges from background free to signal-to-noise ratios of 1:5 and the signals of an ion of interest have between 10 and 10,000 events.
To cope with these data a new fit procedure to determine the centre of the different mass distributions was developed and is explained in the following chapter. Standard methods for this task are summarized in appendix A.2.
Figure 4.2 shows examples for measured mass spectra. 4.2 a) and b) contain nearly

separated and overlapping peaks. Mean and median can not distinguish between the peaks and can therefore not be used. 4.2 c) shows a peak with a low statistics of only 11 counts. The choice of a bin size and position, as required for the Minimum χ^2 Estimation, has a strong influence on the fit result. Also the significance of the results would be low [Taylor, 1982]. As a rule of thumb a minimum of 20-30 events is required to determine the centre of a distribution with the Minimum χ^2 Estimation. The only method that works for all of this cases and is robust is the weighted maximum likelihood estimation (WMLE) [Hu and Zidek, 2002]. Additionally the WMLE can also work with unbinned data (for a definition of un-/binned data see A.1). Unbinned data are typically the data format of choice for the MR-TOF-MS, since the binning to a histogram limits the accuracy for the mass determination with a few ions. The WMLE is a well established method. The function that is optimized by the WMLE describes the distribution of the measured mass spectra. The shape of peaks measured in the MR-TOF-MS does not follow a known analytical function, but can be described by the Exponentially Modified Gaussian (EMG) [Bortels and Collaers, 1987] function. The EMG is a combination of a Gaussian and exponential functions. The probability density function of an EMG with k exponentials on the left side and N-k on the right side of the Gaussian function can be written as (compare appendix A.5) [Purushothaman et al., 2016]

$$\mathrm{EMG}(x, \mu, \sigma, \tilde{\eta}, \tilde{\tau}) = \frac{1}{4}\sum_{i=1}^{N}\frac{\eta_i}{\tau_i}\left(\exp\left(\frac{1}{2}\left(\frac{\sigma}{\tau_i}\right)^2 + \xi_i\frac{x-\mu}{\tau_i}\right)\mathrm{erfc}\left(\frac{1}{\sqrt{2}}\left(\frac{\sigma}{\tau_i} + \xi_i\frac{x-\mu}{\sigma}\right)\right)\right) \quad (4.1)$$

$$\text{with } \sum_{i=1}^{k}\eta_i = \sum_{i=k+1}^{N}\eta_i = 1 \quad (4.2)$$

$$\text{and } \xi_{1,..,k} = +1 \wedge \xi_{k+1,..,N} = -1 \quad (4.3)$$

μ and σ^2 are the mean and variance of the Gaussian function. $\vec{\eta}$ and $\vec{\tau}$ include the weighting parameters and coefficients for the exponential functions. Normalization is given by equation 4.2.
The use of the WMLE and the EMG for peak fitting requires that the following points are considered.

- The errors for the EMG can not be analytically calculated. Therefore, they are numerically treated.

- Errors and behaviour of fit processes for overlapping peaks do not follow general rules and are investigated in this work.

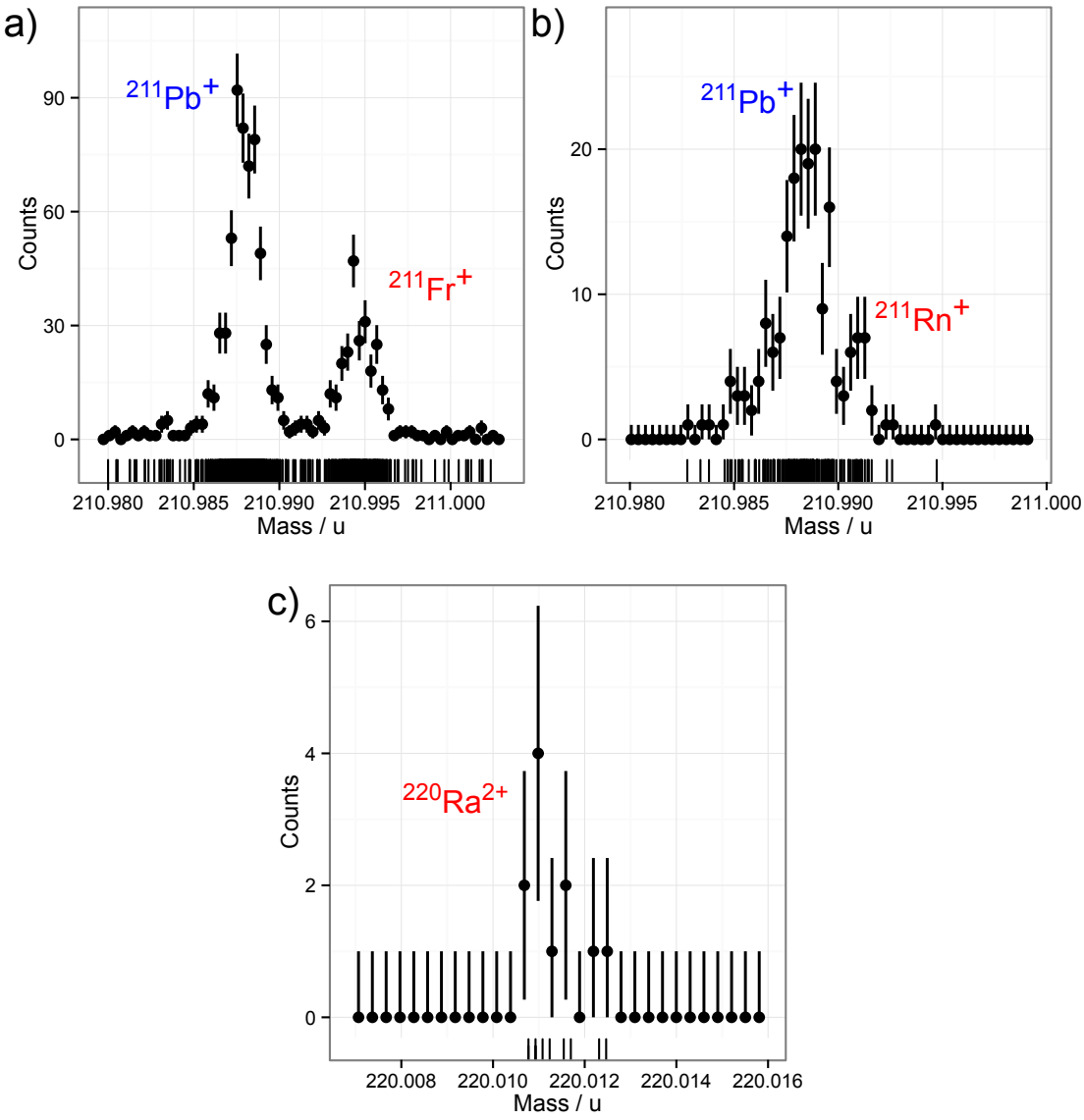

Figure 4.2.: Characteristics of measured mass spectra. Panel a) depicts two well separated mass distributions (peaks), panel b) two overlapping peaks and panel c) a peak with very low count rate.
The histograms of the data are shown to guide the eye. The "rug graph" under the histograms shows the original, unbinned data which are analysed.

4.1. Development of the Fit Algorithm

4.1.1. Test Procedure

The fit algorithm is written in the statistical language R [R Core Team, 2015]. The single steps of the fit algorithm were tested and investigated by repeatedly fitting of simulated and bootstrapped data from measured spectra (see also appendix A.1). A typical number of repetitions for one test was $N_{Sim} = 1000$. The simulated spectra cover a wide parameter space, which corresponds to the expected experimental conditions for the fit algorithm:

Peak Shape The parameter for the peak shapes have in principle an large parameter space. However for understanding of the general behaviour and characteristics of the fit algorithm we have chosen the peak shape from a ^{211}Pb spectrum with mass resolving power 125,000 measured in the beamtime in 2012. This peak with high statistics was fitted with the software Igor with a Gauss and EMG function, compare table 4.1 and figure 4.3. The Gauss function was used to have a comparison between the EMG with tails and a function with no tails, so that the fit procedure can be used universally.
The parameters for Gauss and EMG were fixed in all investigations. What was changed and fitted were the peak centres and areas.

Counts per Peak The number of counts in a single peak was 2^n, $n = 3..10$.

Peak Ratios For the case of overlapping peaks their area ratios were between 1:1 and 1:16.

Peak Centres and Distances The peak centres, that were put in the generation of simulated spectra, are called the true values x_{true}. The distance between overlapping peaks was varied from zero to 2 FWHM. In a distance of 2 FWHM the peaks are quasi separated for the fit algorithm.

Outlier A single outlier was placed in a distance between zero and 10 FWHM to investigate the stability of the fit with regard to a single random background event.

Signal-to-Noise Random signals were added to simulate e. g. detector dark counts in real measurements. Therefore in a range of $\pm$10 FWHM around the peaks, noise was generated with a signal-to-noise from 1:0 up to 1:5. The ratio 1:5 was chosen based on the test presented in section 4.2. At this ratio the significance of peaks being not just generated by constant background but being a real event is in average 3σ, which corresponds to a probability of 0.9973 that the data include not only random noise, but also one or more peaks.

Initialization For initialization of the fits user input is needed for the peak centres and areal ratios. This was simulated by initializing these values randomly around

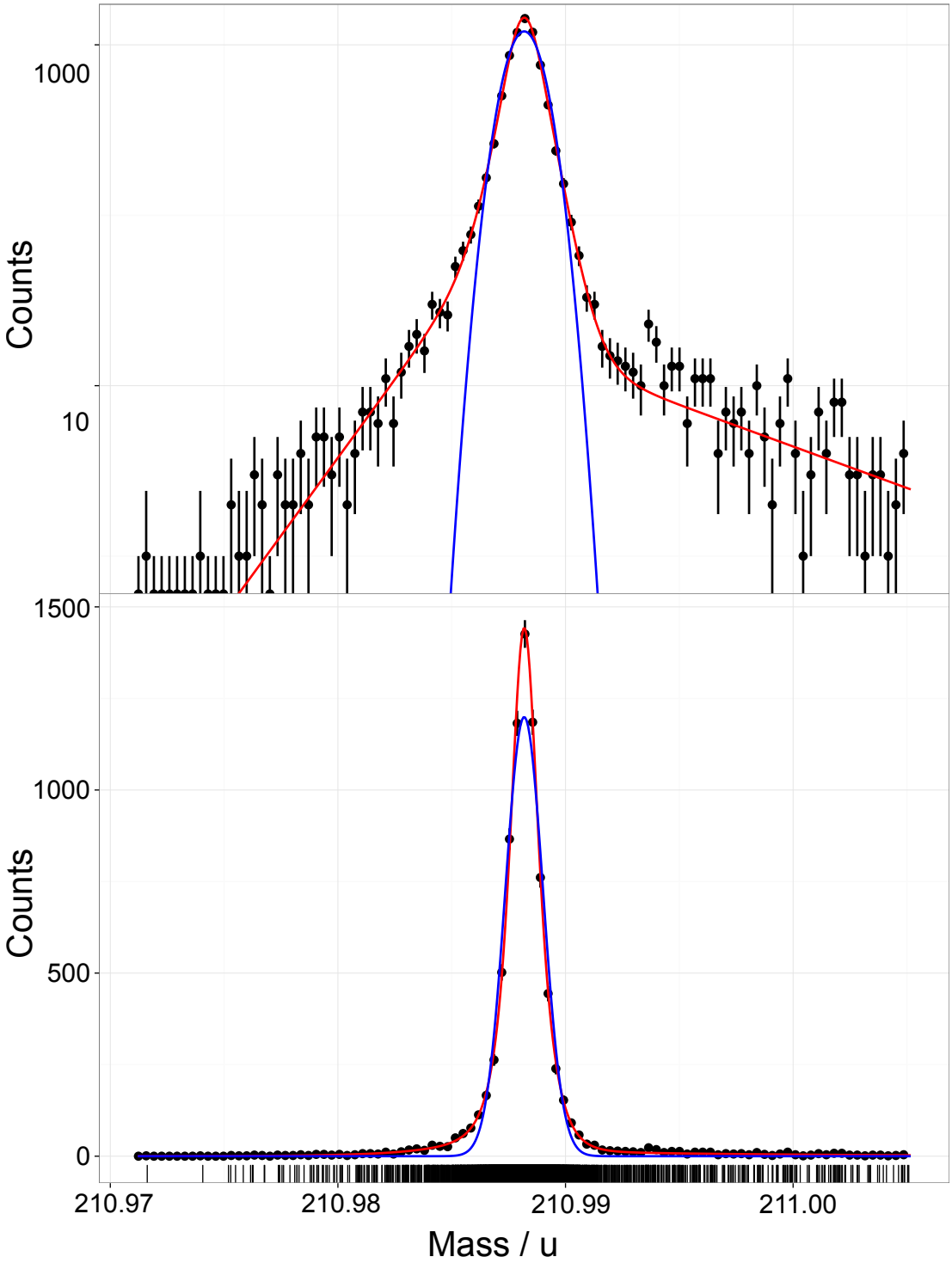

Figure 4.3.: Measured mass spectrum of ^{211}Pb ions shown in logarithmic (top panel) and linear (bottom panel) scales. This mass distribution was used for the determination of the fit parameters for the EMG function (red lines) [Jesch, 2016]. For comparison, a fit with a Gauss function is also shown (blue lines). The FWHM of the distribution is $1.698 \cdot 10^{-3}$ u corresponding to 1.6 MeV. The number of recorded events is about 9000.

the true value x_{true}. It was assumed that a user can do this by "eye" with an accuracy of $\pm$ 0.2 FWHM.

	Parameter	Value
Gauss	σ	$7.226 \cdot 10^{-4}$
EMG	σ	$3.539 \cdot 10^{-4}$
	$\vec{\eta}$	$(0.8028, 0.1972, 0.8958, 0.1042)$
	$\vec{\tau}$	$(5.323 \cdot 10^{-4}, 2.374 \cdot 10^{-3}, 5.848 \cdot 10^{-4}, 8.914 \cdot 10^{-3})$

Table 4.1.: Peak parameter fitted for Gaussian and EMG (with two exponentials on each side) functions from the measured data shown in figure 4.3 used for the development of the fit algorithm. The FWHM of the peak is $1.698 \cdot 10^{-3}$ u.

In the following results will be shown for normal distributed data fitted with Gauss functions and EMG distributed data fitted with EMG functions. The distribution of the data and the fitting functions are not mixed up.
The averaged results of mass fits x_{Fit} are normally shown as deviation from the true value x_{true} in units of the FWHM to make them independent of the actual simulated mass resolving power.

$$\text{deviation} = \frac{x_{Fit} - x_{true}}{\text{FWHM}} \tag{4.4}$$

An averaged deviation of 0.01 FWHM of the fit means for example an accuracy of 8 $\cdot 10^{-8}$ for ^{211}Pb like it was measured in the beamtime 2012, compare section 5.1.

4.1.2. Generation of Random Numbers

For generation of normal distributed random numbers the built-in R function *rnorm()* was used. The generation of random numbers based on the EMG is more complex, since the product exp(x)erfc(x) can be $0 \cdot \infty$, which causes numerical problems during computation. Therefore a random number generation based on discrete and not continuous values of the EMG function was used. To avoid problems due to the binning of the random numbers the bin width was chosen to be about 2000 times smaller than the full width half maximum (FWHM) of the simulated peaks. The used function is *DiscreteDistribution()* from the library *distr*.
Constant background was generated with the function *runif()*.

4.1.3. Fit Process

The fit process for a single peak and two overlapping ones is partially different. Figure 4.4 shows the procedures. For single peaks the data are fitted with a WMLE in

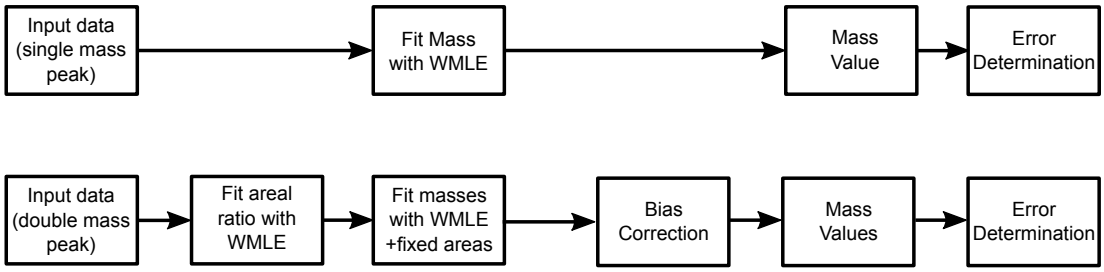

Figure 4.4.: Upper part: The present procedure of fitting a mass spectra with a single separated peak. The lower part shows the corresponding procedure for fitting two or more overlapping peaks. The first step is the determination of the ratios of the peak areas. This first fit result yields numerical stability. The centres of the peaks are fitted in the second step with high accuracy and fixed areas.

an iterative process, which removes dependence on initialization of the fit (compare sections 4.1.4 and 4.1.5). The very precise numerical minimizer *nlm()* based on [Dennis Jr and Schnabel, 1996] is used for this. The result of the fit is the final value for the peak centre. Subsequently the parameter and statistical errors are calculated (section 4.1.9).
For the case of double peaks the fit process is divided into several parts. The first is the determination of the areal ratios of the peaks. This is done with the minimizer *constrOptim()* [Lange, 2010], which is not as precise as the *nlm()*, but has the advantage of higher numerical robustness in case of background and the possibility to use linear constraints for the fitted parameters.
At the end of the fit process the peak areas are calculated from the areal ratio and the number of peaks in the spectrum. The Area A_i of peak i is

$$A_i = a_i \cdot \left(N_{counts} - \frac{n_{bg}}{\Delta_{sp}} \right) \tag{4.5}$$

a_i is the corresponding areal ratio, N_{counts} the number of counts in the fitted spectrum, n_{bg} the number of background counts in a peak-free area of the spectrum and Δ_{sp} the size of the fitted spectrum. n_{bg} is part of the user input and not determined by the fit process.
The obtained areal ratios are an fixed input for the fit of the peak centres, which is done like in the case of a single peak with the minimizer *nlm()*. In case of close lying double peaks the fit results are shifted compared to the true values (typically the two peaks are shifted towards each other). This is corrected with the Bias correction, see section 4.1.7, before the parameter and statistical errors are calculated.

4.1.4. Weighted Fits

In equation A.16 it was shown theoretically that a fit of normal distributed data is very sensitive for outliers. Figure 4.5 illustrates this nicely. There the distance between peak and outlier is proportional to the deviation of the fit results from the true value.

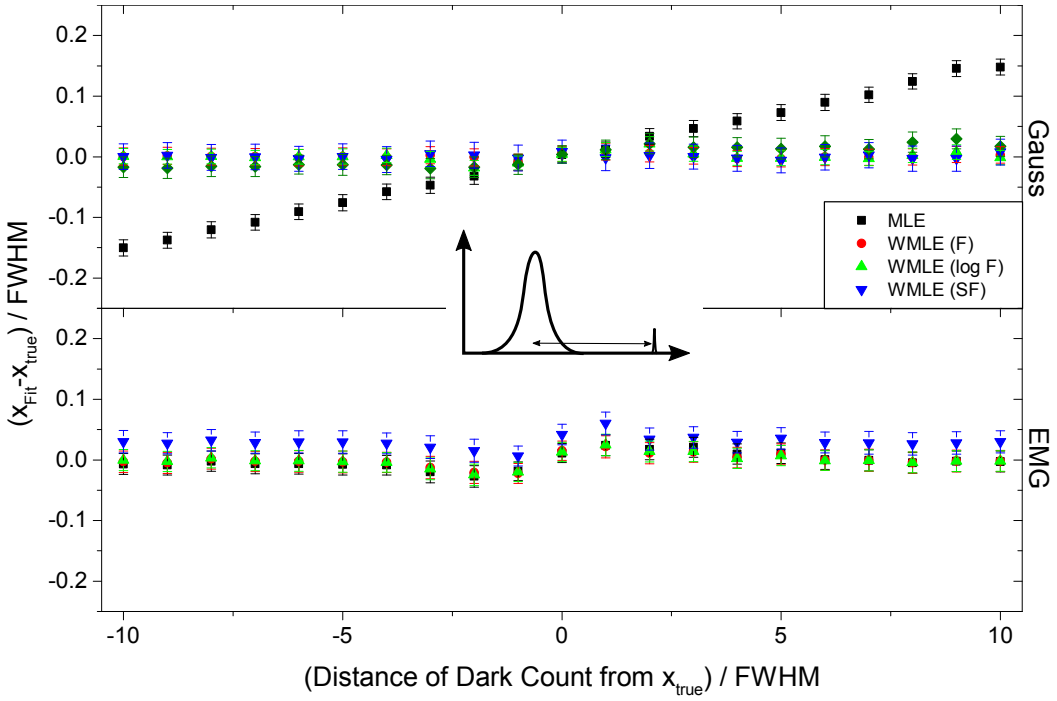

Figure 4.5.: Calculated characteristics of the MLE and WMLE fit procedures for normal (top panel) and EMG (bottom panel) distributed, simulated spectra with 32 counts and one additional dark count placed at different distances from the "peak centre" of the simulated distributions. The task is illustrated in the schematic spectrum in the middle of the figure. Each data point represents the average of 1000 simulated spectra and fits with the corresponding peak functions. Shown are the deviations of the averaged fit results x_{Fit} from the true values x_{true} of the peak centres defined by μ in equations A.18 and A.23. The simulations have been made for the unweighted (MLE) and weighted (WMLE) log-likelihood function $\mathcal{L}$. The weights are its distribution function (WMLE(F)), the natural logarithm of the distribution function (WMLE(log F)) and a step function with the value 1 for all counts within a distance of one FWHM from the peak centres (WMLE(SF)).

In contrast to that fits with a weighting are very stable and independent for outliers.

Figure 4.5 also shows the behaviour of a fit with the EMG function. The EMG is much more robust to outliers. The reason for the higher robustness are most probably the tails of the EMG. The difference between the two functions is that the EMG has tails which give outliers a higher probability in contrast to the Gauss function which has practically no tails, compare figure 4.3.

Three different kinds of weighting functions were tested to find the best one:

WMLE(SF)-Step Function All counts within a certain distance around a peak were weighted with 1, everything else with zero. The distance needs to be adjusted by hand, which depends on the actual peak shape properties like asymmetries. For double peaks non linear behaviour is possible when peak distance and weighting window are similar.

WMLE(F)-Distribution Function If the distribution function itself is used, the properties of the peak shape are taken into account. This is a very strong weighting, since events at a distance of 1 FWHM are already suppressed by a factor 2.

WMLE(log F)-Natural Logarithm of the Distribution Function This one is similar to the weighting with the distribution function, it also takes the peak shape into account. Taking the logarithm of this function changes the speed at which the weighting factor goes down to zero. The weighting factor τ_i is defined as

$$\tau_\mathrm{i} = \begin{cases} \log(\mathrm{f}) & \text{for } \log(\mathrm{f}) \geq 0 \\ 0 & \text{else} \end{cases} \tag{4.6}$$

The reason for this is that τ_i must be between zero and a positive value.

The mean of the weighting functions is fixed during the fitting. Its value is the initialization of the fit or result of the previous iteration step.
Figure 4.5 shows that for fitting single peaks all three weighting methods give similar results. The widths of the weighting functions were varied (σ for the Gauss function, σ and $\vec{\tau}$ for EMG) which changes how fast weighting goes down to zero. Within a factor of 2 no changes in the averaged results were observed for all three weighting functions. Figure 4.9 illustrates the influence of a small signal-to-noise ratio on the fit of a single peak on the example of WMLE(log F).
This is different for the case of two overlapping peaks. The optimizer *constrOptim()* for the determination of areal ratios of the peaks was only numerical stable if the step function was used, figure 4.6 shows an example. The results for Gauss and EMG are comparable. The increasing deviation from the true areas for increasing background is caused by the fact, that the signal-to-noise ratio of the smaller peak is very small (almost 1:8 for 100 background events, which is not significant). For all cases with significant peaks, compare section 4.2, the fit works very well.

Also the fit of peak centres behaves differently. If the weighting functions are to small to take also the tails into account, the peak centres differ from the true values, compare WMLE(F) in the lower right part of figure 4.7. If the weighting functions are to broad the fit is stronger affected by outliers. For example different widths of the step functions for the mass fit were tested and the same stable results were found for widths from ± 1 to ± 1.5 FWHM.
A test where the FWHM of all weighting functions was the same showed that in this case the results for all weighting functions are identically and most important for the goodness of a weighting function is not the shape of the function but the width of the function. The importance of the width of the weighting function is also the stronger the more the areal ratio differs from 1, compare figure 4.7. There the different weighting functions behave differently, depending on their different widths.

All three functions in common is also that the fitted values have a bias from the true value. The difference is the size of this bias, which shows that the weighting functions WMLE(log F) and WMLE(SF) are preferable to WMLE(F). For different peak intensities the WMLE(F) has also problems to determine the position of the smaller peak even without background, compare the lower right part of figure 4.7.
A disadvantage, that only concerns WMLE(SF), is the jumping behaviour between

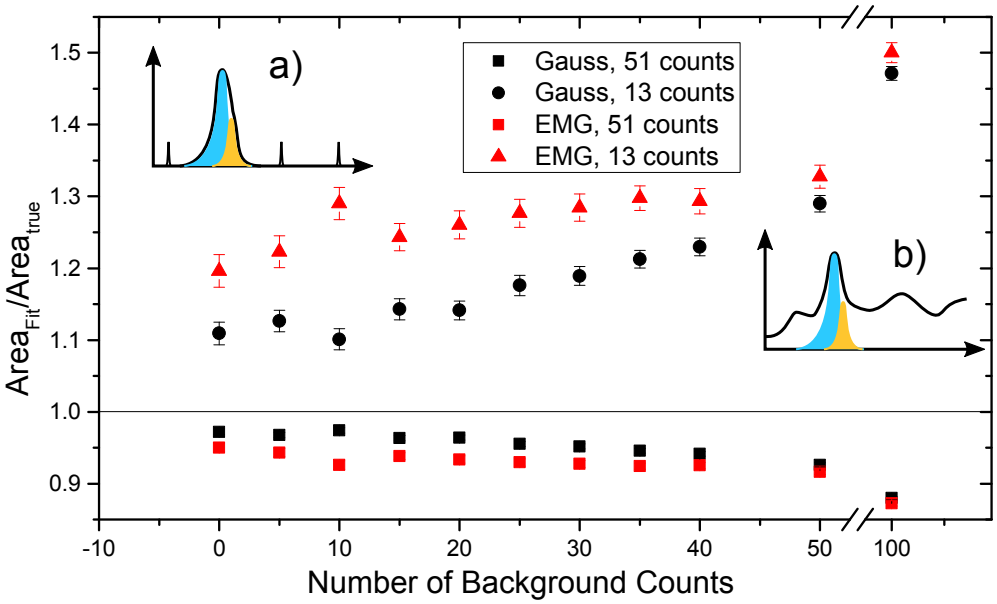

Figure 4.6.: Fit of the areas of two overlapping distributions with 51 (left peak) and 13 (right peak) counts.The peak centres have a distance of one FWHM and an additional background is superimposed. Each data point represents the average of $N_{Sim} = 1000$ simulations. The absolute number of counts in the peaks was calculated from the areal ratio with equation 4.5. The schematic mass spectra illustrating the case of almost no background (a) and 100 background counts (b) are shown. Fitting of the area of the small peak with 100 background counts is still possible with an error of 50 %.

the fits of two peaks, where the width of the weighting functions is similar to the peak distance.

As a conclusion the for the area fits the weighting function WMLE(SF) was chosen, which gives good fit results even for signal-to-noise ratios, which are lower than what is expected for measurements with the MR-TOF-MS. For mass fits the weighting function WMLE(log F) is the only one that takes the peak shape into account and works with strongly different peak intensities.

4.1.5. Iterative Fitting

In case the initialization of the WMLE has an offset to the true value, which is normally the case, the weighting with a wrong peak centre results in a wrong fit value. Figure 4.8 illustrates this problem for an overlapping peak with and without background.

This problem is more pronounced in the case of overlapping peaks with strongly different peak intensities or for peaks with low signal-to-noise ratio, where a small changes in the data weighting can have a big influence.

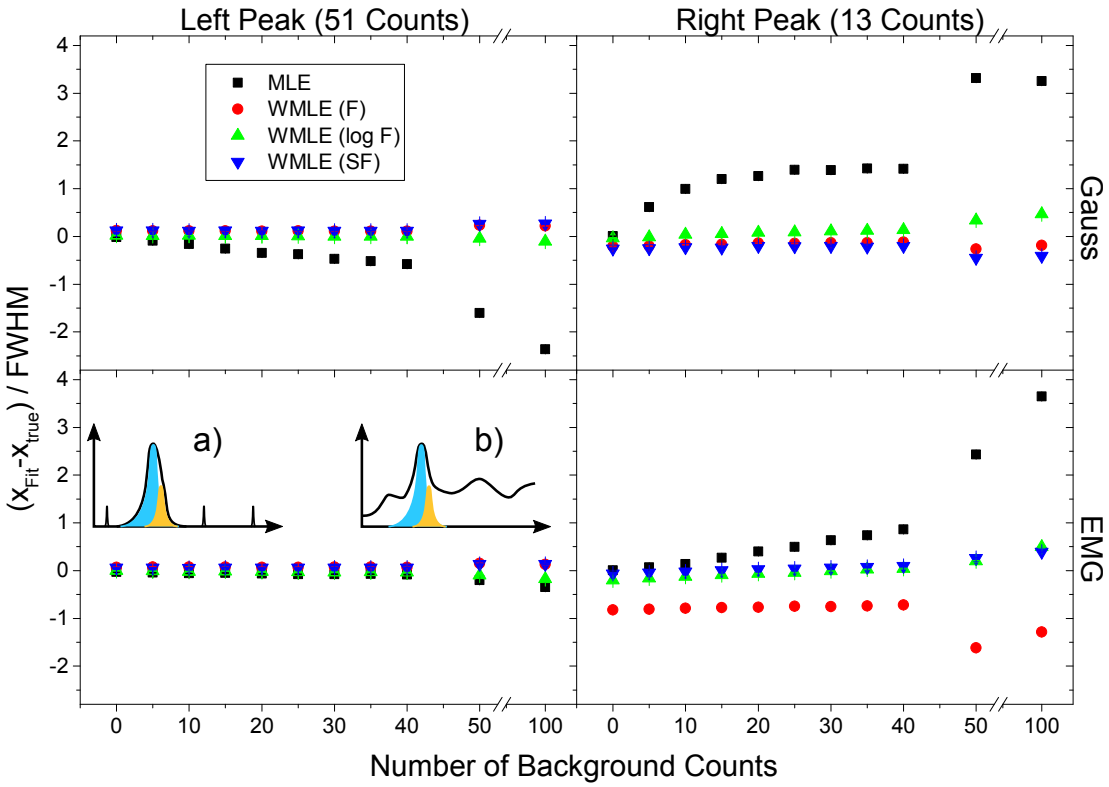

Figure 4.7.: Influence of different weights on the mass determination of two overlapping peaks with 51 and 13 counts. The peak centres have a distance of one FWHM and additional background is superimposed. Each data point represents the average of $N_{Sim} = 1000$ simulations. The sample standard deviations of the fits are smaller than the used symbols.
The schematic mass spectra illustrate the cases of almost no background (panel a) and 100 background counts, where the smaller peak is no longer visible (panel b). The large deviations for high background result from the deviations of the fit of the areas.

A solution is iterative fitting of the data, in which the fit result of the previous step is used as initialization for the next step and especially of the weighting function. Figure 4.8 shows the difference in the results between fitting only once or doing 4 iterations. This solution was implemented in our fit process. The convergence criterion is reached if the difference of the fit results from the last two iterations is below 0.002 FWHM, which is in our case a negligible small value. For example for the measurement of ^{211}Pb with a high statistics of almost 9000 counts and small statistical error, this value is almost a factor 3 smaller than the statistical error. For normal as for EMG distributed data the difference reaches zero after typically 2-3 steps for single peaks or 5-8 for overlapping peaks.

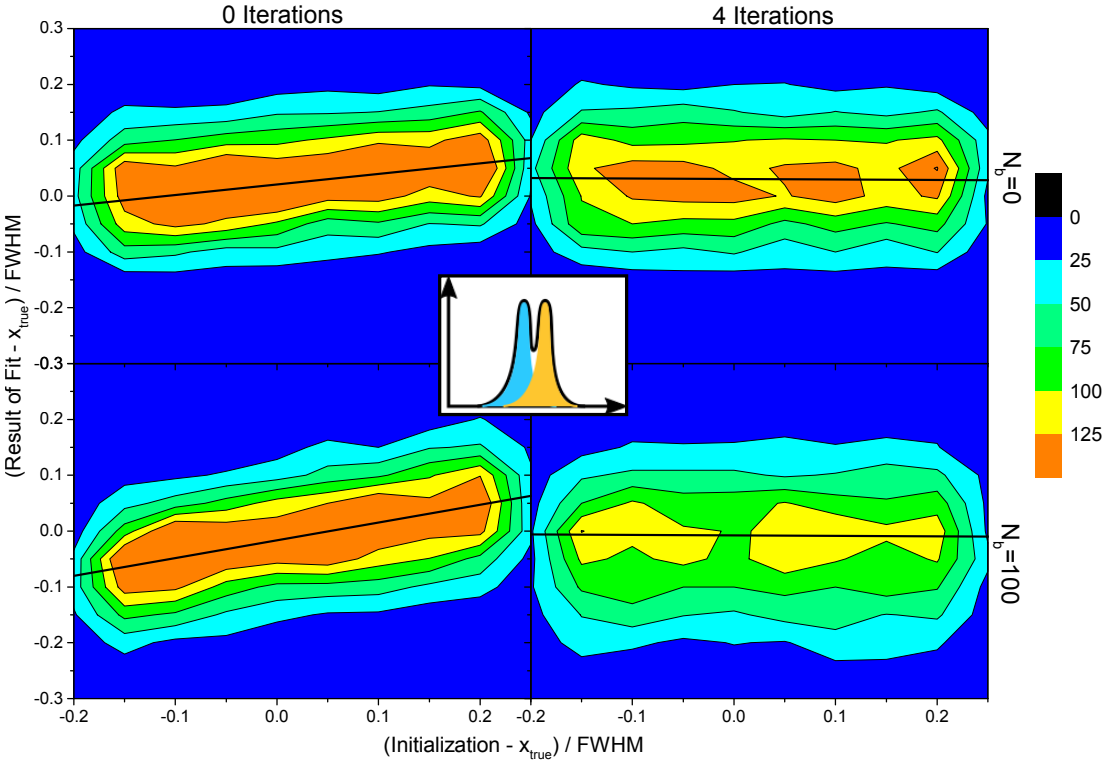

Figure 4.8.: Dependency of the fitted values for the peak centres of two overlapping peaks on the initialization of the fit parameters. Shown are the results for one EMG distributed peak only, the left one in the schematic spectrum. The results for the other peak are simply mirror symmetric. Each distribution has 32 counts. The distance of the peaks is 2 FWHMs and additional background $N_b = 100$ is superimposed in the lower panels. The results of the left panels are based on no iteration, the right panels include four iterations. For each graph 5000 simulations were done. The colours indicate the number of fits for a given initialization and corresponding result. The global dependency on the initialization is indicated by the slope of the black lines.

4.1.6. Influence of the Peak Width

The concept of this fit process is based on the assumption that the real peak shape is known. So the question is: How good must the real peak shape be known to get good results?
To investigate this, the parameters of the fitting functions were changed, but not the ones for generating the simulated spectra, and the typical simulation process was repeated, testing the parameter space mentioned in section 4.1.1.
Single peaks are nearly not effected (deviation < 0.01 FWHM) by changes of the width of the fit function of up to 20 %, compare figure 4.9. For ^{211}Pb this corresponds to an effect on the accuracy on the 0.08 ppm level, which is negligible. This behaviour is easy to explain at the example of the Gauss function. The MLE of the Gauss function acts like a mean of the fitted data, as shown in equation A.16, which does not depend on the width of the fit function. An effect is only possible if the background is not

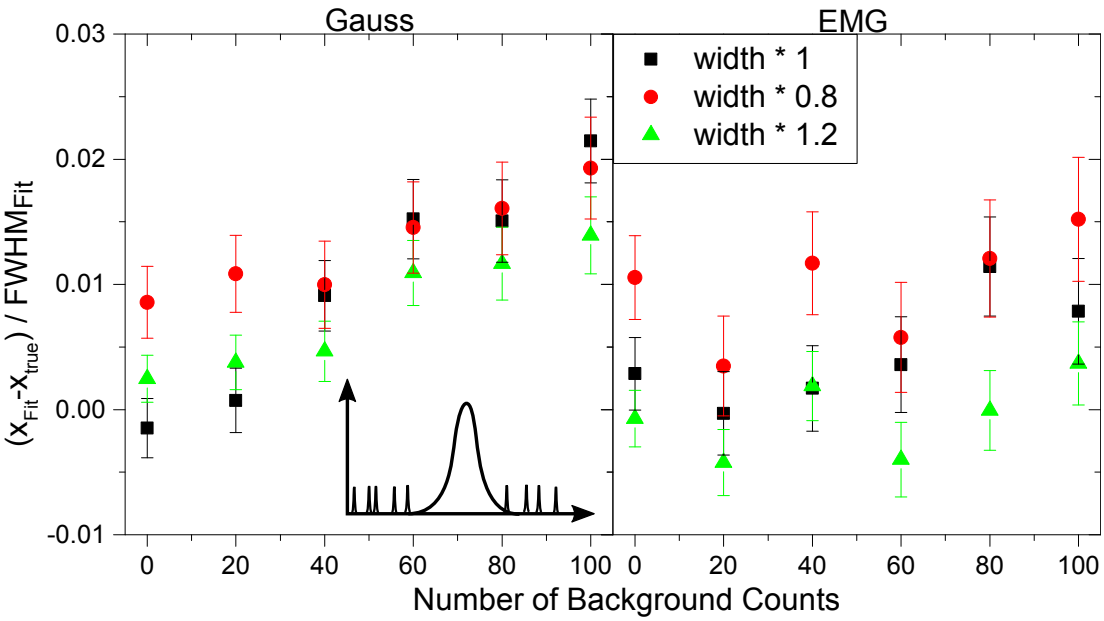

Figure 4.9.: Influence of a wrong width of the fit function for normal (left panel) and EMG (right panel) distributed data. Each data point represents the average from 1000 simulated spectra with 32 counts per peak and a varying amount of background. The assumed width of the fit function was varied by 20 % relative to the real width of the distributions.

symmetric on both sides of the peak. In this case the width of the weighting function has an influence on the result, but normally the background signals in the MR-TOF-MS are uniformly distributed over the complete spectrum.
Again the case is different for overlapping peaks. Figure 4.10 illustrates the effect of a wrong width for the determination of the distance between two overlapping peaks for the example of two normal distributed peaks. For the case with two overlapping

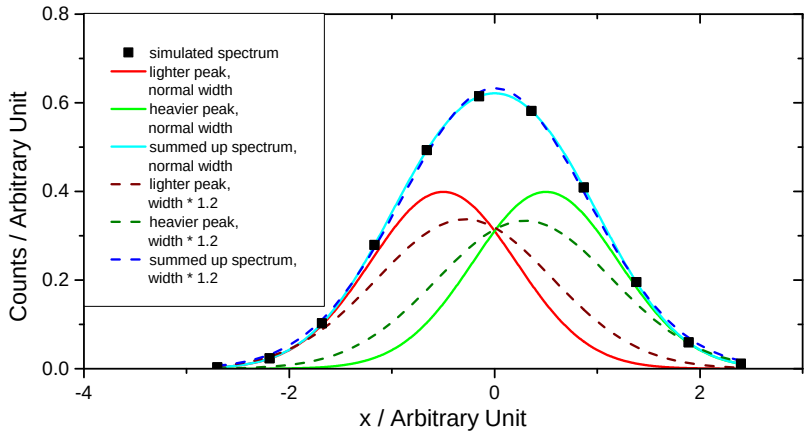

Figure 4.10.: Simulated spectrum of two overlapping Gauss peaks with a distance of 1σ fitted with correct (continuous lines) and by 20 % increased (dashed lines) peak widths. Although the widths are different the corresponding sum spectra describe both the data points.

peaks the data can either be described by two narrow peaks or two broader peaks in

a shorter distance.
Figure 4.11 shows a simulation for the case of two peaks with 32 counts per peak for different peak distances and distributions.

Already for a width which is off by 10 % an effect is visible (deviation $<$ 0.05

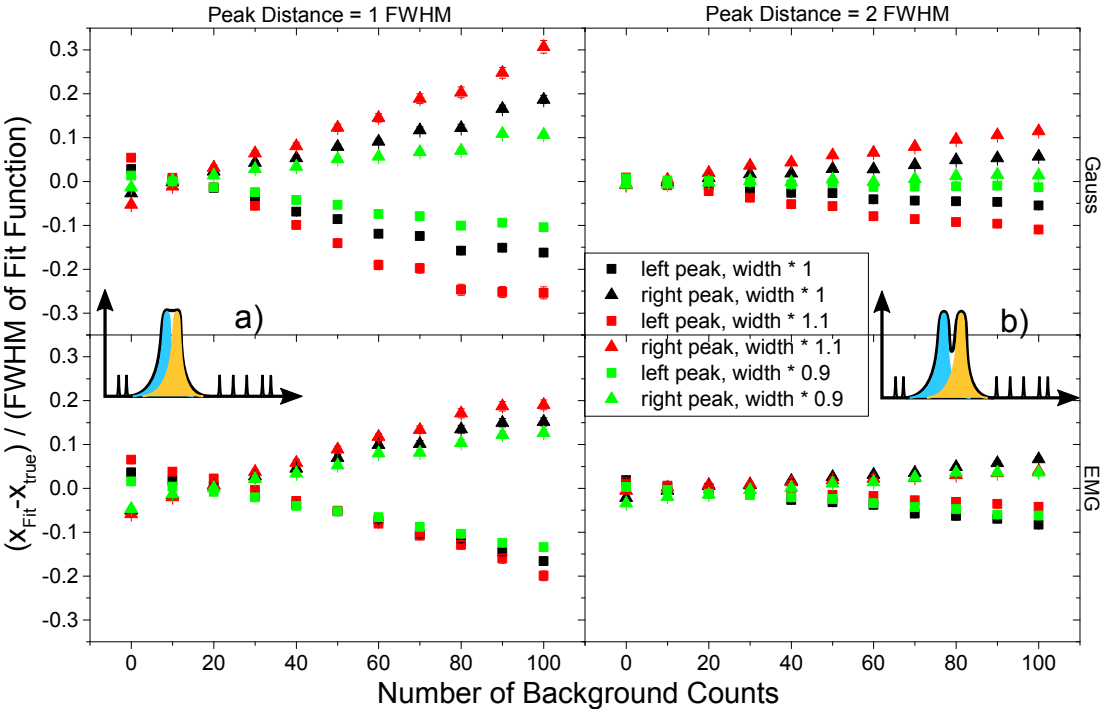

Figure 4.11.: Influence of a wrong peak width of the fit function for normal (top panels) and EMG (bottom panels) distributed data. The plots show the situation for two peaks with a distance of 1 FWHM (left panels and schematic in panel a) and 2 FWHM (right panels and schematic in panal b) and with 32 counts each. For each data point 1000 simulated spectra were fitted. The width of the fit function was variied by 10 % relative to the true widths of the distributions. The sample standard deviations of the differences between fitted and true values is smaller than the used symbols.

FWHM), whose size depends on the peak distance, ratio, total number of counts and the kind of distribution. The WMLE for EMG distributed data is here also more stable than the one for normal distributed data.
Summarized the real peak parameters must be known for overlapping peaks and strongly different peak intensities with an accuracy of 10 % or better to achieve an accuracy of 0.05 FWHM. The required minimum number of ions to determine the peak parameters with the requested accuracy can be estimated for normal distribution with equation A.3 and is about 50. This number is higher for the EMG, but 100 should be sufficient. For single peaks an accuracy of 20 % is sufficient to achieve an accuracy of 0.01FWHM, which corresponds to a relative accuracy of 0.08 ppm for ^{211}Pb.

4.1.7. Bias Correction for Overlapping Peaks

Fitting of overlapping peaks with the WMLE creates an bias in the mass values, whose size increases with smaller peak distances, larger background and the more the peak ratios are away from 1:1, compare for example figure 4.11.
The two peaks have two degrees of freedom that must be corrected for the bias, either the two peak centres or one peak centre and the peak distance. For the latter it is done in the following. Figure 4.12 explains how the peak distance is corrected.

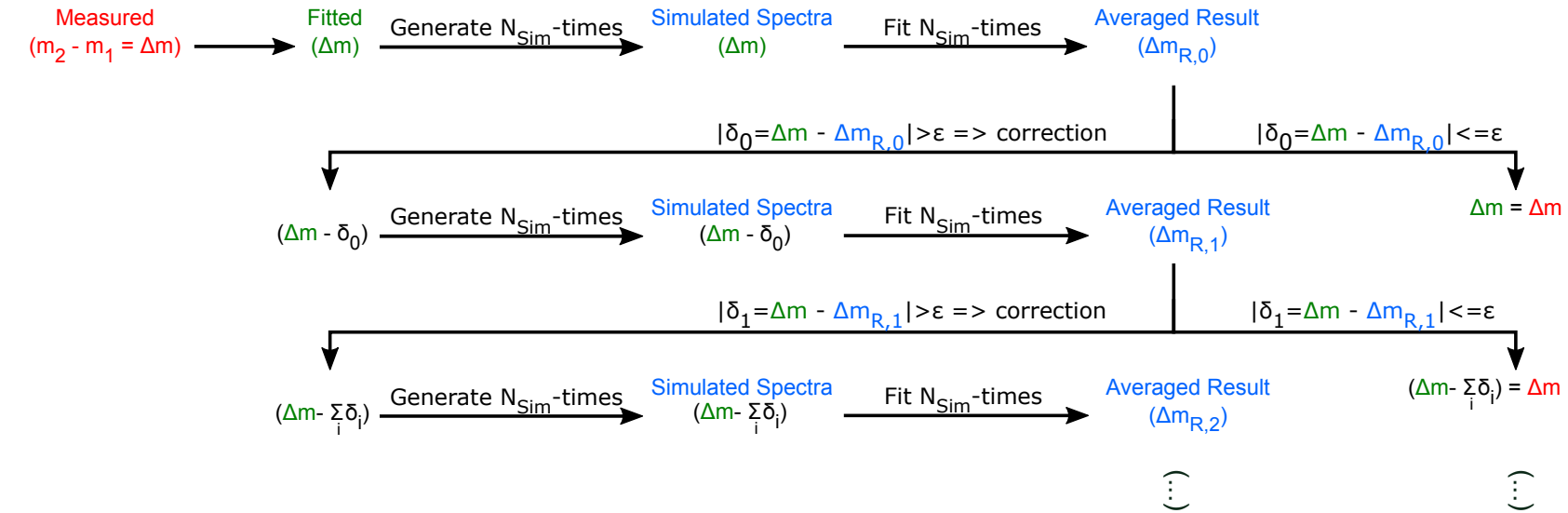

Figure 4.12.: Procedure of the bias correction for the measured peak distance. The fitted peak distance (Δm) of the measured data with the unknown real distance (Δm) has a bias caused by the fit process. Based on the fitted value (Δm) a simulation is started, which generates and fits N_{Sim} simulated spectra. The averaged result ($\Delta m_{R,0}$) is compared with Δm. If the difference δ is smaller than the convergence limit ϵ, then no further correction is needed and the peak distance is Δm=Δm.
Otherwise if $\delta_i > \epsilon$ a correction is mandatory and the new peak distance for the simulated spectra is the last one minus δ_i. The steps of fitting and comparing are repeated.
This process is iterated until $\delta_i <= \epsilon$ is reached. In this case the corrected peak distance agrees with the last input distance.

To determine the bias between the real and fitted peak distance a simulation is done, which generates N_{Sim}-times simulated spectra based on the fitted values and compares the averaged results for the peak distance with the initial value. The difference is subtracted from the fitted value and the new distance is used to start the next simulation. This is done until the difference δ of simulation result and the originally fitted value is less than a chosen convergence limit ϵ. The initial distance of the last simulation step is than the corrected peak distance.
After the peak distance is corrected, there are two possible cases:

- The mass of one of the peaks is known as in section 5.1. The mass of the second peak is then the mass of the first peak plus the corrected peak distance.

- Both masses are unknown. In this case the data must be fitted once again with two peaks, but with fixed areal ratio and peak distance.

Nevertheless the corrected values can still differ from the real value, thus no systematic investigation with real spectra has been done so far. Therefore an additional error contribution is added to the peak centres, see section 4.1.9.
This bias correction is very time-consuming, because of the number of spectra generated in each simulation, which depends on the peak distance, areal ratios and the convergence limit. The time needed to fit a single spectrum is roughly proportional to the number of counts in the spectrum. Typical values are about $N_{Sim} = 1000$ spectra per simulation for a convergence limit of 0.002 FWHM.

4.1.8. Comparison with Bootstrapping

To test the fit also for measured spectra, bootstrapped spectra were generated from the data set in figure 4.3 by randomly drawing N_{Counts} events with replacement for each spectrum. These spectra were fitted repeatedly with an EMG and the averaged results are shown in the upper part of figure 4.13. In the lower part the standard deviations of the fitted masses are shown and compared with the expected one for a normal distribution $\frac{\sigma}{\sqrt{N_{Counts}}}$. A fit of the standard deviations with the formula $f(x) = \frac{A}{\sqrt{N_{Counts}}}$ showed an increase of 23 % compared to the case of a normal distribution. This is caused by the broader distribution and the tails of the EMG and the weighting of events.
The test with bootstrapped data showed that the fit procedure works also with real data and it can reliable be used also for spectra with only 2 counts. The standard deviation of the fit results behaves like the one for the normal distribution and has only a slight increase because of the broader distribution of the EMG and the weighting of the WMLE.

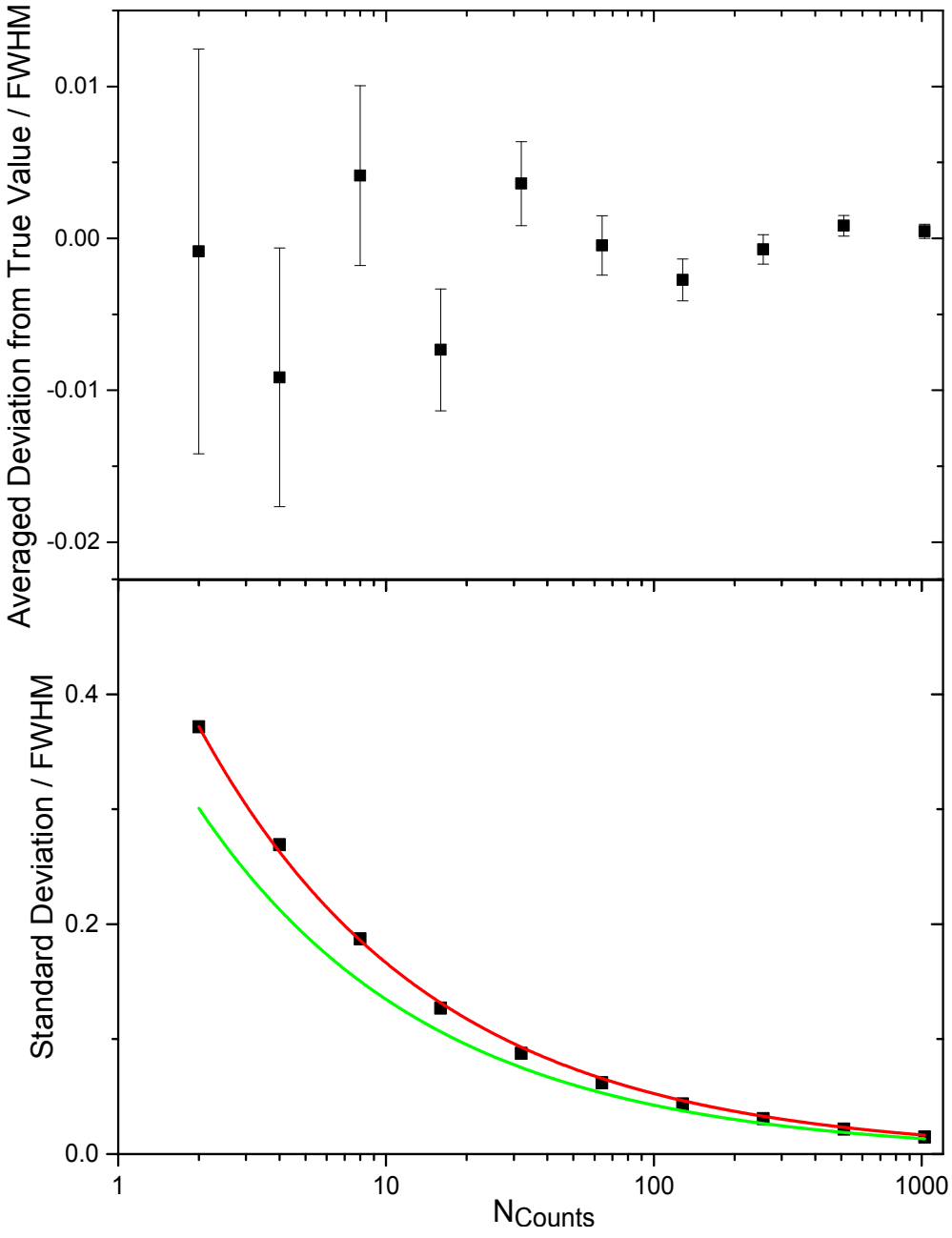

Figure 4.13.: Averaged deviation (top panel) of 1000 spectra per data point bootstrapped from the measured ^{211}Pb data shown in figure 4.3. The lower panel shows the corresponding standard deviations and an associated fit according to the formula $f(N_{Counts}) = A/\sqrt{N_{Counts}}$ (red line). The standard deviation expected for the mean (green line) is shown for comparison for the same number of normal distributed counts . For the ^{211}Pb data an accuracy of 0.1 FWHM corresponds to an absolute accuracy of $8 \cdot 10^{-7}$.

4.1.9. Calculation of Fit Errors

Two types of errors for the fit results of single peaks need to be determined by R and three for overlapping peaks. One is the statistical error. For the normal distribution the statistical error of the mean μ of a single peak is given by

$$\Delta\mu = \frac{\sigma}{\sqrt{N_{Counts}}} \tag{4.7}$$

where N_{Counts} is the number of counts in the peak. Unfortunately there is no closed form available for overlapping peaks and for the EMG. Additionally the statistical error is also influenced by the weighting, so that the statistical errors can only be determined empirically by generating and fitting comparable synthetic spectra and calculating the sample standard deviation. Reliable results can already be achieved with only 100 spectra, but typically 1000 or more are generated. This way all statistical errors for the peak centres and areal ratios are calculated.
The second type is the parameter error, which characterises how good the used function describes the data. It is calculated by changing consecutively the peak shape parameters by adding or subtracting their errors, fitting the measured data with the changed peak shape and taking the square root of the summed up squared differences from the originally fit.
For overlapping peaks their is in addition an error for the correction of the bias of the fit. If one peak is known, than the error of the corrected mass value is the correction itself. In the other case the fit with fixed parameters is done with the uncorrected peak distance, the corrected one and the uncorrected one plus twice the correction. The variation of the resulting mass values is the additional error contribution.
The total error is the square root of the quadratically added single errors. For overlapping peaks this also includes the error for the bias correction mentioned in section 4.1.7.
Typical values for the errors are

Statistical Error The statistical error for the tested EMG is for N_{Counts} counts

$$\sigma_{EMG} = \frac{0.52 * FWHM}{\sqrt{N_{Counts}}} \tag{4.8}$$

which is 23 % larger than the statistical error of the normal distribution. For the measurement of ^{211}Pb the relative statistical error is $4.8 \cdot 10^{-8}$.

Parameter Error The parameter error can be estimated by the results of section 4.1.6. For a single peak the error is $<= 0.01$ FWHM and $<= 0.05$ FWHM for overlapping peaks.

Bias Correction Typically the value of the bias correction is between practically no bias (for peaks with same intensities and distances over 2 FWHM) and 1 FWHM (for peaks with strongly different intensities and distances below 2 FWHM).

4.2. Statistical Significance

When going from simulated spectra to measured ones two problems occur that must be solved. One is the question whether the signal is a peak or background. The other one is the question for the goodness of the fit. Besides experimental aspects, like what is the typical background in a spectrum or are isobaric or isomeric contaminants known and can broaden the peak shape, statistical tests can give a hint to solve these problems.
The Kolmogorov-Smirnov-Test (KS-Test) is a statistical test which can compare either a sample of data points with a probability distribution or two sets of data with each other [Kolmogorov, 1933, Smirnov, 1944]. In the following only the first case is considered, which corresponds to the case of measured data and an expected distribution, but both cases are quite similar in handling.
The test compares the empirical cumulative distribution with an arbitrary cumulative distribution, the null hypothesis, and calculates the maximum distance between them. Based on this distance the probability that the data can be generated by the null hypothesis is calculated, the so called p-value. The ability to work with arbitrary cumulative distributions and not only with the ones of linear or normal distributions is a big advantage of the KS-Test.

The empirical cumulative distribution function for n data points x_i is defined as

$$F_{ecd,n}(x) = \frac{1}{n}\sum_{i=1}^{n} I_{[-\infty,x]}(x_i) \tag{4.9}$$

with the indicator function $I_{[-\infty,x]}(x_i)$ given by

$$I_{[-\infty,x]}(x_i) = \begin{cases} 1 & \text{for } x_i \leq x \\ 0 & \text{for else} \end{cases} \tag{4.10}$$

The Kolmogorov-Smirnov statistics for a given cumulative distribution function $F(x)$ is

$$D_n = \|F_{ecd,n}(x) - F(x)\| = \sup_x |F_{ecd,n}(x) - F(x)| \tag{4.11}$$

For the normal distribution the cumulative distribution function is

$$F_G(x, \mu, \sigma) = \frac{1}{2}\left(1 + \mathrm{erf}\left(\frac{x-\mu}{\sqrt{2\sigma^2}}\right)\right) \tag{4.12}$$

The cumulative distribution function of the EMG is directly connected with $F_G(x)$

$$F_{EMG}(x, \mu, \sigma, \eta, \tau) = F_G(u, 0, v) - \exp\left(-u + \frac{v^2}{2} + \log\left(F_G(u, v^2, v)\right)\right) \tag{4.13}$$

$$\text{with } u = \frac{x-\mu}{\tau} \text{ and } v = \frac{\sigma}{\tau} \tag{4.14}$$

With D_n the p-value can now be calculated [Durbin, 1973]

$$p = e^{-(6nD_n+1)^2/18n} \tag{4.15}$$

In R this calculation is done with the command *ks.test()*, which bases on the published code in [Wang et al., 2003].
In literature often a p-value below 0.05 is needed to reject a null hypothesis like the measured spectrum is generated by constant background and assume that there is more in the spectrum than only constant background. In particle physics even a 5σ event is needed to claim discovery of a new particle like the Higgs Boson [Aad et al., 2012, Sinervo, 2002], which corresponds to a p-value of only $5.7 \cdot 10^{-7}$. Figure 4.14 shows exemplary simulated spectra of a single peak plus background and the p-values for testing for the null hypothesis of constant background.

The meaning of the p-value must be handled carefully, because a high p-value does mean that there is a high probability that the data are generated by the null hypothesis. Actually it does not mean (what nevertheless quite often is assumed in publications) that the null hypothesis is true at all [Blume and Peipert, 2003, Nuzzo, 2014].
A limitation of the KS-Test is the test for background with very low statistics like 10 counts or below, because the KS-Test evaluates the data at the position of counts. A way to determine also for very low statistics the probability that an observed spectrum can result from constant background is to perform Monte-Carlo simulations of spectra with constant background and to count frequencies of spectra with a certain distribution. One distribution of interest is that all counts are located in a defined region of the spectra, whose size is the expected size of a peak. Figure 4.15 shows the results for this in dependence of the percentage of the defined region compared to the spectrum size and the number of counts.

The values for 0.1% describe the case that all counts in a complete mass spectrum are located in one peak width. 30% illustrates the case where the counts in a small spectrum with the size of three peak widths, for example because of close lying peaks, are located in one peak width.
For comparison of the simulation results with measured data care must be taken for the choice of the selected spectrum size, which influences the probabilities that the data result from constant background or real peaks.

The introduced statistical tests are tools to assist users in distinguishing between background signals and real peaks and benchmarking fit results.

4.3. Summary

The fit process introduced in section 4.1 is suitable to determine the centre of a single peak from only 2 counts to 10^4 counts with a negligible small systematic uncertainty. For the conditions like in the beamtime 2012, see section 5.1, this corresponds to a accuracy for ^{211}Pb of $8 \cdot 10^{-8}$ to $4 \cdot 10^{-10}$.
Overlapping peaks can be reliable fitted and the fit is robust against background and offsets in the initialization.
Different distribution functions can be used to describe peak shapes and errors are determined numerically for these distributions. The peak shape parameters must be

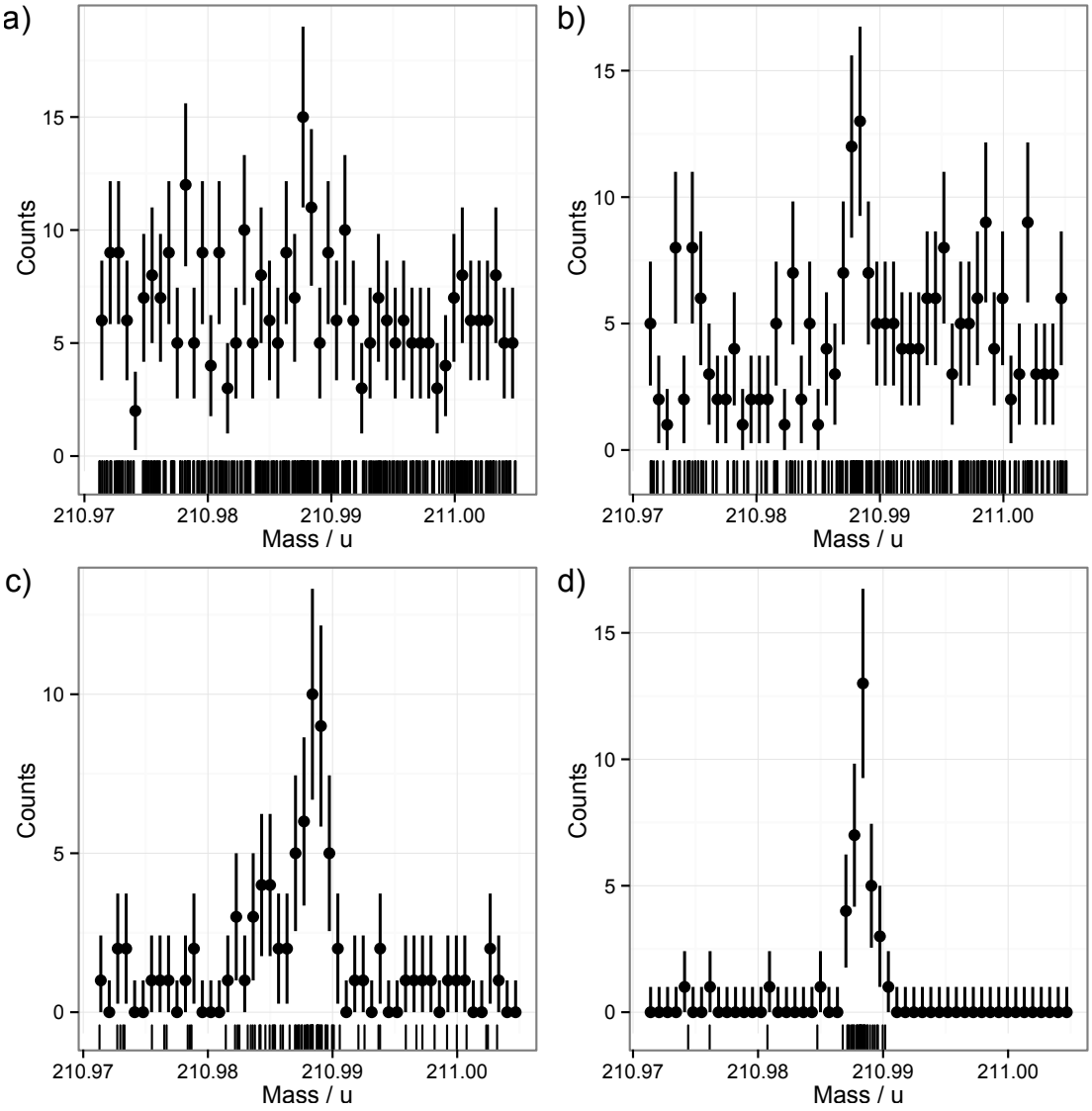

Figure 4.14.: Simulated spectra for one distribution with 32 ^{211}Pb ions (m = 210.9881886 u). A varying continuous constant background level is added. The KS-Test was applied for the different distributions. The null hypothesis is that the data are generated by constant background only. The results are given by the calculated p-values. Panel a) p-value $= 3.8 \cdot 10^{-2}$ (significance of 2σ), panel b) p-value $= 2.0 \cdot 10^{-3}$ (significance of 3σ), panel c) p-value $= 2.9 \cdot 10^{-5}$ (significance of 4σ), panel d) p-value $= 4.3 \cdot 10^{-7}$ (significance of 5σ)

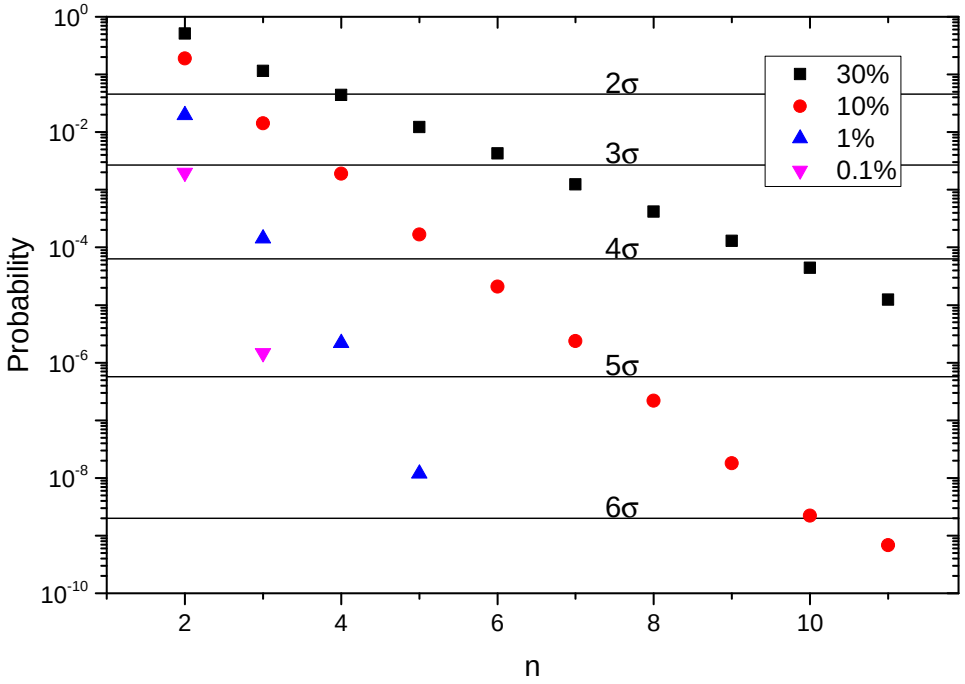

Figure 4.15.: Calculated probability for the condition that in a spectrum with n counts the peak could be generated by a constant background. All n counts are grouped in a region of x % of the total spectrum size.

known with an accuracy of 20% for single peaks and 10% for overlapping peaks to get negligible small errors of only 0.01 FWHM respectively 0.05 FWHM.
All together this reduces the numerical uncertainties so far, that the fit process does not limit the accuracy of mass measurements with the MR-TOF-MS. With further technical improvements mass measurements of short-lived exotic nuclei with accuracies below 10^{-7} are possible.
To support the decision, whether a cluster of counts is a real peak or just background (which is an elementary question for measurements with very low statistics), statistical tools are given in section 4.2.

5. Mass Measurements, Analysis and Results of ^{238}U-Projectile Fragments

In two experiments in 2012 and 2014 the FRS Ion Catcher has measured masses of projectile fragments with the MR-TOF-MS. A detailed description of the experiments can be found in [Purushothaman et al., 2013, Reiter, 2015]. A primary beam of 1000 MeV/u ^{238}U ions was focused on a Be target with an areal density of 1.648 g/cm^2. A Nb backing foil with an areal density of 0.223 g/cm^2 ensured a full ionization of the reaction products.
The produced projectile fragments were separated, identified and energy-bunched by the FRS. At the final focal plane of the FRS, see figure 5.1, the fragments were completely stopped and thermalized in the CSC.
In 2012 the CSC has been operated with an areal density of 3.1 mg/cm^2 He gas. 2014 it was increased to 3.5 mg/cm^2.
α-decaying ions extracted from the CSC can be identified with a silicon detector in

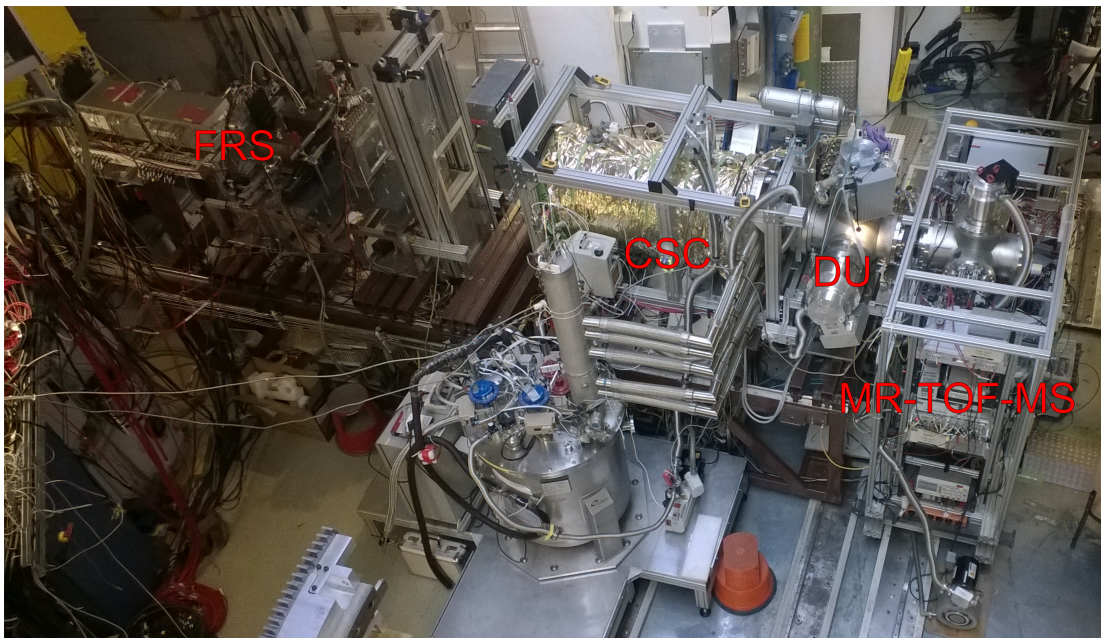

Figure 5.1.: Photo of the experimental setup of the FRS Ion Catcher at the final focal plane in 2014.

the DU, see figure 5.8. The extraction RFQ can be used as a mass filter to determine

charge state distribution and the existence of adducts for the ion of interest. Figure 5.9 shows exemplary the charge state distribution for extracted ^{220}Ra ions. The extracted ions are then transported to the MR-TOF-MS to perform high precision mass measurements.
In the beamtimes 2012 and 2014 projectile fragments and fission of ^{238}U was used to produce isotopes and isomers around the neutron shell closure N=126 and the double magic nuclei ^{132}Sn. In this thesis the analysis of the data of ^{211}Po, ^{211}Rn, ^{211}Fr taken in 2012 and ^{220}Ra taken in 2014 will be presented to demonstrate the possibilities of the developed fit algorithm and the experiment to perform high precision mass measurements with only 11 counts, overlapping peaks and calibrants with different number of turns than the ions of interest. Except for ^{211}Fr the measurements are the first direct mass measurement of these isotopes. Due to different software for data acquisition in the experiments in 2012 and 2014 the treatment of raw data and the time resolved calibration is hdone differently. Section 5.1 describes the analysis of the isotopes ^{211}Fr, ^{211}Po and ^{211}Rn measured in 2012 and section 5.2 of ^{220}Ra measured in 2014.

5.1. Experiment in 2012

5.1.1. Calibration and Fitting

In 2012 the data were measured in list-mode acquired with the commercial TDC software Digitizer. During the measurement singly charged ^{211}Pb ions from the ^{223}Ra-ion source were used for calibration and to determine the time dependent parameter b in the calibration formula 2.22. Calibrant and ion of interest have the same number of turns in the mass analyzer, thus formula 2.22 is overdetermined and the parameter c can be set to an arbitrary value.
The ion source was switched on periodically and the peak of the calibrant was fitted with a Gauss function and the Minimum χ^2 Estimation, compare figure 5.2 a). The ion source was not continuously on to prevent a to strong overlapp with the peak of the ion of interest. For the time without calibrant, parameter b was linearly interpolated. Figure 5.2 a) shows this exemplary for the measurement of ^{211}Fr. Figure 5.2 b) illustrates the effect for each measured ion. The overall effect is in increase of the mass resolving power by 50 %.
Even though the value of the time independent parameter t_0 is negligible small [Ito et al., 2013] its value can be easily measured offline

$$t_0 = 163 \pm 3\text{ns} \tag{5.1}$$

Afterwards all measured ions were time resolved calibrated with a self written program [Jesch, 2014] and from the measurement with the highest statistics the shape of the calibrant peak was fitted with an EMG [Purushothaman, 2014], compare section A.5, in the software Igor Pro [Igor Pro, 2015]. The number of exponentials in the fit function was varied to find the right one. Therefore the fitting started with

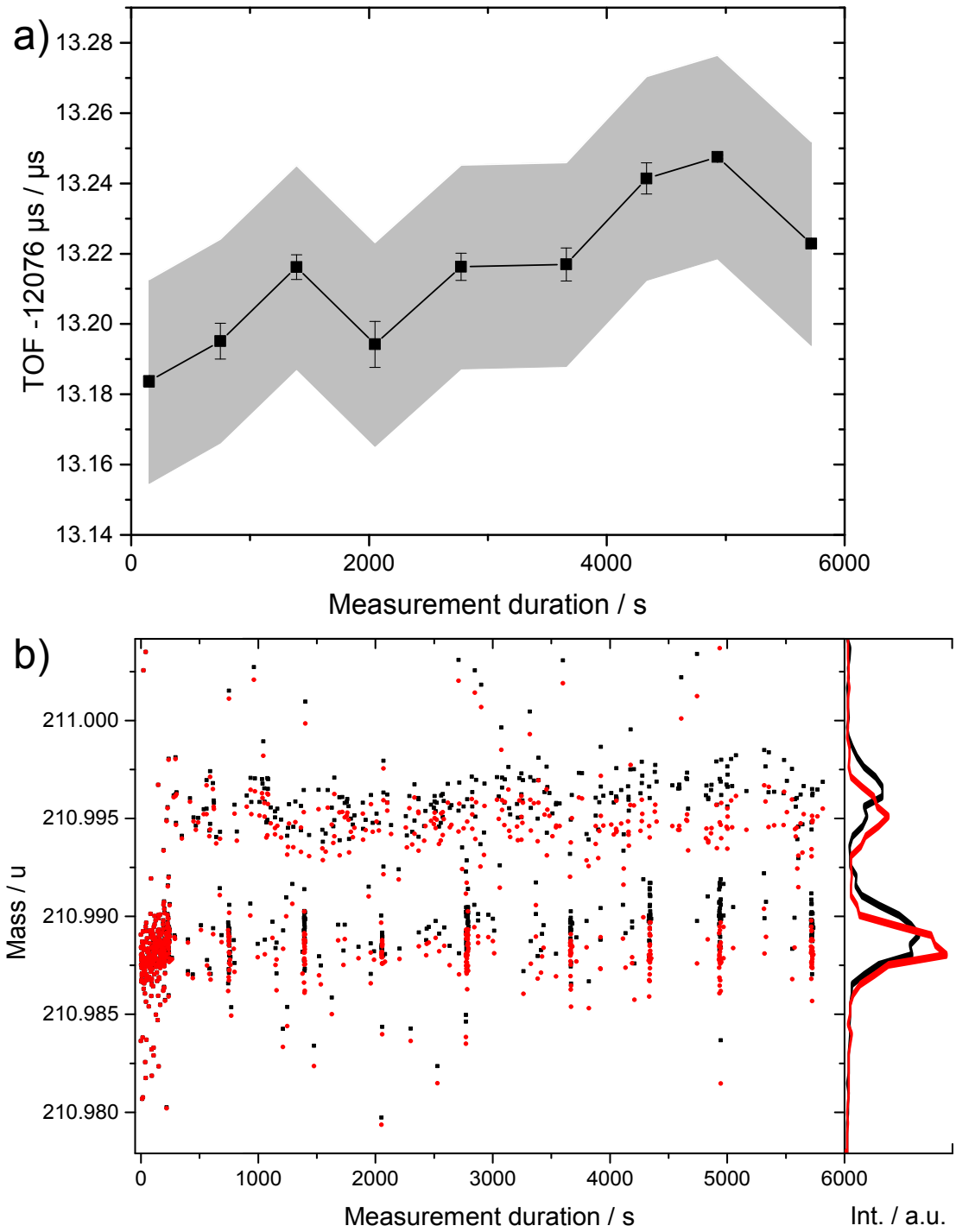

Figure 5.2.: Panel a): Drift of the time-of-flight for the ^{211}Pb reference ions (black squares). The grey area indicates the FWHM of the reference peak. Panel b): Recorded ions in the measurement of ^{211}Fr ions with (red) and without (black) time resolved calibration. The internal source for ^{211}Pb (m = 210.988 u) ions was periodically switched on and each data point in panel a) represents a determination of the peak centre and corresponding error. The projected histograms on the right side of panel b) show the improvement due to the time resolved calibration (red spectrum). The time resolved calibration increased the mass resolving power by 50 %.

3 exponentials on each side and exponentials with uncertainties of the corresponding weighting factor η_i equal or larger than this factor were removed. A sufficient description of the data is given by an EMG with two exponential on each side:

$$\begin{aligned}\sigma =& 3.54 \cdot 10^{-4} \\ \vec{\eta} =& (8.03 \cdot 10^{-1}, 1 - 8.03 \cdot 10^{-1}, 8.96 \cdot 10^{-1}, 1 - 8.96 \cdot 10^{-1}) \\ \vec{\tau} =& (5.32 \cdot 10^{-4}, 2.37 \cdot 10^{-3}, 5.85 \cdot 10^{-4}, 8.91 \cdot 10^{-3})\end{aligned} \tag{5.2}$$

The numerical errors of the parameters are

$$\begin{aligned}\Delta\sigma =& 0.28 \cdot 10^{-4} \\ \Delta\vec{\eta} =& (0.28 \cdot 10^{-1}, 0.28 \cdot 10^{-1}, 0.07 \cdot 10^{-1}, 0.07 \cdot 10^{-1}) \\ \Delta\vec{\tau} =& (0.38 \cdot 10^{-4}, 0.22 \cdot 10^{-3}, 0.21 \cdot 10^{-4}, 0.89 \cdot 10^{-3})\end{aligned} \tag{5.3}$$

The accuracy of the peak parameters is better 10%, which is required to make the influence of the parameter uncertainties negligible small, see section 4.1.6. The ^{211}Pb peak and the corresponding fit are shown in figure 4.3. The FWHM of the ^{211}Pb peak is $1.70 \cdot 10^{-3}$ u, which corresponds to a mass resolving power of

$$R_m \approx 125,000 \tag{5.4}$$

Afterwards the time resolved calibrated data were fitted in R with a mass window of $\pm$ 10 $\cdot$ FWHM around the peaks. To investigate the effect of the ratios of strongly overlapping peaks the spectra of ^{211}Po and ^{211}Rn were fitted twice: Once with complete data set and once only with the data where the intensity of the internal calibration ion source was reduced.
Important for the calculation of the statistical errors in the fits, compare section 4.1.9, is also the amount of background in the measured spectra. With in average 1 background count in 7 $\cdot$ FWHM it is the highest for the measurement of ^{211}Fr, which means that all spectra are nearly background free.
The fit process gives as result following values:

- The mass values of the fitted peaks and the corresponding mass errors subdivided in statistical, parameter and bias errors.

- The number of ions per peak with the corresponding errors subdivided in statistical and parameter errors.

The fit results for the measurement of ^{211}Fr, ^{211}Po and the two measurements of ^{211}Rn are shown in the figures 5.3, 5.4, 5.5 and 5.6 and in table 5.1. The corresponding errors are discussed in section 5.1.2.

The spectra of ^{211}Rn in figure 5.3 show a cluster of events around mass 210.995. This value fits to the mass of $^{211}Fr^{+}$. $^{211}Fr^{+}$ was produced in the FRS, but stopped in front of the CSC in this measurement. Also no other isotope produced in the FRS has the fitting mass value. The fact that no cluster of events at this mass is visible in the measurement of $^{211}Po^{+}$, compare figure 5.4 a) and b), can mean that the events are random artifacts or signals of dirt molecules from the residual gas in the CSC, that was ionized by the beam. The cluster can cause a shift of ^{211}Rn to the heavier

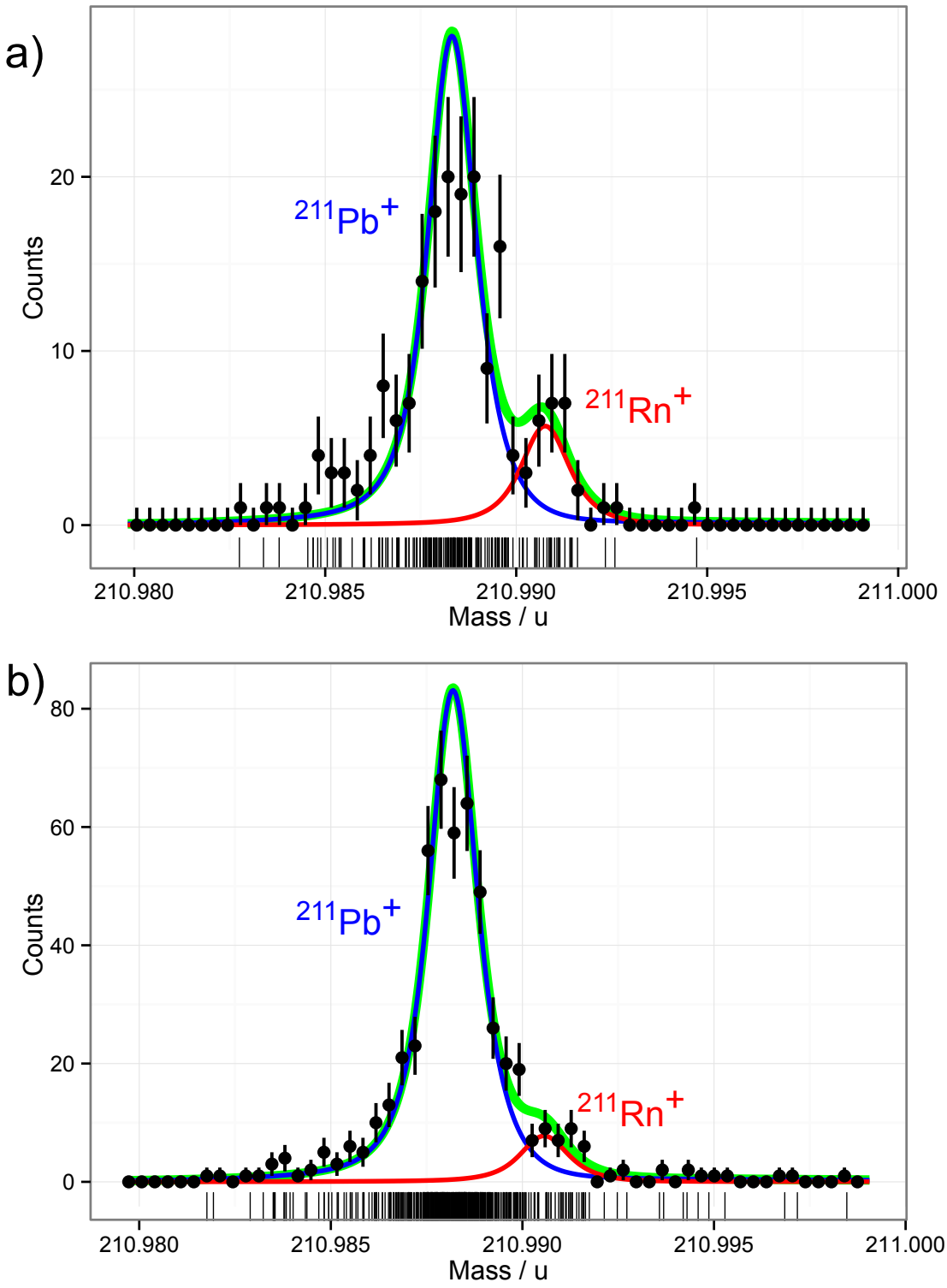

Figure 5.3.: Results of the first mass measurement of ^{211}Rn ions with the MR-TOF-MS. Panel a) shows the mass spectrum with a reduced intensity of the reference ions. Panel b) the full intensity of the reference ion source has contributed in the spectrum. The fitted calibrant peak is shown with blue lines, the fitted peak of the ^{211}Rn ions with red lines and the sum of both with green lines. The histograms of the measured ions are only drawn to guide the eye and are not relevant for the fit process. The areas of the fit functions are normalized to the areas of the histograms.

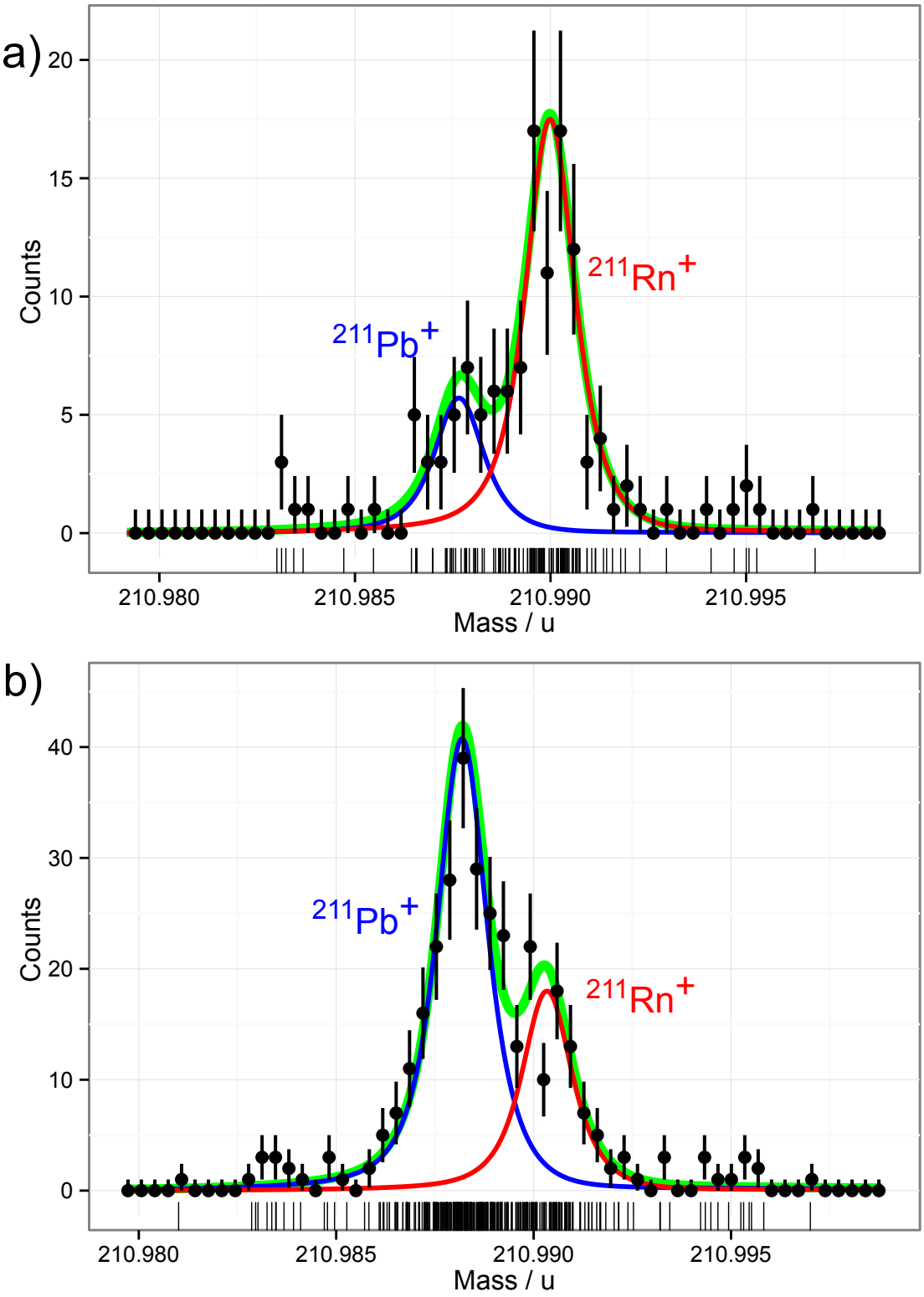

Figure 5.4.: Results of the second mass measurement of ^{211}Rn ions with the MR-TOF-MS. Panel a) shows the mass spectrum with a reduced intensity of the reference ions. Panel b) the full intensity of the reference ion source has contributed in the spectrum. The fitted calibrant peak is shown with blue lines, the fitted peak of the ^{211}Rn ions with red lines and the sum of both with green lines. The histograms of the measured ions are only drawn to guide the eye and are not relevant for the fit process. The areas of the fit functions are normalized to the areas of the histograms.

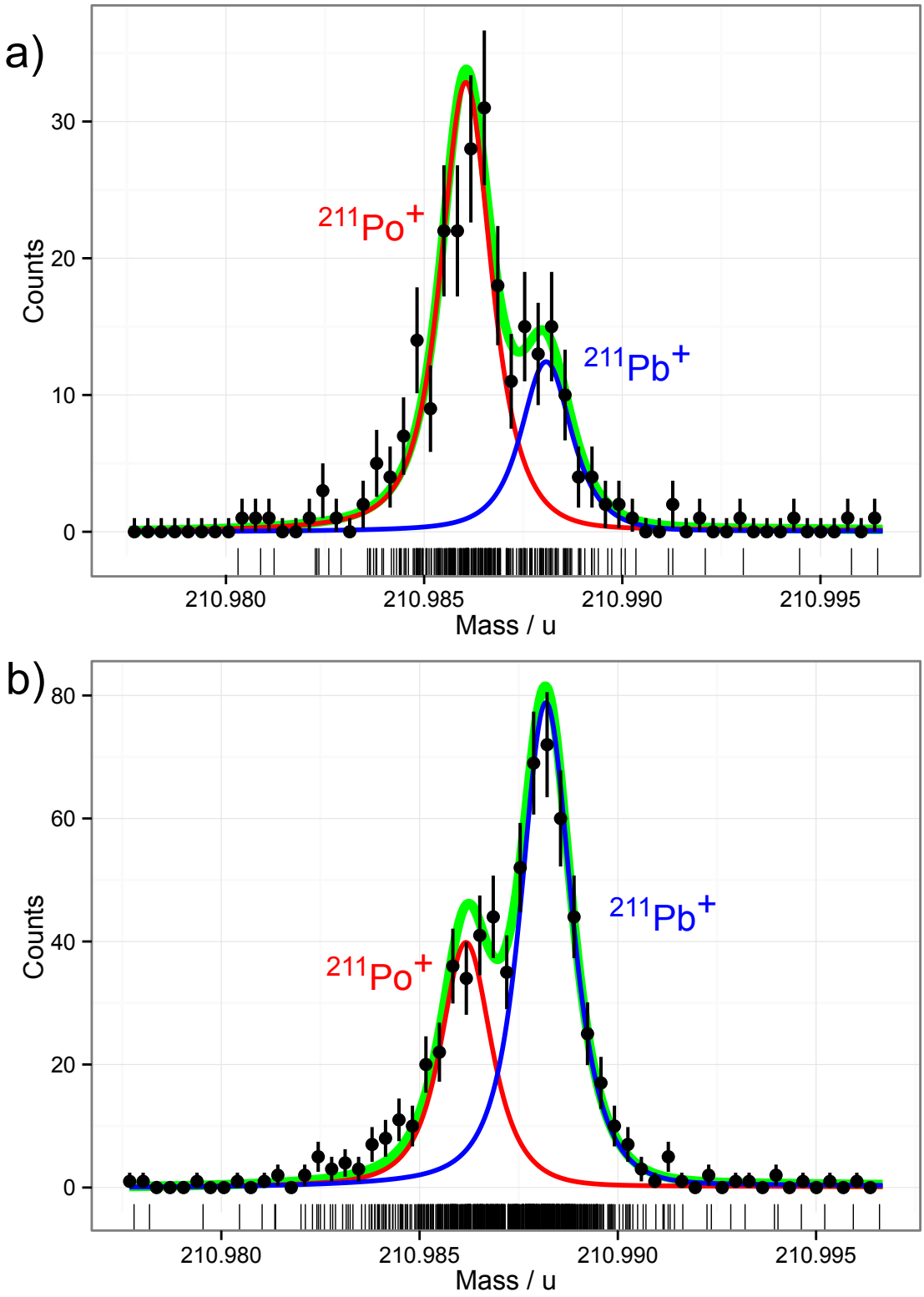

Figure 5.5.: Results of the mass measurement of ^{211}Po ions with the MR-TOF-MS. Panel a) shows the mass spectrum with a reduced intensity of the reference ions. Panel b) the full intensity of the reference ion source has contributed in the spectrum. The fitted calibrant peak is shown with blue lines, the fitted peak of the ^{211}Po ions with red lines and the sum of both with green lines. The histograms of the measured ions are only drawn to guide the eye and are not relevant for the fit process. The areas of the fit functions are normalized to the areas of the histograms.

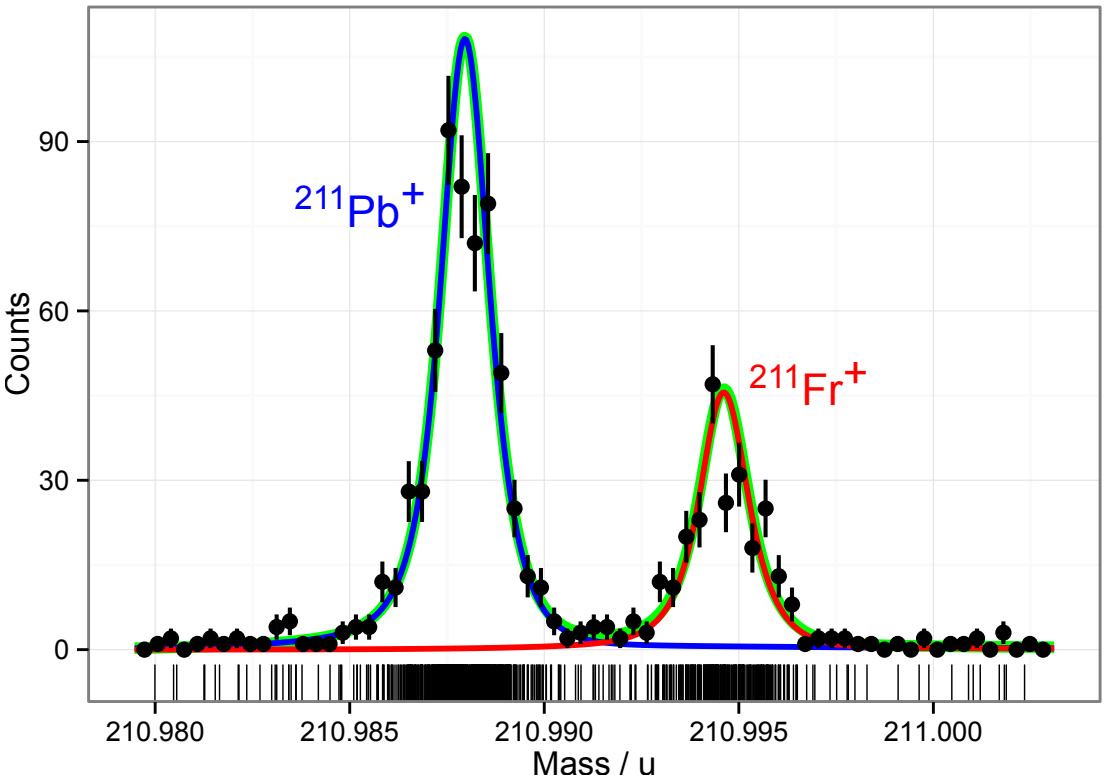

Figure 5.6.: Results of the mass measurement of ^{211}Fr ions with the MR-TOF-MS. The fitted calibrant peak is shown with a blue line, the fitted peak of the ^{211}Fr ions with a red line and the sum of both with a green line. The histogram of the measured ions is only drawn to guide the eye and is not relevant for the fit process. The areas of the fit functions are normalized to the area of the histogram.

		See Figure	Measured Mass Values / μu	Recorded Ions	Calibrant Ions
Complete Spectra	^{211}Fr	5.6	210995389	260	614
	^{211}Po	5.5 b	210986720	226	447
	^{211}Rn (1)	5.3 b	210991116	44	471
	^{211}Rn (2)	5.4 b	210990887	102	231
Intensity of Calibration Ions Reduced	^{211}Po	5.5 a	210986711	185	70
	^{211}Rn (1)	5.3 a	210991177	32	158
	^{211}Rn (2)	5.4 a	210991067	98	32

Table 5.1.: Measured mass values for ^{211}Fr, ^{211}Po and ^{211}Rn fragments analysed with bias correction. The ^{211}Rn fragments have been measured in two experiments as indicated. The numbers of recorded fragments and reference ions are listed. The corresponding errors are shown in section 5.1.2.

side, but the fit with the WMLE weights the cluster with a factor 4 less than the counts of ^{211}Rn.
A second small cluster, that is visible in all spectra, is at mass 210.983. This is even lighter than the lightest isotope with A=211 (^{211}Po), which means these counts are an molecule, whose mass can not be determined with high enough accuracy to shrink the list of possible molecules to a single one. These counts can cause a small shift of the fit of a nearby peak to the lighter side. This shift is reduced by the weighting of the WMLE, which weights the counts at mass 210.983 by a factor of 4 less compared to the counts of ^{211}Pb and a factor 3 for the counts of ^{211}Po.
Fits of the data without the events, that are lighter than 210.984 u or heavier than210.993 u, showed a deviation for ^{211}Fr of -0.03ppm, for ^{211}Po of -0.1ppm, -0.2ppm for the first measurement of ^{211}Rn and -0.3ppm for the second one. The influence of these deviations on the final results is negligible, compare figure 5.7.

5.1.2. Error of the Mass Determination

Three not fit related errors causes additional peak broadening, shifting and uncertainties.

Interpolated Drift Correction The ion source used for the time resolved calibration (TRC) was not permanently switched on, therefore the TRC is no perfect correction of the time-of-flight drifts. However the more often the ion source was switched on, the better will be the TRC and the smaller the additional peak broadening and shifting. The error σ_{IDC} caused by the broadening was estimated to be

$$\sigma_{\mathrm{IDC}} = \frac{\mathrm{x}}{\sqrt{\mathrm{N}_{\mathrm{IDC}}}} \tag{5.5}$$

$\mathrm{N}_{\mathrm{IDC}}$ is the number of times how often the ion source was switched on or the number of ions of interest, what ever is smaller. x is the standard deviation of the changes between consecutive fits of the calibrant peak and was determined from a measurement where the ion source was permanently on [Jesch, 2016]. It describes the drift between consecutive measurement of the peak position of the calibrant. For the case of the experiment 2012 it is

$$\mathrm{x} = 1.9\mathrm{ppm} \tag{5.6}$$

This error also includes a short term drift (second scale) caused by an unstable voltage(malfunction of electronics) in the mass analyzer.

Non-Ideal Ejection Due to a technical problem a pulsed voltages applied to the mass analyzer did not switch correctly. This resulted in different electrical fields during the ejection from the mass analyzer for ions with different mass-to-charge ratios. The characteristic of the voltage was measured and compared with simulations after the beamtime. The simulations showed that for ^{211}Po and ^{211}Rn this effect can be neglected, but ^{211}Fr was shifted relative to ^{211}Pb

by $1.7 \cdot 10^{-5}$u. The mass value of ^{211}Fr was accordingly corrected and the additional error contribution for ^{211}Fr was estimated to

$$\sigma_{\text{NIE}} = \begin{cases} +8 \cdot 10^{-6} u \\ -1.7 \cdot 10^{-5} u \end{cases} \tag{5.7}$$

Calibration The calibration of the time-of-flight spectrum has also an error. The error of parameter b is included in the error for the interpolated drift correction and the error for the recalibration is estimated by the errors of the fit of the calibrant ^{211}Pb. The uncertainty of t_0 is negligible small and the error of c is zero, because of the overdetermined of the fit formula.

All error contributions are listed in table 5.2. The dominant error, which limits the accuracy of the measured masses, is for the measurement with the highest statistics (^{211}Fr) the interpolated drift correction. It can be reduced by switching on the calibration ion source more often. A better separation of the peaks would allow to switch the calibrant ion source permanently on and can be achieved by increasing the mass resolving power of the MR-TOF-MS.
The dominant errors for the other measurements are the statistical errors and the errors of the bias correction. Both can be improved by increasing the mass resolving power, which is inversely proportional to the statistical error and better separation of overlapping peaks reduces the bias.

		Complete Spectra				Spectra with reduced intensity of calibration ions		
		^{211}Fr	^{211}Po	^{211}Rn (1)	^{211}Rn (2)	^{211}Po	^{211}Rn (1)	^{211}Rn (2)
Systematic	Interpolated Drift Correction / 10^{-7}	± 6.4	± 5.0	± 7.3	± 7.3	± 5.0	± 7.3	± 7.3
	Non-Ideal Ejection / 10^{-7}	+ 0.4 - 0.8						
Fit	Calibrant: Statistics / 10^{-7}	± 1.7	± 2.3	± 2.3	± 3.2	± 7.5	± 3.5	± 11.0
	Calibrant: Parameter / 10^{-7}	± 0.2	± 1.0	± 4.2	± 0.9	± 1.1	± 2.9	± 0.8
	Ion of Interest: Statistics / 10^{-7}	± 2.6	± 4.0	± 35	± 5.8	± 3.6	± 12.5	± 4.6
	Ion of Interest: Parameter / 10^{-7}	± 0.2	± 1.0	± 4.2	± 0.9	± 1.1	± 2.9	± 0.8
	Ion of Interest: Correction of Bias of Fit / 10^{-7}	± 1.3	± 6.9	± 36.5	± 6.8	± 8.0	± 9.5	± 6.8
	Total Error / 10^{-6}	+ 0.73 - 0.73	± 0.98	± 5.14	± 1.20	± 1.26	± 1.81	± 1.56

Table 5.2.: Compilation of all relative error contributions. ^{211}Rn was measured twice.

5.1.3. Results

The measured mass values and the comparison with the tabulated literature values in AME12 [Audi et al., 2012] are shown in figure 5.7 and table 5.3.
The relative deviation of the measured mass values m_{meas} from the literature values

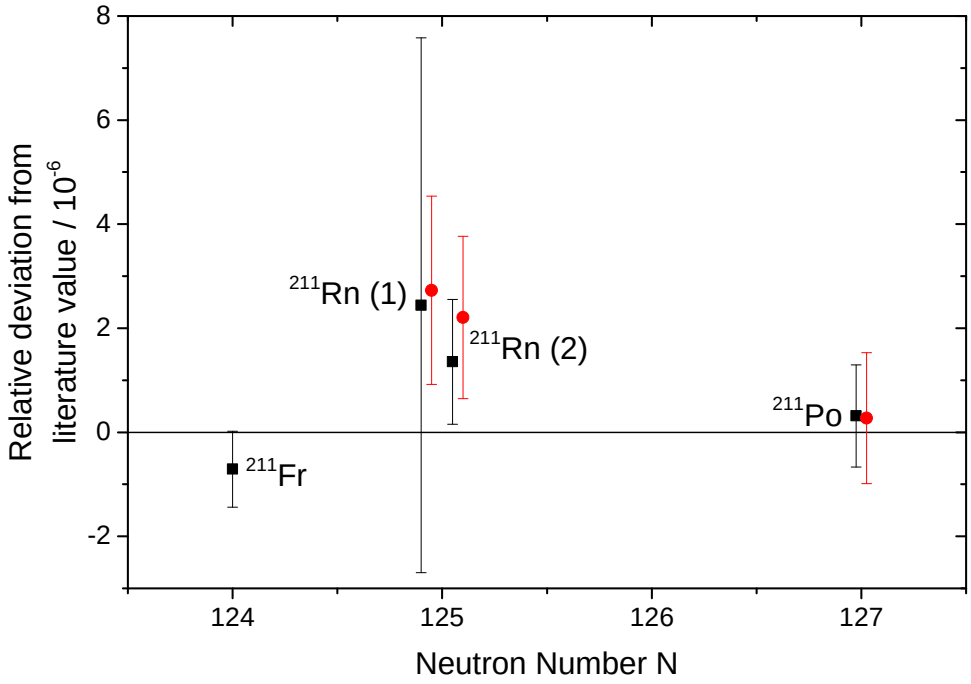

Figure 5.7.: Comparison of the measured mass values with the literature values from the atomic mass evaluation 2012 (AME12) [Audi et al., 2012]. The results of the complete spectra are shown in black and for the spectra with reduced intensity of the calibration ions in red. ^{211}Rn was measured twice.

m_{lit} is given by

$$\text{relative deviation} = \frac{m_{meas} - m_{lit}}{m_{meas}} \tag{5.8}$$

The comparison between the analysis of the complete spectra and the spectra with reduced intensity of the calibration ions showed that it is preferable to use the full data set for ^{211}Po and ^{211}Rn (2) and the one with lower intensity for ^{211}Rn (1).
The final mass values of the two ^{211}Rn measurements m_1 and m_2 were averaged with a mean and weighted with their errors σ_1 and σ_2.

$$m_{^{211}Rn,final} = \left(\sum_{i=1}^{2} \frac{m_i}{\sigma_i}\right) / \left(\sum_{i=1}^{2} \frac{1}{\sigma_i}\right) \tag{5.9}$$

The resulting error of the measurement is calculated with

$$\sigma_{^{211}Rn,final} = \left(\sum_{i=1}^{2} \frac{1}{\sigma_i^2}\right)^{-1/2} \tag{5.10}$$

The final mass values are

$$m_{^{211}\mathrm{Fr,final}} = (210995389 \pm 154)\mu\mathrm{u} \quad (5.11)$$

$$m_{^{211}\mathrm{Po,final}} = (210986720 \pm 207)\mu\mathrm{u} \quad (5.12)$$

$$m_{^{211}\mathrm{Rn,final}} = (210991002 \pm 211)\mu\mathrm{u} \quad (5.13)$$

Within the errors ^{211}Fr and ^{211}Po agree well with the literature values [Kowalska et al., 2009, Hahn et al., 1969]. For ^{211}Rn the mass values for the spectra with lower intensity do not agree within the errors with the literature value [Heßberger et al., 2000]. The results for the complete spectra agree better. The gap between second measurement and literature value can be explained by the contamination discussed in section 5.1.1. An isomeric state with a half-life long enough to measure it in the MR-TOF-MS and that would fit to the measured mass is not known in literature [Torgerson and Macfarlane, 1970, Heßberger et al., 2000]. The first measurement of ^{211}Rn agrees with the literature value, but has large errors.

These measurements demonstrated the capability of the developed fit process to evaluate even data in challenging cases like overlapping non-Gaussian peaks and low statistics. The use of the fit process enables the MR-TOF-MS to measure more challenging and exotic isotopes, where for example not completely resolved isomers prevented till now a direct mass measurement.
For ^{211}Po and ^{211}Rn it was also the first direct mass measurement.

5.2. Experiment in 2014

For the measurement and data analysis of ^{220}Ra some special challenges had to be overcome:

Half-Life ^{220}Ra has a half-life of only 17.9 ms, which is the most short-lived isotope whose mass was measured in a MR-TOF-MS.

Doubly Charged Ions As shown in figure 5.9 ^{220}Ra was extracted mainly as doubly charged ions from the CSC. Transport and storage of ions in the MR-TOF-MS are sensitive to the mass-to-charge ratio of the ions. This is also the first time that multiple charged ions are measured in a MR-TOF-MS.

Low Detection Rate Only 11 counts were detected in the experiment. Under this conditions future mass measurements of exotic nuclei will be performed.

	Complete spectra			Spectra with reduced intensity of calibration ions		Averaged
	^{211}Fr*	^{211}Po*	^{211}Rn (2)	^{211}Po	^{211}Rn (1)	^{211}Rn*
Mass (Exp) / μu	210995389 ± 154	210986720 ± 207	210990887 ± 254	210986711 ± 266	210991177 ± 382	210991002 ± 211
Mass Excess (Exp) / keV	-4279 ± 143	-12370 ± 193	-8489 ± 236	-12379 ± 248	-8219 ± 356	-8381 ± 197
Mass Excess (AME12) / keV	-4140 ± 12	-12432.1 ± 1.3	-8755 ± 7	-12432.1 ± 1.3	-8755 ± 7	-8755 ± 7

Table 5.3.: Overview of the measured mass values and mass excess for the isotopes ^{211}Fr, ^{211}Po and ^{211}Rn. ^{211}Rn was measured twice. The mass of an electron was added to the fitted value to get the mass of the neutral isotopes. The literature values are taken from the atomic mass evaluation 2012 (AME12) [Audi et al., 2012]. The results marked with the symbol * are the final values.

Calibration No isobaric calibrant with high count rate was available. Therefore two different ways to calibrate were used. One is the internal calibration with the isobar $^{34}S^{19}F_4$, simultaneously measured with ^{220}Ra. Because a time resolved calibration is not possible with 32 $^{34}S^{19}F_4$ events, the settings of the mass range selector were changed several times during the measurement to measure also ions with different mass-to-charge ratios and turn numbers than for ^{220}Ra. With the help of this method a clear identification also of ions with different turn numbers even in very complex spectra is possible. ^{124}Xe and ^{132}Xe were used for this calibration, which cover a large range of number of turns and minimize errors for the calibration due to different turn numbers. The disadvantage of the second method is that the calibrants are only periodically measured like in section 5.1, but therefore a time resolved calibration was possible.

Due to these challenges great care was taken in addition to identify the ions and the charge state in front of the MR-TOF-MS.
^{220}Ra was first identified in the FRS by the atomic number of the fully ionized nuclei and the mass-to-charge ratio. The identity of the ions extracted from the CSC was again checked in the DU by measuring the α-energy with a silicon detector, figure 5.8. The charge state distribution, see figure 5.9, was determined from a scan of the extraction RFQ in the mass filter mode [Reiter, 2015]. About 80 % of ^{220}Ra is extracted as doubly charged ions and 20 % as singly charged ions. Therefore the MR-TOF-MS was tuned to a mass-to-charge ratio of 110 $\frac{u}{e}$.

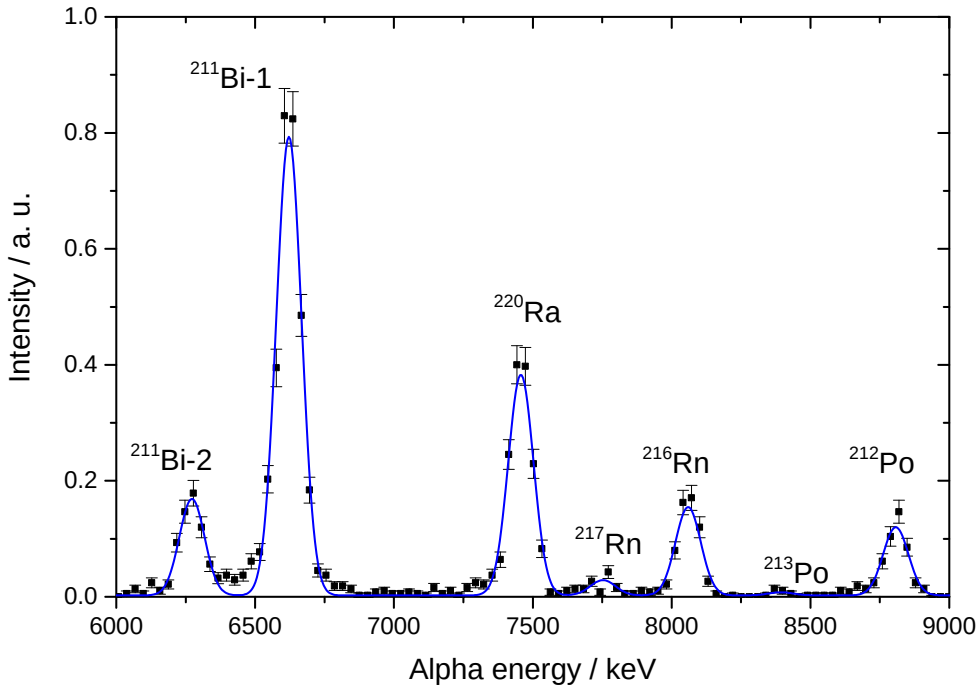

Figure 5.8.: α spectrum of ^{220}Ra measured in the diagnostics unit. The decay of ^{220}Ra is clearly separated and identified. The peaks of ^{211}Bi originate from decay products of the internal ^{223}Ra ion source, all other peaks from the beam. [Reiter, 2015]

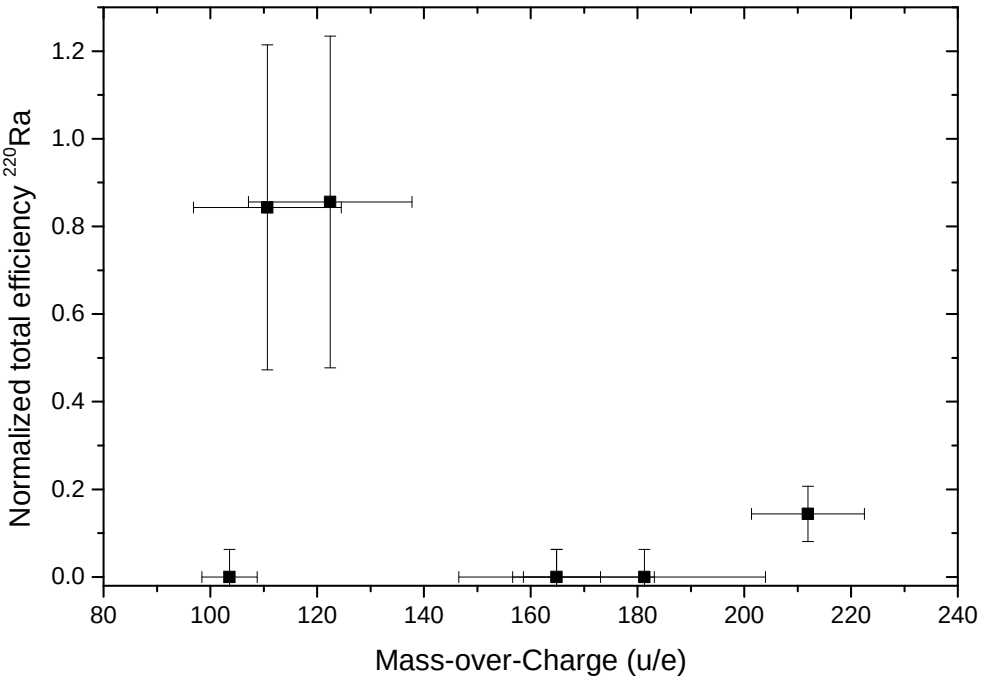

Figure 5.9.: Determination of the charge state of ^{220}Ra extracted from the CSC by using the extraction RFQ as a mass filter. Roughly 80 % of the ^{220}Ra is extracted as doubly charged ions and 20 % as single charged ions. Because of the mass resolving power of the mass filter, a scan at six different mass-to-charge ratios covered the whole region of interest. [Reiter, 2015]

5.2.1. Calibration And Fitting

In the experiment in 2014 the data were acquired with the software MAc andstored in the histogram mode with a binning of 1.6 ns. MAc was also used for calibration and TRC of the time-of-flight spectrum.
Figure 5.10 shows the measured time-of-flight spectrum with all ions from the internal ion source and the corresponding turn numbers. The time independent parameter t_0 was measured offline.

$$t_0 = 252 \pm 5\text{ns} \tag{5.14}$$

The calibration with the isotopes ^{124}Xe and ^{132}Xe was done with the formula 2.22. The parameter c was fitted in MAc

$$c = 6.893925 \cdot 10^{-8} \frac{u}{ns^2} \tag{5.15}$$

The TRC was done with the peak of ^{132}Xe and parameter b determined analogue to section 5.1.1. The peak of ^{132}Xe was also used to determine the parameters of the peak shape, see figure 5.11. Analogue to section 5.1.1 the number of exponentials was determined. The peaks have two exponentials on the left side and one on the

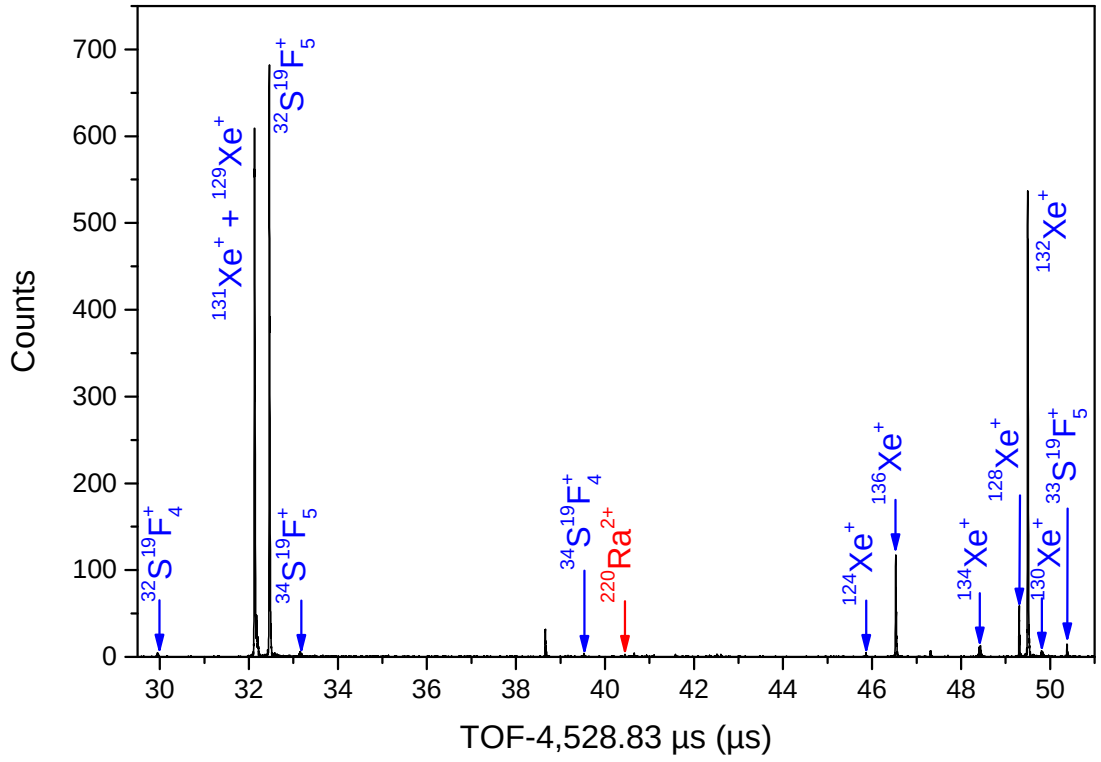

Figure 5.10.: Time-of-flight spectrum of the ^{220}Ra measurement. Identified peaks are labeled. The number of turns for each peak is given in brackets. The Xe-isotopes and the dissociation products of SF_6 originate from the internal ion source of the MR-TOF-MS.

right side.

$$\begin{aligned}\sigma &= 2.32 \cdot 10^{-4} \\ \vec{\eta} &= (9.68 \cdot 10^{-1}, 1 - 9.68 \cdot 10^{-1}, 1) \\ \vec{\tau} &= (2.49 \cdot 10^{-1}, 3.78 \cdot 10^{-4}, 5.90 \cdot 10^{-4})\end{aligned} \tag{5.16}$$

The numerical errors of the parameter are

$$\begin{aligned}\Delta\sigma &= 0.98 \cdot 10^{-4} \\ \Delta\vec{\eta} &= (0.12 \cdot 10^{-1}, 0.12 \cdot 10^{-1}, 0) \\ \Delta\vec{\tau} &= (0.78 \cdot 10^{-1} 1.31 \cdot 10^{-4}, 0.09 \cdot 10^{-4})\end{aligned} \tag{5.17}$$

The measured spectrum covers mass-to-charge ratios from 108 $\frac{u}{q}$ to 136 $\frac{u}{q}$ and to take this into account the parameters σ and $\vec{\tau}$ must be scaled linearly with the mass-to-charge ratio, see also section 2.4.3.
The FWHM of the ^{132}Xe peak is $9.04 \cdot 10^{-4}$ which corresponds to a mass resolving power of

$$R_m = 145,000 \tag{5.18}$$

The mass resolving power is slightly larger compared to the mass resolving power in section 5.1, but the number of turns is roughly halved and the mass ranged increased. The broader mass range enables the simultaneous measurement of ions from the

internal source from A=108 to A=136.

With the external calibration $^{34}S^{19}F_4$ could be identified and used for an internal

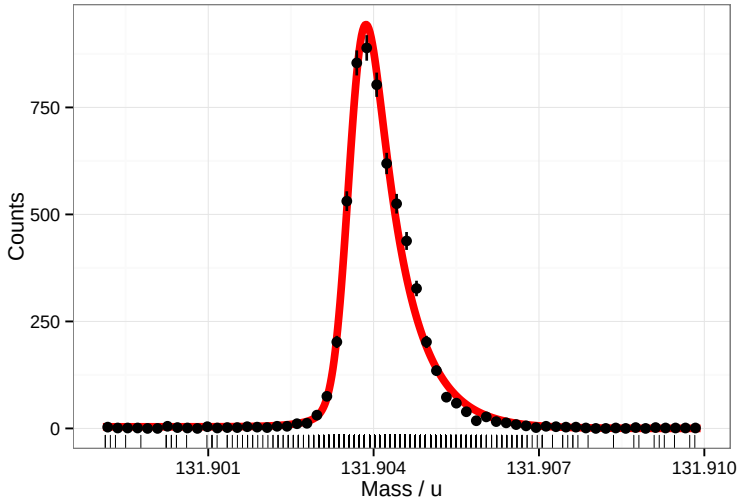

Figure 5.11.: Measured peak of ^{132}Xe, which was used to determine the peak parameters for the EMG function (red line). The FWHM of the peak is $9.04 \cdot 10^{-4}$ u. The histogram of the measured ions is only drawn to guide the eyes and are not relevant for the fit process. The measured data are shown in the rug graph.

calibration with the formula 2.14. The parameter a determined with MAc is

$$a = 5.269452 \cdot 10^{-12} \frac{u}{ns^2} \tag{5.19}$$

The drift of the time-of-flight is so small, that the peak shape from the external calibration can also be used for the internal calibration. The resulting error is negligible, compare section 4.1.6.

Then the data were exported from MAc with a mass window of $\pm$ 10 $\cdot$ FWHM or smaller for the case of close lying other peaks, but at least $\pm$ 5 $\cdot$ FWHM. The analysis of the peak widths showed that for the used tuning of the MR-TOF-MS all peaks of ions with an odd number of turns, see figure 5.10, have an enlarged variance and different peak shape. Also the peak areas were a factor of 10 lower than expected from the isotope pattern for peaks with odd turn numbers compared to the ones with even numbers. The reason for this is a misadjustment of the ion optics and different phase spaces for ions with odd and even turn numbers during the ejection from the mass analyzer [Yavor, 2009]. This effect gets reduced for higher number of turns and can also disappear. Therefore peaks with odd turn numbers are excluded from the analysis. The peaks of ^{129}Xe (N=129) and ^{131}Xe (N=128) overlap in the summed up spectrum, but for some settings of the MRS ^{131}Xe was measured alone. This data were used to make a single peak fit, unaffected by ^{129}Xe.

The background is quite low with 0.3 events in 10 $\cdot$ FWHM.

After the fit the mass values must be corrected for the different numerical method used for the determination of peak centres in the time resolved calibration. The time resolved calibration in MAc is done with a median, which is stable and faster then

the method introduced in section 4.1, but not that accurate. The effect is small and can be corrected in first order by a recalibration with the following equation:

$$m_{IOI} = m_{IOI,fit} \cdot \frac{m_{cal,lit}}{m_{cal,fit}} \tag{5.20}$$

m_{IOI} is the corrected mass value for an ion of interest. $m_{IOI,fit}$ and $m_{cal,fit}$ are the fitted mass values of an ion of interest and the calibrant. $m_{cal,lit}$ is the reference mass of the calibrant. The recalibration factor for the internal calibration with $^{34}S^{19}F_4$ is

$$\frac{m_{cal,lit}}{m_{cal,fit}} - 1 = \frac{m_{^{34}S^{19}F_4,lit}}{m_{^{34}S^{19}F_4,fit}} - 1 = 1.8 \cdot 10^{-6} \tag{5.21}$$

and for the external calibration with ^{132}Xe

$$\frac{m_{cal,lit}}{m_{cal,fit}} - 1 = \frac{m_{^{132}Xe,lit}}{m_{^{132}Xe,fit}} - 1 = 3.3 \cdot 10^{-6} \tag{5.22}$$

The fit results are given in table 5.4, figure 5.12 shows the fit of ^{220}Ra with internal calibration.

		Measured Mass / μu	Counts
Internally Calibrated	^{220}Ra	220.011634	11
Externally Calibrated	^{220}Ra	220.011448	11
	^{128}Xe	127903624	563
	^{131}Xe	130905133	3310
	^{136}Xe	135907245	1446
	$^{34}S^{19}F_4$	109961380	32
	$^{32}S^{19}F_5$	126964120	8398
	$^{33}S^{19}F_5$	127963594	111

Table 5.4.: Measured results for ^{220}Ra, calibrated internally with $^{34}S^{19}F_4$ and externally with ^{124}Xe and ^{132}Xe. The mass values are recalibrated with equation 5.20 and the mass of one or two electron was added to get the mass of the neutral isotopes. The corresponding errors are shown in section 5.2.2.

5.2.2. Error of the Mass Determination

Besides the statistical and parameter errors from the fit, the following errors contribute to the total error of the measurement:

Interpolated Drift Correction Analogue to the beamtime 2012 the calibrant ions for the external and internal calibration were not simultaneously measured with

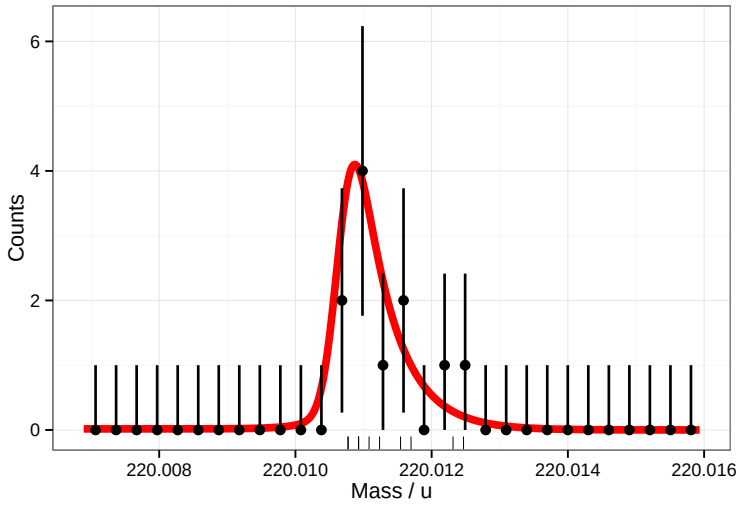

Figure 5.12.: Mass determination of ^{220}Ra (red) with only 11 events. The shown data are internally calibrated with $^{34}S^{19}F_4$. The histogram of the measured ions is only drawn to guide the eyes and are not relevant for the fit process. The measured data are shown in the rug graph.

the ions of interest. This causes a broadening of the peaks. The corresponding error is like in section 5.1.2 estimated to be

$$\sigma_{IDC} = \frac{x}{\sqrt{N_{IDC}}} \tag{5.23}$$

N_{IDC} is the number of times how often the ion source was switched on or the number of ions of interest, what ever is smaller. If no time resolved calibration was done, N_{IDC} is the number of ions of interest. x was determined in a different measurement from the broadening of a time resolved calibrated ^{133}I peak with width σ_I compared to the width σ_{Cs} of the calibrant peak of ^{133}Cs with the formula [Ayet San Andres, 2016].

$$\sigma_I = \sqrt{\sigma_{Cs}^2 + x^2} \tag{5.24}$$

$$x = 0.78\text{ppm} \tag{5.25}$$

Calibration The error of the calibration is similar to the beamtime 2012. The uncertainty of t_0 is negligible and the errors of the time dependent parameters a and b are included in the error of the interpolated drift correction. The error of the time independent parameter c was estimated by changing the time-of-flight of one calibrant by the uncertainty of time-of-flight determination and calculating new parameters b' and c'. By comparing the original and new sets of parameters a turn dependent error for c can be calculated, which is the difference in the calibration for a given number of turns N, see figure 5.13.
The error for the recalibration is estimated by the fit errors of the calibrant ^{132}Xe and $^{34}S^{19}F_4$ respectively.

All error contributions are relative errors and therefore independent of the charge of the measured ions. They are listed in table 5.5. The dominant errors are the statistical

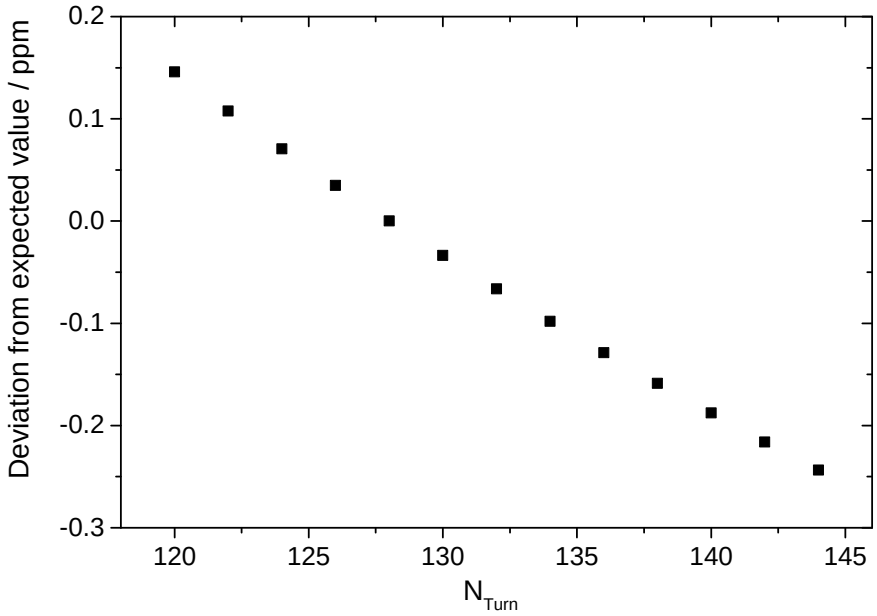

Figure 5.13.: Turn dependent error of parameter c. Shown are only the errors for even numbers of turns. Because of the tuning of the MR-TOF-MS the measurement of ions with odd turn numbers was disturbed. The error is zero for N=128, which is the number of turns for the calibrant ^{132}Xe.

errors of ^{220}Ra (11 events) and for the internal calibration of the calibrant $^{34}S^{19}F_4$ (32 events). This count rates are expected ones for the measurements of exotic nuclei, whose production rates are limited. An improvement of the errors is only possible by improving the mass resolving power.

		Internally Calibrated	Externally Calibrated						
		^{220}Ra	^{220}Ra	^{128}Xe	^{131}Xe	^{136}Xe	$^{34}S^{19}F_4$	$^{32}S^{19}F_5$	$^{33}S^{19}F_5$
Systematic	Interpolated Drift Correction / 10^{-7}	± 2.4	± 4.5	± 4.5	± 4.5	± 4.5	± 4.5	± 4.5	± 4.5
	Calibration with Different Turn Numbers / 10^{-7}		± 1.9	± 0.3	± 0.0	± 0.3	± 1.9	± 0.3	± 0.3
Fit	Calibrant: Statistics / 10^{-7}	± 6.3	± 0.5	± 0.5	± 0.5	± 0.5	± 0.5	± 0.5	± 0.5
	Calibrant: Parameter / 10^{-7}	± 0.4	± 0.0	± 0.0	± 0.0	± 0.0	± 0.0	± 0.0	± 0.0
	Ion of Interest: Statistics / 10^{-7}	± 11.4	± 11.2	± 1.5	± 0.6	± 1.0	± 6.4	± 0.4	± 3.4
	Ion of Interest: Parameter / 10^{-7}	± 0.2	± 0.5	± 0.1	± 0.1	± 0.1	± 0.2	± 0.0	± 0.2
	Total Error / 10^{-7}	± 13.2	± 12.2	± 4.8	± 4.6	± 4.6	± 8.1	± 4.6	± 5.7

Table 5.5.: Compilation of all relative error contributions.

5.2.3. Results

The results for the data analysis of the ^{220}Ra-measurement are shown in table 5.6 and figure 5.14. The relative deviation of the measured mass values m_{meas} from the literature values m_{lit} is given by

$$\text{relative deviation} = \frac{m_{meas} - m_{lit}}{m_{meas}} \tag{5.26}$$

Internal and external calibration give similar results for mass value and error of ^{220}Ra.

	Internally Calibrated ^{220}Ra	Externally Calibrated ^{220}Ra*
Mass (Exp) / μu	220011748 $\pm$ 290	220011762 $\pm$ 268
Mass Excess (Exp) / keV	10838 $\pm$ 270	10664 $\pm$ 250
Mass Excess (AME12) / keV	10271 $\pm$ 8	10271 $\pm$ 8

Table 5.6.: The literature value is taken from the AME12. The result marked with the symbol * is the final value for the measurement of ^{220}Ra.

The final mass value for ^{220}Ra is the one from the external calibration, because of the smaller error.

$$m_{^{220}Ra} = (220011762 \pm 276)\mu u \tag{5.27}$$

It deviates by 1.5 σ from the literature value. No long-lived isomeric state of ^{220}Ra is known so far that would fit to the measured mass [Ruiz, 1961, Andreyev et al., 1989, Heßberger et al., 2000].
The fact that internal and external calibration give the same results means that the deviation does not result from the calibration with different numbers of turns.
Besides ^{220}Ra six stable isotopes and molecules were measured, which allow a determination of an unknown systematic error analogue to [Chen, 2008]. But it turned out, that the errors of the measured masses are already overestimated.

This measurement demonstrated that the MR-TOF-MS can measure the mass of very short-lived isotopes with only 11 events. In addition the calibration with different turn numbers was tested successfully and agrees with the results of the calibration with isobars. It was also the first direct mass measurement of ^{220}Ra and the low energy measurement of the isotope with the most challenging ratio of mass to half life so far.

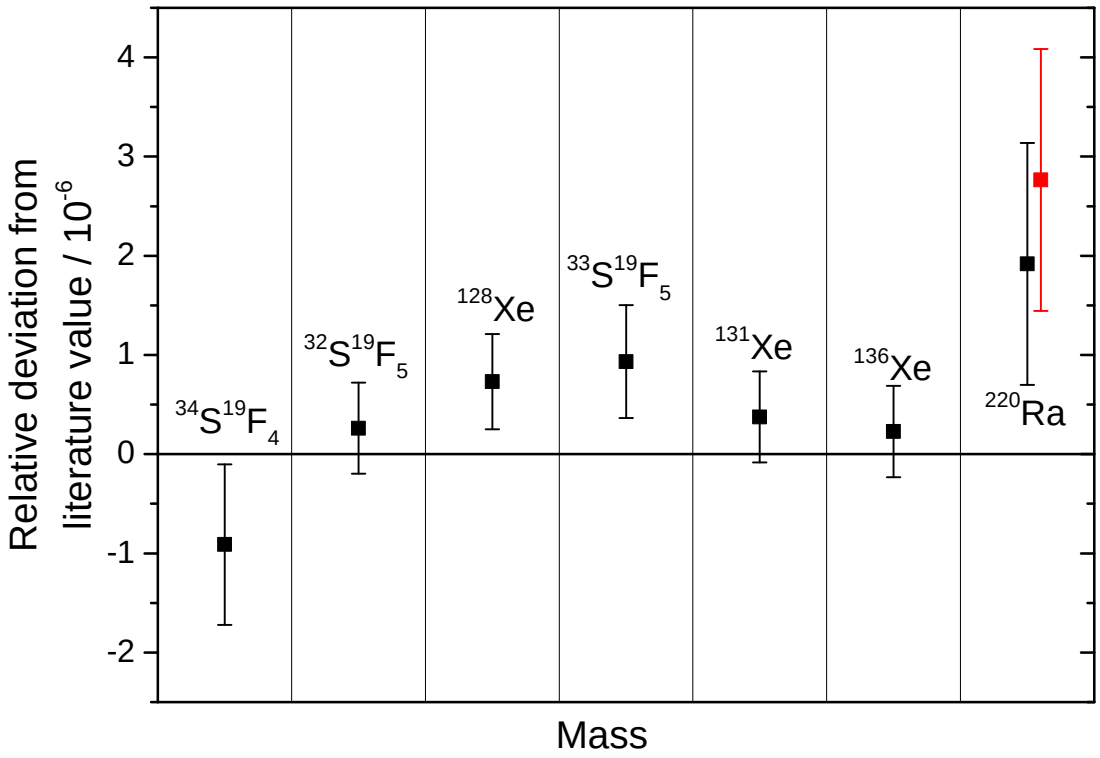

Figure 5.14.: Comparison of the measured neutral mass values (charge q=0) with the literature values from the AME12. The internally calibrated ^{220}Ra is shown in red, the externally calibrated isotopes and molecules in black. The chemical and electron bounding energy is neglected.

5.3. Comparison of the Experimental Results with Theoretical Predictions

Mass measurements are important to test the predictive power of theoretical models. In figure 5.15 the measured mass excesses from the sections 5.1 and 5.2 are compared with theoretical predictions. The theoretical models are the microscopic-macroscopic descriptions ETFS-1 [Aboussir et al., 1995], WS3 [Liu et al., 2011], FRDM [Moller et al., 1995], base on the shell model, like the model of Duflo-Zuker [Duflo and Zuker, 1995] or the Hartree-Fock-Bogoliuboy theory [Dobaczewski et al., 1996].
The predictive power of the different models can be quantitatively characterized by the standard deviations σ. Table 5.7 gives an overview of the standard deviations for the compared theories.

Within the errors only the Duflo-Zuker model and WS3 agree well with the experimental values. Both theoretical models have an average deviation of 0.15 MeV.

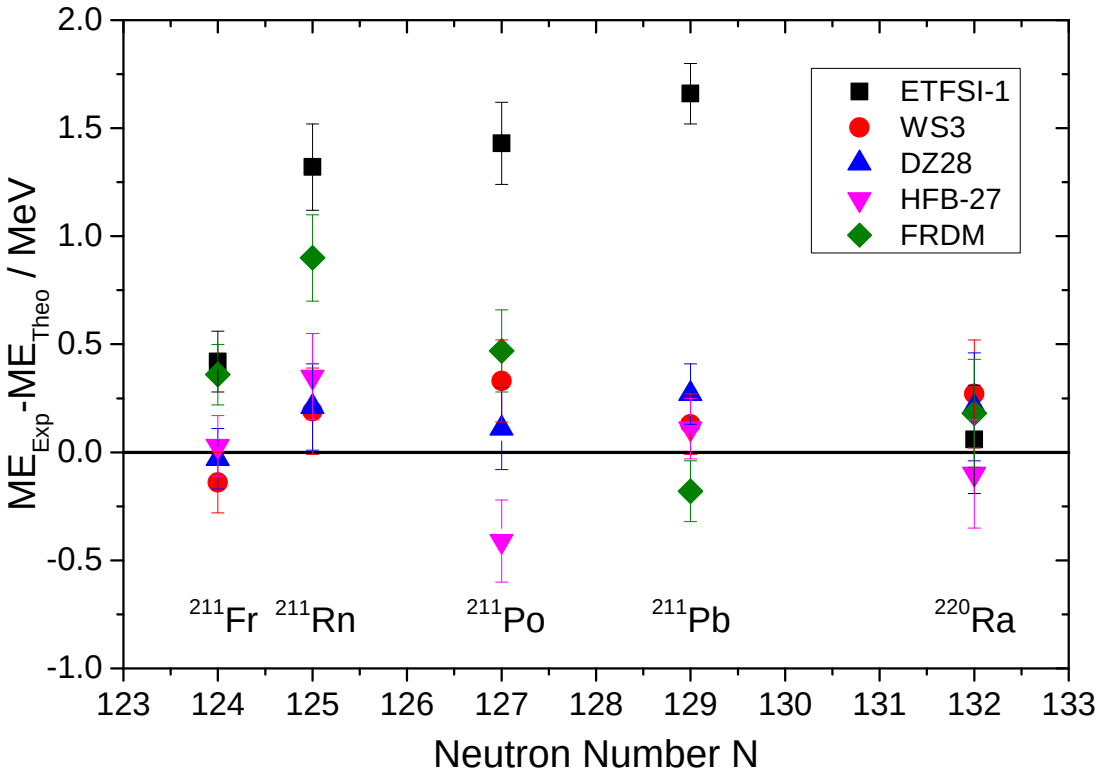

Figure 5.15.: Comparison of the measured mass excesses for ^{211}Fr, ^{211}Po, ^{211}Rn, ^{211}Pb and ^{220}Ra with theoretical predictions of the models ETFS-1 [Aboussir et al., 1995], WS3 [Liu et al., 2011], DZ28 [Duflo and Zuker, 1995], HFB-27 [Dobaczewski et al., 1996] and FRDM [Moller et al., 1995]. The mass excess of ^{211}Pb was determined by using ^{211}Fr as reference.

Theory	σ / MeV
ETFSI-1	0.62
WS3	0.16
DZ28	0.11
HFB-27	0.25
FRDM	0.35

Table 5.7.: Standard deviations σ for the measured isotopes for different theoretical models.

5.4. Outlook on Future Error Contributions

The errors contributing to the beamtimes 2012 and 2014 as discussed in the sections 5.1.2 and 5.2.2 can be further reduced for future experiments. The non-ideal ejection was already removed before the beamtime in 2014. Also the error of the interpolated drift correction can be further reduced by letting the calibration ion source switched on for the full time. Ideally one calibrant ion should be measured in every measurement cycle of the MR-TOF-MS, which would enable a time resolved calibration without linear interpolation of the time dependent parameters and negligible error. Significantly higher rates should be avoided to prevent completely space charge effects.

The next largest error contributions are the statistical errors, followed by the calibrations with different numbers of turns. The statistical error σ_{stat} is for Gauss and EMG shaped peaks proportional to the inverse of the mass resolving power R_m and the square root of the number of counts N_{Counts}, compare section 4.1.8

$$\sigma_{\mathrm{stat}} \propto \frac{1}{R_m \sqrt{N_{\mathrm{Counts}}}} \tag{5.28}$$

N_{Counts} will be also in future experiments comparable small, so that a reduction of σ_{stat} is only possible by increasing R_m. With an ideal drift correction and an increase of the mass resolving power to 400.000 (which corresponds to an increase in time-of-flight from 5 ms to 14 ms [Plaß et al., 2015] and is still less than one half-life of ^{220}Ra) the accuracy of a measurement with only 11 counts can be reduced to $4.5 \cdot 10^{-7}$. Additionally an increase of the time resolving power will also reduce the uncertainty in the determination of the time of flight of a peak and hence reduce the error for the calibration with different number of turns.
Table 5.8 shows a compilation of error contributions from the beamtimes in 2012 and 2014 and estimated error contributions for future measurements. An improvement of the interpolated drift correction by a factor of 2 compared to 2014 through a different operation mode of the calibration ion source and thermal and electrical stabilization of the MR-TOF-MS is reasonable. The Non-ideal ejection was already removed before 2014. With the help of a laser ablation ion source [Hornung, 2013] the difference in the numbers of turns for calibrant and ion of interest will be reduced to two, compare figure 5.13. The increase of the mass resolving power is counter proportional to the statistical error, which will be improved at least by a factor of 3.

The MR-TOF-MS has a systematic uncertainty of less than $1 \cdot 10^{-7}$ [Dickel et al., 2015a]. Together with the non-statistical errors from table 5.8, future measurements will have a systematic uncertainty of $2 \cdot 10^{-7}$. To reduce also the statistical error to $2 \cdot 10^{-7}$ only 36 detected ions are needed at a mass resolving power of 400,000, which reduces the residual uncertainty for mass measurements of exotic nuclei to $3 \cdot 10^{-7}$. With only 10 ions a uncertainty of $4.5 \cdot 10^{-7}$ can be reached.

	2012	2014	Future
Interpolated Drift Correction / 10^{-7}	19 / $\sqrt{N_{IDC}}$	7.8 / $\sqrt{N_{IDC}}$	4 / $\sqrt{N_{IDC}}$
Non-Ideal Ejection / 10^{-7}	$\leq 6^*$	0	0
Calibration with Different Turn Numbers of Calibrant and Ion of Interest / 10^{-7}	5^*	1.9	0.3
Statistics / 10^{-7}	$42/\sqrt{N_{Counts}}$	$36/\sqrt{N_{Counts}}$	$12/\sqrt{N_{Counts}}$

Table 5.8.: Compilation of relative error contributions of the mass determinations for the beamtimes in 2012 and 2014 and estimated for future mass measurements. $\sqrt{N_{Counts}}$ is the number of ions of interest in a peak. N_{IDC} (compare figure 5.2) is the number of times how often the ion source was switched on or the number of ions of interest, what ever is smaller. The values marked with the symbol * was taken from [Jesch, 2016].

6. Summary and Conclusions

Mass measurements of short-lived uranium projectile fragments were performed for the first time with a Multiple-Reflexion-Time-of-Flight Mass Spectrometer (MR-TOF-MS). A major part of this doctoral work was a novel development of a data analysis method for the MR-TOF-MS mass measurements of exotic nuclei at the fragment separator FRS at GSI. The developed method was successfully applied to the data obtained from two pilot experiments with the MR-TOF-MS at the FRS in 2012 and 2014. A substantial upgrade of the experimental setup of the MR-TOF-MS was also performed in the frame work of this doctoral thesis after the first run.

In the experiments projectile fragments were created with 1000 MeV/u ^{238}U ions in a Be/Nb target at the entrance of the in-flight separator FRS. The exotic nuclei were spatially separated, energy bunched and slowed down with the ion-optical system of the FRS combined with monoenergetic and homogeneous degraders. At the final focal plane of the FRS the fragments were completely slowed down and thermalized in a cryogenic stopping cell (CSC) filled with 3-5 mg/cm^2 pure helium gas. The exotic nuclei were fast extracted from the CSC to enable mass measurements of very short-lived fragments with the MR-TOF-MS. The achievement of this goal was successfully demonstrated with the mass measurement of ^{220}Ra ions with a half-life of 17.9 ms and 11 detected events. The mass measurements of the isobars ^{211}Fr, ^{211}Po and ^{211}Rn have clearly demonstrated the scientific potential of the MR-TOF-MS for the investigation of exotic nuclei and the power of the data analysis system. Difficult measurements with overlapping mass distributions with only a few counts in the measured spectra were the challenge for the new data analysis method based on the maximum likelihood method. The drifts during the measurements were corrected with the developed time-resolved calibration method. After the improvements of the setup as a consequence of the experience of the first experiment in 2012 and the applied time-resolved calibration method a mass resolving power of 400,000 has been achieved in the experiment in 2014.

The achieved mass accuracy in these pilot experiments were about $1 \cdot 10^{-6}$. The contribution of the software and the resulting systematic errors were in the 10^{-8} range. The reliability of the present analysis method was carefully checked in detailed simulations with a realistic peak shape approximated by an exponentially modified Gaussian distribution. Both list mode data and measured histograms were treated in the data analysis. The analysis method was tested with strongly overlapping mass distributions and low count rates including a variable amount of back ground.

In summary, the experimental setup for mass measurements of very rare and short-

lived nuclei and the corresponding data analysis have reached with this work and results of the present thesis a great potential for high-resolution measurements in future experiments. There mass measurements with 10 events can be performed with a residual uncertainty of $4.5 \cdot 10^{-7}$ at a mass resolving power of 400,000.

A. Appendix

A.1. Definitions

- **List-mode** The time-of-flight t is the difference between the recorded time of the detector t_2 and the time of the ejection pulse from the trap t_1. t_1 of each ion is used to apply the drift correction. The list-mode data are defined by the recorded t and t_1 for each ion.

- **Un-/Binned Data** Binned data are grouped by quantization of a continuous property of the data. Examples are the digitalization of analogue signals or the generation of a histogram. In this work unbinned data are defined by a sequence of events with an abundance of only 1 and an arbitrary density distribution.

- **Bootstrapping** Bootstrapping is a tool in statistics to generated a new spectrum with a conserved probability distribution. The new spectrum results from drawing randomly with a uniform probability events with replacement from the measured spectrum. The number of the events in the new spectrum can be selected.

A.2. Numerical Methods for Mass Determination

Several methods are available to determine the centroid of a distribution.

Mean The mean μ is the average value of a sample of n data points x_i, i=1..n

$$\mu = \frac{\sum_{i=1}^{n} x_i}{n} \tag{A.1}$$

with the sample variance σ^2

$$\sigma^2 = \frac{1}{n-1} \sum_{i=1}^{n} (x_i - \mu)^2 \tag{A.2}$$

The error of the mean σ_{mean} and the sample variance σ_{σ^2} for normal distributed samples are [Ahn and Fessler, 2003]

$$\sigma_{mean} = \frac{\sigma}{\sqrt{n}} \text{ and } \sigma_{\sigma^2} = \sigma^2 \sqrt{\frac{2}{n-1}} \tag{A.3}$$

It is easy to implement, but not robust against outlier [Leys et al., 2013] or able to determine peak areas. Overlapping peaks can not be treated and the actual distribution of the data is not taken into account.

Median In a sorted list of events the median is the element in the middle of the list. The error of the median has no easy universal formula, but for normal distributed data it is related with the error of the mean via [Kenney and Keeping, 1962]

$$\sigma_{\text{Median}} = \frac{\pi(2n+1)}{4n}\sigma_{\text{mean}} \tag{A.4}$$

It is very robust in presence of background and outliers. The disadvantages are that it can not be used for overlapping peaks, it does not consider the actual peak shape and peak areas can not be determined.

Minimum χ^2 Estimation This method adjusts a set of model parameters $\vec{\theta}$ to describe best a set of n data points of the form (x_i, y_i) with $i = 1, ..., n$ and the errors σ_i. The model formula has the form $f(x,\vec{\theta})$. The parameters $\vec{\theta}$ give the best description of the data points, when the equation

$$\chi^2 = \sum_{i=1}^{n} \frac{\left(y_i - f\left(x_i, \vec{\theta}\right)\right)^2}{\sigma_{i^2}} \tag{A.5}$$

has a minimum. It works with user-defined functions and an arbitrary number of peaks. Background can be fitted as well and errors for the data points can be easily included in the fit process. The weighting with the error σ_i^2 makes it also robust against outliers.
The method needs binned data, a minimum number of bins and events per bin to fit data reliably, which means for the experimentalist that at least 20 counts for a single normal distributed peak are needed [Taylor, 1982]. As a rule of thumb no bin should have a frequency below 5 [Healey, 2014].

Maximum Likelihood Estimation The Maximum Likelihood Estimation (MLE) assumes that the data are the result of a probability distribution. The data depend on some unknown parameters. The MLE searches for the set of parameters that describes the data most probably by minimizing the likelihood function, see appendix A.3.
This method can handle overlapping peaks with very low statistics and arbitrary distributions. A disadvantage is the sensitivity for outliers and background, compare appendix A.3.
lWith the expansion of the Weighted MLE (WMLE), as introduced in appendix 4.1.4, the fit can reduce the influence of outliers and background and becomes robust. The typical background in a MR-TOF-MS ranges from background free to signal-to-noise ratios of 1:5. Together with peak statistics of 10-100 counts weighting is the ideal tool to handle background.

A.3. Maximum Likelihood Estimation

The maximum likelihood estimation (MLE) searches for the most likely model parameters for a data set ($x_i, i = 1, .., n$) by maximizing the so called likelihood function [Aldrich et al., 1997]. The likelihood function consists of model based probability density functions (pdf)

$$f\left(x, \tilde{\theta}\right) \tag{A.6}$$

with $\tilde{\theta} = (\theta_1, .., \theta_k)$ as the parameters to be estimated and is the product of these functions for all data points

$$L = \prod_{i=1}^{n} f\left(x_i, \tilde{\theta}\right) \tag{A.7}$$

For large data sets it is numerically easier to work with sums instead of products. Therefore the log-likelihood function is used

$$\mathcal{L} = \ln L = \sum_{i=1}^{n} \ln f\left(x_i, \tilde{\theta}\right) \tag{A.8}$$

The equations A.7 and A.8 have a maximum for the same set of parameter, which can be found by taking the partial derivatives of the log-likelihood function for each parameter and setting it to zero

$$\frac{\partial \mathcal{L}}{\partial \theta_l} = 0 \text{ with } l = 1, .., k \tag{A.9}$$

These differential equations form a system of k equations with k unknown parameters, which can be solved analytically in case of closed-form solutions or with numerical techniques.

Example for Normal Distributed Data The log-likelihood function for normal distributed data with variance σ^2 and peak position μ is

$$\mathcal{L} = \sum_{i=1}^{n} \ln\left(\frac{1}{\sqrt{2\pi\sigma^2}} \exp\left(-\frac{(x_i - \mu)^2}{2\sigma^2}\right)\right) \tag{A.10}$$

$$= \sum_{i=1}^{n} \ln\left(\frac{1}{\sqrt{2\pi\sigma^2}}\right) + \sum_{i=1}^{n} \ln\left(\exp\left(-\frac{(x_i - \mu)^2}{2\sigma^2}\right)\right) \tag{A.11}$$

$$= \sum_{i=1}^{n} \ln\left(\frac{1}{\sqrt{2\pi\sigma^2}}\right) - \frac{1}{2\sigma^2} \sum_{i=1}^{n} (x_i - \mu)^2 \tag{A.12}$$

The peak position μ can now be determined by setting the partial derivative to

zero.

$$\frac{\partial \mathcal{L}}{\partial \mu} = 0 \tag{A.13}$$

$$\Leftrightarrow -\frac{2}{2\sigma^2}\sum_{i=1}^{n}(x_i - \mu) = 0 \tag{A.14}$$

$$\Leftrightarrow \sum_{i=1}^{n}\mu = \sum_{i=1}^{n} x_i \tag{A.15}$$

$$\Leftrightarrow \mu = \frac{1}{n}\sum_{i=1}^{n} x_i \tag{A.16}$$

Equation A.16 shows that for normal distributed data the peak position is just the Arithmetic mean of the data.

What equation A.16 also shows is the disadvantage of the MLE: Like the Arithmetic mean it does not weight data points and as a result is very prone to outliers and background signals. This problem is well known [Stein et al., 1956] and a possible solution is the Weighted Maximum Likelihood Estimation (WMLE) [Hu and Zidek, 2002], where an additional weighting factor τ_i is included in equation A.8.

$$\mathcal{L}_w = \sum_{i=1}^{n} \tau_i \ln\left(f\left(x_i, \vec{\theta}\right)\right) \tag{A.17}$$

The form or value of τ_i is not fixed and must be chosen for each function f individually [Ahmed et al., 2005, Fishbein and Patterson, 1993].
MLE and WMLE have many properties that make them suitable for fitting data [Wang et al., 2004].

A.4. R Programming Language and Test Environment

The fit algorithm is written and tested in R [R Core Team, 2015], a free language and environment for statistical computing and graphics. Several common numerical and statistical routines and tests are already included and further libraries can be imported easily.
R can also include code libraries in different languages like C, C++ and Fortran, like for the KS-Test, see section 4.2.
The fit process as introduced in section 4.1 was developed and tested in R. The final version of the fit process runs in R, but an R environment can be included in other software like for data acquisition to automatize the data analysis.

A.5. Exponentially Modified Gaussian

In a MR-TOF-MS the peak shape is influenced by different effects. For low turn numbers the dominating effect is the turn-around time of the ions which results in a Gaussian like peak shape [Dickel, 2010]. For higher turn numbers the optical aberrations increase and influence the peak shape. The exact peak shape due to these aberrations are not exactly known, but they appear in the tails of the distribution. They are in first order mass independent and depend on the tunning of the MR-TOF-MS and also very weekly on the number of turns. The real peak shape can be better described by the Exponentially Modified Gaussian EMG [Bortels and Collaers, 1987], a convolution of a Gaussian function G and an truncated exponential function. The EMG is well established for example in modeling chromatographic peaks [Foley and Dorsey, 1984].
For the development of a fit algorithm G and EMG functions were used to better understand the behaviour of the algorithm. The probability density function for Gaussian peak shapes is

$$\mathrm{G}(\mathrm{x},\mu,\sigma) = \frac{1}{\sqrt{2\pi\sigma^2}}\exp\left(-\frac{(\mathrm{x}-\mu)^2}{2\sigma^2}\right) \tag{A.18}$$

with the peak centre and mean μ and the width σ. The EMG consists of the function $\mathrm{G}(\mathrm{x},\mu,\sigma)$ and an exponential function truncated on one side

$$\mathrm{F}(\mathrm{x},\mu,\tau) = \frac{1}{\tau}\exp\left(-\xi\frac{\mathrm{x}-\mu}{\tau}\right)\mathrm{H}(\xi\mathrm{x}) \tag{A.19}$$

with parameter τ. For a left-sided exponential is $\xi = -1$ and for a right-sided one is $\xi = +1$. $\mathrm{H}(\xi\mathrm{x})$ is a step function with

$$\mathrm{H}(\xi\mathrm{x}) = \begin{cases} 1 & \text{for } \xi\mathrm{x} \geq 0 \\ 0 & \text{for } \xi\mathrm{x} < 0 \end{cases} \tag{A.20}$$

The joined probability density function is then

$$\mathrm{EMG}(\mathrm{x},\mu,\sigma,\eta,\tau) = \int_{-\infty}^{+\infty}\mathrm{F}(\mathrm{v},\mu,\tau)\mathrm{G}(\mathrm{x}+\mathrm{v},\mu,\sigma)\mathrm{dv} \tag{A.21}$$

and can be written in an integrated form [Bortels and Collaers, 1987] as

$$\mathrm{EMG}(\mathrm{x},\mu,\sigma,\tau) = \frac{1}{2\tau}\exp\left(\frac{1}{2}\left(\frac{\sigma}{\tau}\right)^2 + \xi\frac{\mathrm{x}-\mu}{\tau}\right)\mathrm{erfc}\left(\frac{1}{\sqrt{2}}\left(\frac{\sigma}{\tau}+\xi\frac{\mathrm{x}-\mu}{\sigma}\right)\right) \tag{A.22}$$

Equation A.22 has only one exponential function included, but in order to describe the measured peak shapes N exponentials can be added with k exponentials on the left side and N-k on the right side. The corresponding pdf is realized by summing up and weighting N times equation A.22 [Purushothaman et al., 2016]

$$\mathrm{EMG}(\mathrm{x},\mu,\sigma,\tilde{\eta},\tilde{\tau}) = \frac{1}{4}\sum_{\mathrm{i}=1}^{\mathrm{N}}\frac{\eta_\mathrm{i}}{\tau_\mathrm{i}}\left(\exp\left(\frac{1}{2}\left(\frac{\sigma}{\tau_\mathrm{i}}\right)^2 + \xi_\mathrm{i}\frac{\mathrm{x}-\mu}{\tau_\mathrm{i}}\right)\mathrm{erfc}\left(\frac{1}{\sqrt{2}}\left(\frac{\sigma}{\tau_\mathrm{i}}+\xi_\mathrm{i}\frac{\mathrm{x}-\mu}{\sigma}\right)\right)\right) \tag{A.23}$$

$$\text{with } \sum_{i=1}^{k} \eta_i = \sum_{i=k+1}^{N} \eta_i = 1 \tag{A.24}$$

$$\text{and } \xi_{1,..,k} = +1 \wedge \xi_{k+1,..,N} = -1 \tag{A.25}$$

Normalization is given by equation A.24. Reducing the number of exponentials can be easily achieved by setting the corresponding value of η_i to zero.
Figure 4.3 shows the Gaussian and EMG function in comparison, which were used for the development of a fit algorithm in section 4.1. The EMG function has two exponentials on each side (N=4). For the analysis of measured data the best way to determine the peak shape parameters is a fit of a peak with high statistic (about 10^3 counts or more) with Minimum χ^2 Estimation. The number of exponentials in the fit function can be varied to find the right one. Therefore the fitting started with N exponentials on each side and exponentials with uncertainties of the corresponding weighting factor η_i equal or larger than this factor are removed. This peak shape can also used to describe all other peaks in the spectrum, see section 2.4.3. Therefor the peak width, σ for Gauss and σ and τ for the EMG, must be scaled linearly with the mass-to-charge ratio.

Bibliography

[Aad et al., 2012] Aad, G., Abajyan, T., Abbott, B., Abdallah, J., Khalek, S. A., Abdelalim, A., Abdinov, O., Aben, R., Abi, B., Abolins, M., et al. (2012). Observation of a new particle in the search for the Standard Model Higgs boson with the ATLAS detector at the LHC. *Physics Letters B*, 716(1):1–29.

[Aboussir et al., 1995] Aboussir, Y., Pearson, J., Dutta, A., and Tondeur, F. (1995). Nuclear mass formula via an approximation to the Hartree Fock method. *Atomic Data and Nuclear Data Tables*, 61(1):127–176.

[Ahmed et al., 2005] Ahmed, E. S., Volodin, A., Hussein, A., et al. (2005). Robust weighted likelihood estimation of exponential parameters. *Reliability, IEEE Transactions on*, 54(3):389–395.

[Ahn and Fessler, 2003] Ahn, S. and Fessler, J. A. (2003). Standard errors of mean, variance, and standard deviation estimators. *University of Michigan: EECS Department*.

[Aldrich et al., 1997] Aldrich, J. et al. (1997). RA Fisher and the making of maximum likelihood 1912-1922. *Statistical Science*, 12(3):162–176.

[Andreyev et al., 1989] Andreyev, A., Bogdanov, D., Chepigin, V., Kabachenko, A., Orlova, O., and Ter-Akopian, G. (1989). Measurements of the cross-sections values for light particle evaporation in the irradiation of Au and Pb targets with Ne-ions. *Yad. Fizika*, 50(9):619.

[Aston, 1927] Aston, F. W. (1927). Bakerian lecture. A new mass-spectrograph and the whole number rule. *Proceedings of the Royal Society of London. Series A, Containing Papers of a Mathematical and Physical Character*, pages 487–514.

[Audi et al., 2012] Audi, G., Wang, M., Wapstra, A., Kondev, F., MacCormick, M., Xu, X., and Pfeiffer, B. (2012). The Ame2012 atomic mass evaluation. *Chinese physics C*, 36(12):1287.

[Ayet et al., 2014] Ayet, S., Ebert, J., Dickel, T., Plaß, W., Bergmann, J., Geissel, H., Haettner, E., Hornung, C., Jesch, C., Lang, J., et al. (2014). Recent Technical Improvements for the Multiple-Reflection Time-of-Flight Mass Spectrometer at the FRS Ion Catcher. *GSI Scientific Report 2014*, page 107.

[Ayet San Andres, 2014] Ayet San Andres, S. (2014). personal communication.

[Ayet San Andres, 2016] Ayet San Andres, S. (2016). personal communication.

[Ayet San Andres, 2017] Ayet San Andres, S. (2017). *in preparation*. PhD thesis, Justus-Liebig-Universität Gießen.

[Ayet San Andres and Short, 2015] Ayet San Andres, S. and Short, D. (2015). personal communication.

[Bender et al., 2002] Bender, M., Cornelius, T., Lalazissis, G., Maruhn, J., Nazarewicz, W., and Reinhard, P.-G. (2002). The z= 82 shell closure in neutron-deficient pb isotopes. *The European Physical Journal A-Hadrons and Nuclei*, 14(1):23–28.

[Bergmann, 2015] Bergmann, J. (2015). Entwicklung und Anwendung einer integrierten Systemsteuerung und Datenaufnahme für Flugzeitmassenspektrometer. Master's thesis, Justus-Liebig-Universität Gießen.

[Bergström et al., 2002] Bergström, I., Carlberg, C., Fritioff, T., Douysset, G., Schönfelder, J., and Schuch, R. (2002). SMILETRAP-A Penning trap facility for precision mass measurements using highly charged ions. *Nuclear Instruments and Methods in Physics Research Section A: Accelerators, Spectrometers, Detectors and Associated Equipment*, 487(3):618–651.

[Blaum, 2006] Blaum, K. (2006). High-accuracy mass spectrometry with stored ions. *Physics Reports*, 425(1):1–78.

[Blume and Peipert, 2003] Blume, J. and Peipert, J. F. (2003). What your statistician never told you about P-values. *The Journal of the American Association of Gynecologic Laparoscopists*, 10(4):439–444.

[Bollen, 2004] Bollen, G. (2004). Traps for rare isotopes. In *The Euroschool Lectures on Physics with Exotic Beams, Vol. I*, pages 169–210. Springer.

[Bortels and Collaers, 1987] Bortels, G. and Collaers, P. (1987). Analytical function for fitting peaks in alpha-particle spectra from Si detectors. *International Journal of Radiation Applications and Instrumentation. Part A. Applied Radiation and Isotopes*, 38(10):831–837.

[Bradbury and Nielsen, 1936] Bradbury, N. E. and Nielsen, R. A. (1936). Absolute values of the electron mobility in hydrogen. *Physical Review*, 49(5):388.

[Chaudhuri et al., 2014] Chaudhuri, A., Andreoiu, C., Brodeur, M., Brunner, T., Chowdhury, U., Ettenauer, S., Gallant, A., Grossheim, A., Gwinner, G., Klawitter, R., et al. (2014). TITAN: an ion trap for accurate mass measurements of ms-half-life nuclides. *Applied Physics B*, 114(1-2):99–105.

[Chen, 2008] Chen, L. (2008). *Investigation of stored neutron-rich nuclides in the element range of Pt-U with the FRS-ESR facility at 360-400 MeV/u*. PhD thesis, Justus-Liebig-Universität Gießen.

[Chen et al., 2012] Chen, L., Plass, W., Geissel, H., Knöbel, R., Kozhuharov, C., Litvinov, Y. A., Patyk, Z., Scheidenberger, C., Siegień-Iwaniuk, K., Sun, B., et al. (2012). New results on mass measurements of stored neutron-rich nuclides in the element range from pt to u with the frs-esr facility at 360–400 mev/u. *Nuclear Physics A*, 882:71–89.

[Chomaz, 2003] Chomaz, P. (2003). Introduction: The terra incognita of exotic nuclei. *Comptes Rendus Physique*, 4(4):419–432.

[Dawson, 1976] Dawson, P. H. (1976). Quadrupole mass spectrometry and its applications. *Rapid Commun. Mass Specrom.*, 3:155–159.

[Dennis Jr and Schnabel, 1996] Dennis Jr, J. E. and Schnabel, R. B. (1996). *Numerical methods for unconstrained optimization and nonlinear equations*, volume 16. Siam.

[Dickel, 2010] Dickel, T. (2010). *Design and Commissioning of an Ultra-High-Resolution Time-of-Flight Based Isobar Separator and Mass Spectrometer*. PhD thesis, Justus-Liebig-Universität Gießen.

[Dickel et al., 2015a] Dickel, T., Plaß, W., Becker, A., Czok, U., Geissel, H., Haettner, E., Jesch, C., Kinsel, W., Petrick, M., Scheidenberger, C., et al. (2015a). A high-performance multiple-reflection time-of-flight mass spectrometer and isobar separator for the research with exotic nuclei. *Nuclear Instruments and Methods in Physics Research Section A: Accelerators, Spectrometers, Detectors and Associated Equipment*, 777:172–188.

[Dickel et al., 2015b] Dickel, T., Plaß, W., San Andres, S. A., Ebert, J., Geissel, H., Haettner, E., Hornung, C., Miskun, I., Pietri, S., Purushothaman, S., et al. (2015b). First spatial separation of a heavy ion isomeric beam with a multiple-reflection time-of-flight mass spectrometer. *Physics Letters B*, 744:137–141.

[Diwisch, 2015] Diwisch, M. (2015). *Present and Future Isochronous Mass Spectrometry at GSI-FAIR*. PhD thesis, Justus-Liebig-Universität Gießen.

[Dobaczewski et al., 1996] Dobaczewski, J., Nazarewicz, W., Werner, T., Berger, J., Chinn, C., and Dechargé, J. (1996). Mean-field description of ground-state properties of drip-line nuclei: Pairing and continuum effects. *Physical Review C*, 53(6):2809.

[Duflo and Zuker, 1995] Duflo, J. and Zuker, A. (1995). Microscopic mass formulas. *Physical Review C*, 52(1):R23.

[Durbin, 1973] Durbin, J. (1973). *Distribution theory for tests based on the sample distribution function*, volume 9. Siam.

[Ettenauer et al., 2013] Ettenauer, S., Simon, M., Macdonald, T., and Dilling, J. (2013). Advances in precision, resolution, and separation techniques with radioactive, highly charged ions for Penning trap mass measurements. *International Journal of Mass Spectrometry*, 349:74–80.

[Farinon et al., 2011] Farinon, F., Pietri, S., Brünle, A., Geissel, H., Kojouharov, I., and Nociforo, C. (2011). Development and test of an α-tagger detector at the FRS. *GSI Scientific Report*, page 148.

[Fishbein and Patterson, 1993] Fishbein, E. and Patterson, R. T. (1993). Error-weighted maximum likelihood (EWML): a new statistically based method to cluster quantitative micropaleontological data. *Journal of Paleontology*, pages 475–486.

[Foley and Dorsey, 1984] Foley, J. P. and Dorsey, J. G. (1984). A review of the exponentially modified Gaussian (EMG) function: evaluation and subsequent calculation of universal data. *Journal of chromatographic science*, 22(1):40–46.

[Franzke, 1987] Franzke, B. (1987). The heavy ion storage and cooler ring project ESR at GSI. *Nuclear Instruments and Methods in Physics Research Section B: Beam Interactions with Materials and Atoms*, 24:18–25.

[Franzke et al., 2008] Franzke, B., Geissel, H., and Münzenberg, G. (2008). Mass and lifetime measurements of exotic nuclei in storage rings. *Mass Spectrometry Reviews*, 27(5):428–469.

[Gaimard and Schmidt, 1991] Gaimard, J.-J. and Schmidt, K.-H. (1991). A reexamination of the abrasion-ablation model for the description of the nuclear fragmentation reaction. *Nuclear Physics A*, 531(3):709–745.

[Geissel et al., 1992] Geissel, H., Armbruster, P., Behr, K., Brünle, A., Burkard, K., Chen, M., Folger, H., Franczak, B., Keller, H., Klepper, O., et al. (1992). The GSI projectile fragment separator (FRS): a versatile magnetic system for relativistic heavy ions. *Nuclear Instruments and Methods in Physics Research Section B: Beam Interactions with Materials and Atoms*, 70(1):286–297.

[Geissel et al., 1995] Geissel, H., Munzenberg, G., and Riisager, K. (1995). Secondary exotic nuclear beams. *Annual Review of Nuclear and Particle Science*, 45(1):163–203.

[Geissel et al., 2016] Geissel, H., Münzenberg, G., and Scheidenberger, C. (2016). 25 Years of FRS Experiments and New Horizons. *to be published*.

[Geissel et al., 2003] Geissel, H., Weick, H., Winkler, M., Münzenberg, G., Chichkine, V., Yavor, M., Aumann, T., Behr, K., Böhmer, M., Brünle, A., et al. (2003). The

Super-FRS project at GSI. *Nuclear Instruments and Methods in Physics Research Section B: Beam Interactions with Materials and Atoms*, 204:71–85.

[Geissel et al., 2013] Geissel, H., Winfield, J., Berg, G., Franczak, B., Iwasa, N., Münzenberg, G., Nociforo, C., Plaß, W., Scheidenberger, C., Weick, H., et al. (2013). Dispersion-matched spectrometer in the low-energy branch of the Super-FRS for high-resolution measurements with large-emittance relativistic fragment beams. *Nuclear Instruments and Methods in Physics Research Section B: Beam Interactions with Materials and Atoms*, 317:277–283.

[Greiner, 2013] Greiner, F. (2013). Aufbau und Erprobung einer elektrischen RFQ-Strahlweiche. Bachelor's thesis, Justus-Liebig-Universität Gießen.

[Greiner and Miskun, 2016] Greiner, F. and Miskun, I. (2016). personal communication. Discharge source.

[Haettner, 2012] Haettner, E. (2012). personal communication.

[Hahn et al., 1969] Hahn, R., Roche, M., and Toth, K. (1969). Alpha Decay of U 227. *Physical Review*, 182(4):1329.

[Hausmann et al., 2000] Hausmann, M., Attallah, F., Beckert, K., Bosch, F., Dolinskiy, A., Eickhoff, H., Falch, M., Franczak, B., Franzke, B., Geissel, H., et al. (2000). First isochronous mass spectrometry at the experimental storage ring esr. *Nuclear Instruments and Methods in Physics Research Section A: Accelerators, Spectrometers, Detectors and Associated Equipment*, 446(3):569–580.

[Healey, 2014] Healey, J. (2014). *Statistics: A tool for social research*. Cengage Learning.

[Heßberger et al., 2000] Heßberger, F., Hofmann, S., Ackermann, D., Ninov, V., Leino, M., Saro, S., Andreyev, A., Lavrentev, A., Popeko, A., and Yeremin, A. (2000). Decay properties of neutron-deficient nuclei in the region Z= 86–92. *The European Physical Journal A*, 8(4):521–535.

[Hornung, 2013] Hornung, C. (2013). A Laser Ablation Carbon Cluster Ion Source for a Multiple-Reflection Time-Of-Flight Mass Spectrometer. Master's thesis, Justus-Liebig-Universität Gießen.

[Hu and Zidek, 2002] Hu, F. and Zidek, J. V. (2002). The weighted likelihood. *Canadian Journal of Statistics*, 30(3):347–371.

[Hüfner et al., 1975] Hüfner, J., Schäfer, K., and Schürmann, B. (1975). Abrasion-ablation in reactions between relativistic heavy ions. *Physical Review C*, 12(6):1888.

[Igor Pro, 2015] Igor Pro (2015). Igor Pro. https://www.wavemetrics.com/products/igorpro/igorpro.htm.

[Ito et al., 2013] Ito, Y., Schury, P., Wada, M., Naimi, S., Sonoda, T., Mita, H., Arai, F., Takamine, A., Okada, K., Ozawa, A., et al. (2013). Single-reference high-precision mass measurement with a multireflection time-of-flight mass spectrograph. *Physical Review C*, 88(1):011306.

[Janik et al., 2011] Janik, R., Prochazka, A., Sitar, B., Strmen, P., Szarka, I., Geissel, H., Behr, K.-H., Karagiannis, C., Nociforo, C., Weick, H., et al. (2011). Time Projection Chambers with C-pads for heavy ion tracking. *Nuclear Instruments and Methods in Physics Research Section A: Accelerators, Spectrometers, Detectors and Associated Equipment*, 640(1):54–57.

[Jesch, 2008] Jesch, C. (2008). Injektions-Ionenfallensystem für ein Multireflexions-Flugzeitmassenspektrometer. Diplomarbeit, Justus-Liebig-Universität Gießen.

[Jesch, 2014] Jesch, C. (2014). personal communication.

[Jesch, 2016] Jesch, C. (2016). *The Multiple-Reflection Time-of-Flight Isobar Separator for TITAN and Direct Mass Measurements at the FRS Ion Catcher*. PhD thesis, Justus-Liebig-Universität Gießen.

[Jokinen et al., 1997] Jokinen, A., Evensen, A., Kugler, E., Lettry, J., Ravn, H., Van Duppen, P., Erdmann, N., Jading, Y., Köhler, S., Kratz, K., et al. (1997). Selective laser ionization of radioactive ni-isotopes. *Nuclear Instruments and Methods in Physics Research Section B: Beam Interactions with Materials and Atoms*, 126(1):95–99.

[Kenney and Keeping, 1962] Kenney, J. and Keeping, E. (1962). The Median. *Mathematics of statistics*, pages 211–212.

[Knöbel et al., 2016] Knöbel, R., Diwisch, M., Bosch, F., Boutin, D., Chen, L., Dimopoulou, C., Dolinskii, A., Franczak, B., Franzke, B., Geissel, H., et al. (2016). First direct mass measurements of stored neutron-rich 129,130,131 Cd isotopes with FRS-ESR. *Physics Letters B*.

[Kolmogorov, 1933] Kolmogorov, A. N. (1933). *Sulla determinazione empirica di una legge di distribuzione*. na.

[Kowalska et al., 2009] Kowalska, M., Naimi, S., Agramunt, J., Algora, A., Audi, G., Beck, D., Blank, B., Blaum, K., Böhm, C., Breitenfeldt, M., et al. (2009). Preparing a journey to the east of 208Pb with ISOLTRAP: Isobaric purification at A= 209 and new masses for 211-213Fr and 211Ra. *The European Physical Journal A*, 42(3):351–359.

[Lange, 2010] Lange, K. (2010). *Numerical analysis for statisticians*. Springer Science & Business Media.

[Leys et al., 2013] Leys, C., Ley, C., Klein, O., Bernard, P., and Licata, L. (2013).

Detecting outliers: Do not use standard deviation around the mean, use absolute deviation around the median. *Journal of Experimental Social Psychology*, 49(4):764–766.

[Litvinov et al., 2005] Litvinov, Y. A., Geissel, H., Radon, T., Attallah, F., Audi, G., Beckert, K., Bosch, F., Falch, M., Franzke, B., Hausmann, M., et al. (2005). Mass measurement of cooled neutron-deficient bismuth projectile fragments with time-resolved Schottky mass spectrometry at the FRS-ESR facility. *Nuclear Physics A*, 756(1):3–38.

[Liu et al., 2011] Liu, M., Wang, N., Deng, Y., and Wu, X. (2011). Further improvements on a global nuclear mass model. *Physical Review C*, 84(1):014333.

[Loboda et al., 2000] Loboda, A., Krutchinsky, A., Loboda, O., McNabb, J., Spicer, V., Ens, W., and Standing, K. (2000). Novel Linac II electrode geometry for creating an axial field in a multipole ion guide. *European Journal of Mass Spectrometry*, 6(6):531–536.

[Lotze, 2014] Lotze, C. (2012-2014). personal communication.

[Lunney et al., 2003] Lunney, D., Pearson, J., and Thibault, C. (2003). Recent trends in the determination of nuclear masses. *Reviews of Modern Physics*, 75(3):1021.

[Miskun, 2015] Miskun, I. (2015). Diploma Thesis.

[Mittig et al., 1997] Mittig, W., Lépine-Szily, A., and Orr, N. (1997). Mass measurement far from stability. *Annual Review of Nuclear and Particle Science*, 47(1):27–66.

[Moller et al., 1995] Moller, P., Nix, J. R., Myers, W., and Swiatecki, W. (1995). Nuclear ground-state masses and deformations. *Atomic Data and Nuclear Data Tables*, 59(2):185–381.

[Morrissey, 1989] Morrissey, D. (1989). Systematics of momentum distributions from reactions with relativistic ions. *Physical Review C*, 39(2):460.

[Mumpower et al., 2015] Mumpower, M., Surman, R., Fang, D., Beard, M., and Aprahamian, A. (2015). The impact of uncertain nuclear masses near closed shells on the r-process abundance pattern. *Journal of Physics G: Nuclear and Particle Physics*, 42(3):034027.

[Münzenberg, 1998] Münzenberg, G. (1998). Synthesis and investigation of superheavy elements: perspectives on radioactive beams. *PHILOSOPHICAL TRANSACTIONS-ROYAL SOCIETY OF LONDON SERIES A MATHEMATICAL PHYSICAL AND ENGINEERING SCIENCES*, pages 2083–2104.

[Nuzzo, 2014] Nuzzo, R. (2014). Statistical errors. *Nature*, 506(7487):150–152.

[Okumura et al., 2004] Okumura, D., Toyoda, M., Ishihara, M., and Katakuse, I. (2004). Application of a multi-turn time-of-flight mass spectrometer, multum ii, to organic compounds ionized by matrix-assisted laser desorption/ionization. *Journal of mass spectrometry*, 39(1):86–90.

[Paul and Steinwedel, 1953] Paul, W. and Steinwedel, H. (1953). Notizen: Ein neues Massenspektrometer ohne Magnetfeld. *Zeitschrift für Naturforschung A*, 8(7):448–450.

[Pfützner et al., 1994] Pfützner, M., Geissel, H., Münzenberg, G., Nickel, F., Scheidenberger, C., Schmidt, K.-H., Sümmerer, K., Brohm, T., Voss, B., and Bichsel, H. (1994). Energy deposition by relativistic heavy ions in thin argon absorbers. *Nuclear Instruments and Methods in Physics Research Section B: Beam Interactions with Materials and Atoms*, 86(3):213–218.

[Pikhtelev, 2014] Pikhtelev, A. (2014). personal communication. Original version of MAc software.

[Plaß et al., 2007] Plaß, W., Dickel, T., Petrick, M., Boutin, D., Di, Z., Fleckenstein, T., Geissel, H., Jesch, C., Scheidenberger, C., and Wang, Z. (2007). An rf quadrupole–time-of-flight system for isobar-separation and multiplexed low-energy rare-isotope beam experiments. *The European Physical Journal Special Topics*, 150(1):367–368.

[Plaß et al., 2008] Plaß, W. R., Dickel, T., Czok, U., Geissel, H., Petrick, M., Reinheimer, K., Scheidenberger, C., and Yavor, M. I. (2008). Isobar separation by time-of-flight mass spectrometry for low-energy radioactive ion beam facilities. *Nuclear Instruments and Methods in Physics Research Section B: Beam Interactions with Materials and Atoms*, 266(19):4560–4564.

[Plaß et al., 2015] Plaß, W. R., Dickel, T., San Andres, S. A., Ebert, J., Greiner, F., Hornung, C., Jesch, C., Lang, J., Lippert, W., Majoros, T., et al. (2015). High-performance multiple-reflection time-of-flight mass spectrometers for research with exotic nuclei and for analytical mass spectrometry. *Physica Scripta*, 2015(T166):014069.

[Plaß et al., 2013] Plaß, W. R., Dickel, T., and Scheidenberger, C. (2013). Multiple-reflection time-of-flight mass spectrometry. *International Journal of Mass Spectrometry*, 349:134–144.

[Purushothaman, 2014] Purushothaman, S. (2014). personal communication.

[Purushothaman et al., 2016] Purushothaman, S. et al. (2016). Manuscript in preparation.

[Purushothaman et al., 2013] Purushothaman, S., Reiter, M., Haettner, E., Dendooven, P., Dickel, T., Geissel, H., Ebert, J., Jesch, C., Plass, W., Ranjan, M.,

et al. (2013). First experimental results of a cryogenic stopping cell with short-lived, heavy uranium fragments produced at 1000 MeV/u. *EPL (Europhysics Letters)*, 104(4):42001.

[R Core Team, 2015] R Core Team (2015). *R: A Language and Environment for Statistical Computing*. R Foundation for Statistical Computing, Vienna, Austria.

[Radon et al., 1997] Radon, T., Kerscher, T., Schlitt, B., Beckert, K., Beha, T., Bosch, F., Eickhoff, H., Franzke, B., Fujita, Y., Geissel, H., et al. (1997). Schottky mass measurements of cooled proton-rich nuclei at the gsi experimental storage ring. *Physical review letters*, 78(25):4701.

[Ranjan et al., 2015] Ranjan, M., Dendooven, P., Purushothaman, S., Dickel, T., Reiter, M., Ayet, S., Haettner, E., Moore, I., Kalantar-Nayestanaki, N., Geissel, H., et al. (2015). Design, construction and cooling system performance of a prototype cryogenic stopping cell for the Super-FRS at FAIR. *Nuclear Instruments and Methods in Physics Research Section A: Accelerators, Spectrometers, Detectors and Associated Equipment*, 770:87–97.

[Ranjan et al., 2011] Ranjan, M., Purushothaman, S., Dickel, T., Geissel, H., Plass, W., Schäfer, D., Scheidenberger, C., Van de Walle, J., Weick, H., and Dendooven, P. (2011). New stopping cell capabilities: RF carpet performance at high gas density and cryogenic operation. *EPL (Europhysics Letters)*, 96(5):52001.

[Reiter, 2011] Reiter, M. P. (2011). Simulation der kryogenen Stoppzelle des FRS-Ion-Catchers-Experiments und Aufbau eines neuartigen RFQ-Strahlführungssystems. Master's thesis, Justus-Liebig-Universität Gießen.

[Reiter, 2015] Reiter, M. P. (2015). *Pilot Experiments with Relativistic Uranium Projectile and Fission Fragments Thermalized in a Cryogenic Gas filled Stopping Cell*. PhD thesis, Justus-Liebig-Universität Gießen.

[Ruiz, 1961] Ruiz, C. P. (1961). Alpha decay studies in the families of the light uranium isotopes. Technical report, Lawrence Berkeley Nat. Lab.

[Satoh et al., 2005] Satoh, T., Tsuno, H., Iwanaga, M., and Kammei, Y. (2005). The design and characteristic features of a new time-of-flight mass spectrometer with a spiral ion trajectory. *Journal of the American Society for Mass Spectrometry*, 16(12):1969–1975.

[Scheidenberger et al., 2001] Scheidenberger, C., Attallah, F., Casares, A., Czok, U., Dodonov, A., Eliseev, S., Geissel, H., Hausmann, M., Kholomeev, A., Kozlovski, V., et al. (2001). A new concept for time-of-flight mass spectrometry with slowed-down short-lived isotopes. *Hyperfine Interactions*, 132(1-4):527–530.

[Schury et al., 2014] Schury, P., Wada, M., Ito, Y., Arai, F., Naimi, S., Sonoda, T., Wollnik, H., Shchepunov, V., Smorra, C., and Yuan, C. (2014). A high-resolution

multi-reflection time-of-flight mass spectrograph for precision mass measurements at RIKEN/SLOWRI. *Nuclear Instruments and Methods in Physics Research Section B: Beam Interactions with Materials and Atoms*, 335:39–53.

[Siebring, 2012] Siebring, J. (2012). personal communication. Labview.

[Simon, 2008] Simon, A. (2008). Entwicklung und Test eines CFK-basierten RF-Quadrupols fÃ¼r ein Multireflektions-Flugzeitmassenspektrometer. Bachelor's thesis, Justus-Liebig-Universität Gießen.

[Sinervo, 2002] Sinervo, P. K. (2002). Signal significance in particle physics. *arXiv preprint hep-ex/0208005*.

[Smirnov, 1944] Smirnov, N. V. (1944). Approximate laws of distribution of random variables from empirical data. *Uspekhi Matematicheskikh Nauk*, (10):179–206.

[Stein et al., 1956] Stein, C. et al. (1956). Inadmissibility of the usual estimator for the mean of a multivariate normal distribution. In *Proceedings of the Third Berkeley symposium on mathematical statistics and probability*, number 399 in 1, pages 197–206.

[Takamine, 2007] Takamine, A. e. a. (2007). Improvement of slow RI beam transport using carbon-OPIG. *Riken accelerator progress report*, 40:147.

[Taylor, 1982] Taylor, J. R. (1982). An Introduction to Error Analysis: The Study of Uncertainties in Physical Measurements. *Univ. Sci. Books, Mill Valley, Calif*.

[Thielemann et al., 2001] Thielemann, F.-K., Brachwitz, F., Freiburghaus, C., Kolbe, E., Martinez-Pinedo, G., Rauscher, T., Rembges, F., Hix, W., Liebendörfer, M., Mezzacappa, A., et al. (2001). Element synthesis in stars. *Progress in Particle and Nuclear Physics*, 46(1):5–22.

[Torgerson and Macfarlane, 1970] Torgerson, D. F. and Macfarlane, R. D. (1970). Alpha-Decay Studies of the N= 127 Isotones Fr 214, Ra 215, and Ac 216. *Physical Review C*, 2(6):2309.

[Verentchikov et al., 2005] Verentchikov, A., Yavor, M., Hasin, Y. I., and Gavrik, M. (2005). Multireflection planar time-of-flight mass analyzer. I: An analyzer for a parallel tandem spectrometer. *Technical Physics*, 50(1):73–81.

[Wang et al., 2003] Wang, J., Tsang, W. W., and Marsaglia, G. (2003). Evaluating Kolmogorov's distribution. *Journal of Statistical Software*, 8(18).

[Wang et al., 2012] Wang, M., Audi, G., Wapstra, A., Kondev, F., MacCormick, M., Xu, X., and Pfeiffer, B. (2012). The AME2012 atomic mass evaluation(II). Tables, graphs and references. *Chinese Physics C*, 12:004.

[Wang et al., 2004] Wang, X., van Eeden, C., and Zidek, J. V. (2004). Asymptotic properties of maximum weighted likelihood estimators. *Journal of Statistical Planning and Inference*, 119(1):37–54.

[Weizsäcker, 1935] Weizsäcker, C. v. (1935). Zur theorie der kernmassen. *Zeitschrift für Physik A Hadrons and Nuclei*, 96(7):431–458.

[Wiley and McLaren, 1955] Wiley, W. and McLaren, I. H. (1955). Time-of-flight mass spectrometer with improved resolution. *Review of Scientific Instruments*, 26(12):1150–1157.

[Wiza, 1979] Wiza, J. L. (1979). Microchannel plate detectors. *Nuclear Instruments and Methods*, 162(1):587–601.

[Wolf et al., 2013] Wolf, R., Wienholtz, F., Atanasov, D., Beck, D., Blaum, K., Borgmann, C., Herfurth, F., Kowalska, M., Kreim, S., Litvinov, Y. A., et al. (2013). Isoltrap's multi-reflection time-of-flight mass separator/spectrometer. *International Journal of Mass Spectrometry*, 349:123–133.

[Wollnik, 1987] Wollnik, H. (1987). Mass separators. *Nuclear Instruments and Methods in Physics Research Section A: Accelerators, Spectrometers, Detectors and Associated Equipment*, 258(3):289–296.

[Wollnik and Casares, 2003] Wollnik, H. and Casares, A. (2003). An energy-isochronous multi-pass time-of-flight mass spectrometer consisting of two coaxial electrostatic mirrors. *International Journal of Mass Spectrometry*, 227:217–222.

[Yavor, 2009] Yavor, M. (2009). *Optics of charged particle analyzers*. Academic Press.

[Yavor et al., 2015] Yavor, M. I., Plaß, W. R., Dickel, T., Geissel, H., and Scheidenberger, C. (2015). Ion-optical design of a high-performance multiple-reflection time-of-flight mass spectrometer and isobar separator. *International Journal of Mass Spectrometry*.

[Yoon et al., 2007] Yoon, O. K., Zuleta, I. A., Robbins, M. D., Barbula, G. K., and Zare, R. N. (2007). Simple template-based method to produce Bradbury-Nielsen gates. *Journal of the American Society for Mass Spectrometry*, 18(11):1901–1908.

Acknowledgments

An dieser Stelle möchte ich gerne all jenen danken, die mir beim Erstellen dieser Arbeit geholfen und mich während meiner Promotion unterstützt haben:

- Prof. Dr. Christoph Scheidenberger für die Möglichkeit, am MR-TOF-MS arbeiten zu können.

- Prof. Dr. Dr. h. c. Hans Geissel für die Hilfe und Vorschläge beim Schreiben meiner Arbeit.

- Dr. Wolfgang R. Plaß für die vielen Diskussionen und anregenden Ideen bei der Entwicklung der Fitmethode und der Auswertung der Messergebnisse.

- Dr. Timo Dickel fü die gute und intensive Betreuung während meiner ganzen Arbeit. Sei es im Labor, am Computer oder vor einer Tafel.

- Den Leuten, mit denen ich zahllose Stunden im Labor verbracht habe, die immer eine helfende Hand hatten und viele gute Ideen, ohne die die oftmals anstrengenden Experimente nicht so gut verlaufen wären: Samuel Ayet, Florian Greiner, Christine Hornung, Ivan Miskun, Dr. Sivaji Purushothaman, Dr. Pascal Reiter und Ann-Kathrin Rink.

- Allen Mitgliedern der FRS Ion Catcher Kollaboration. Für ein so großes Experiment sind viele gute Leute notwendig, um es so erfolgreich zum laufen zu bringen.

- Allen Angehörigen der IONAS Gruppe, aktuellen wie ehemaligen. Es war eine schöne Zeit mit euch allen.

- Meiner Familie und meiner Freundin, die mir immer zur Seite standen, wenn ich es brauchte.

Selbstständigkeitserklärung

Ich erkläre: Ich habe die vorgelegte Dissertation selbständig und ohne unerlaubte fremde Hilfe und nur mit den Hilfen angefertigt, die ich in der Dissertation angegeben habe. Alle Textstellen, die wörtlich oder sinngemäß aus veröffentlichten Schriften entnommen sind, und alle Angaben, die auf mündlichen Auskünften beruhen, sind als solche kenntlich gemacht. Bei den von mir durchgeführten und in der Dissertation erwähnten Untersuchungen habe ich die Grundsätze guter wissenschaftlicher Praxis, wie sie in der „Satzung der Justus-Liebig-Universität Gießen zur Sicherung guter wissenschaftlicher Praxis“ niedergelegt sind, eingehalten.

Datum Jens Ebert

Erstgutachter: Prof. Dr. Christoph Scheidenberger
Zweitgutachter: Prof. Dr. Dr. h.c. Hans Geissel